

<b>REPORT DOCUMENTATION PAGE</b>					<i>Form Approved OMB No. 0704-0188</i>	
<small>The public reporting burden for this collection of information is estimated to average 1 hour per response, including the time for reviewing instructions, searching existing data sources, gathering and maintaining the data needed, and completing and reviewing the collection of information. Send comments regarding this burden estimate or any other aspect of this collection of information, including suggestions for reducing the burden, to Department of Defense, Washington Headquarters Services, Directorate for Information Operations and Reports (0704-0188), 1215 Jefferson Davis Highway, Suite 1204, Arlington, VA 22202-4302. Respondents should be aware that notwithstanding any other provision of law, no person shall be subject to any penalty for failing to comply with a collection of information if it does not display a currently valid OMB control number.</small>						
<b>PLEASE DO NOT RETURN YOUR FORM TO THE ABOVE ADDRESS.</b>						
<b>1. REPORT DATE (DD-MM-YYYY)</b>		<b>2. REPORT TYPE</b>			<b>3. DATES COVERED (From - To)</b>	
<b>4. TITLE AND SUBTITLE</b>				<b>5a. CONTRACT NUMBER</b>		
				<b>5b. GRANT NUMBER</b>		
				<b>5c. PROGRAM ELEMENT NUMBER</b>		
<b>6. AUTHOR(S)</b>				<b>5d. PROJECT NUMBER</b>		
				<b>5e. TASK NUMBER</b>		
				<b>5f. WORK UNIT NUMBER</b>		
<b>7. PERFORMING ORGANIZATION NAME(S) AND ADDRESS(ES)</b>					<b>8. PERFORMING ORGANIZATION REPORT NUMBER</b>	
<b>9. SPONSORING/MONITORING AGENCY NAME(S) AND ADDRESS(ES)</b>					<b>10. SPONSOR/MONITOR'S ACRONYM(S)</b>	
					<b>11. SPONSOR/MONITOR'S REPORT NUMBER(S)</b>	
<b>12. DISTRIBUTION/AVAILABILITY STATEMENT</b>						
<b>13. SUPPLEMENTARY NOTES</b>						
<b>14. ABSTRACT</b>						
<b>15. SUBJECT TERMS</b>						
<b>16. SECURITY CLASSIFICATION OF:</b>			<b>17. LIMITATION OF ABSTRACT</b>	<b>18. NUMBER OF PAGES</b>	<b>19a. NAME OF RESPONSIBLE PERSON</b>	
a. REPORT	b. ABSTRACT	c. THIS PAGE			<b>19b. TELEPHONE NUMBER (Include area code)</b>	

# **A Novel Method for Prediction of Nonlinear Aeroelastic Responses**

FINAL REPORT

GRANT #FA9550-07-1-0289

PAUL G. A. CIZMAS AND THOMAS W. STRGANAC

DATE REPORT WAS ISSUED: JANUARY 2010

# Contents

<b>Abstract</b>	<b>5</b>
<b>Nomenclature</b>	<b>6</b>
<b>1 Introduction</b>	<b>9</b>
<b>2 Improvements of the Reduced-Order Model based on Proper Orthogonal Decomposition</b>	<b>10</b>
2.1 Acceleration Techniques for the Proper Orthogonal Decomposition Method . . . . .	10
2.1.1 Database Splitting . . . . .	11
2.1.2 Novel Solver for Linear Systems with Quasi-symmetric Matrices . . . . .	13
2.2 Proper Orthogonal Decomposition Method for Flows with Discontinuities . . . . .	16
2.2.1 Augmented Proper Orthogonal Decomposition Method . . . . .	16
2.2.2 Discontinuities Capturing using Mathematical Morphology . . . . .	19
<b>3 A Novel Nonlinear Beam Model</b>	<b>24</b>
3.1 Derivation of the Nonlinear Equations of Motion . . . . .	24
3.1.1 Overview . . . . .	24
3.1.2 Definition of Parameters . . . . .	24
3.1.3 The Lagrangian . . . . .	26
3.1.4 Inextensionality Constraint . . . . .	27
3.1.5 Hamilton's Principle . . . . .	27
3.1.6 Application of the Galerkin Method . . . . .	28
3.1.6.1 Bending Equations of Motion . . . . .	28
3.1.6.2 Torsional Equation of Motion . . . . .	29
3.1.7 The Lagrange Multiplier . . . . .	29
3.1.8 The Equations of Motion . . . . .	32
3.2 Modal Representation . . . . .	34
3.2.1 Introduction . . . . .	34
3.2.2 Linear Matrices . . . . .	36
3.2.2.1 Linear Mass Matrix . . . . .	36
3.2.2.2 Linear Damping Matrix . . . . .	37
3.2.2.3 Linear Stiffness Matrix . . . . .	37
3.2.3 Nonlinear Matrices . . . . .	37
3.2.3.1 Nonlinear Mass Matrix . . . . .	38
3.2.3.2 Nonlinear Damping Matrix . . . . .	40
3.2.3.3 Nonlinear Stiffness Matrix . . . . .	41
3.2.4 Forcing Vectors . . . . .	42

3.2.4.1	Linear Forcing Vector . . . . .	42
3.2.4.2	Nonlinear Forcing Vector . . . . .	43
3.3	Numerical Implementation of the Structural Solver . . . . .	43
3.3.1	Overview . . . . .	43
3.3.2	Matrices . . . . .	43
3.3.3	Forcing Vectors . . . . .	44
3.3.4	Solution . . . . .	44
3.4	Structural Solver Validation . . . . .	45
3.4.1	Method . . . . .	45
3.4.2	Natural Frequencies . . . . .	45
3.4.2.1	Case 1: A Tapered Beam . . . . .	46
3.4.2.2	Case 2: A Twisted Beam . . . . .	48
3.4.2.3	Case 3: A Composite Beam . . . . .	48
3.5	Finite Element Method Code for Plates . . . . .	52
<b>4</b>	<b>Continuation Methods</b>	<b>55</b>
<b>5</b>	<b>A Novel Flow Solver Grid Generator for Aircraft with Extreme Wing Deformation</b>	<b>58</b>
5.1	Background information . . . . .	58
5.2	Conformal Mapping . . . . .	59
5.3	Grid Quality . . . . .	61
<b>A</b>	<b>Nonlinear Beam - Hamilton's Principle</b>	<b>69</b>

# List of Figures

2.1	Cumulative energy spectrum. . . . .	11
2.2	Slope of the total CPU time vs physical time measured at 0.01 s increments. . . . .	12
2.3	Degree of non-symmetry $\eta$ as a function of the multiplying factor $X$ . . . . .	17
2.4	Effect of degree of non-symmetry on: (a) number of iterations, and (b) Eulerian norm of difference between the solutions of the LU decomposition and the present method. . . . .	18
2.5	Velocity profile at $t = 1.0$ for full-order model, reduced-order model with 20 modes and no discontinuity mode, and reduced-order model with 2 modes, including a discontinuity mode (Brenner et al., 2009). . . . .	20
2.6	Edge strength index. . . . .	23
2.7	Mach number contours. . . . .	23
3.1	Diagram of Deformed Beam . . . . .	25
3.2	Heavy Goland Wing time coefficients at LCO: (a) out-of-plane bending, and (b) pitching. . . . .	35
3.3	Heavy Goland Wing time coefficients at flutter: (a) out-of-plane bending, and (b) pitching. . . . .	36
3.4	Tapered beam with $100 \times 5 \times 6$ mesh. . . . .	46
3.5	Twisted beam with $100 \times 5 \times 10$ mesh. . . . .	48
3.6	Composite beam. . . . .	50
3.7	Generic transport wing. . . . .	53
3.8	Generic transport wing: first three modes. . . . .	54
4.1	Example bifurcation diagram showing the effect of trim constraint. . . . .	56
4.2	Sensitivity to aspect ratio: transition to subcritical from supercritical behavior at angle of attach 2.8 deg and in-plane to out-of-plane stiffness ratio, $\beta_n=4$ . . . . .	57
5.1	Grid generator: (a) detail of topologically identical layers along the wing, and (b) aircraft configuration. . . . .	59
5.2	Conformal mapping components. . . . .	60
5.3	Conformal mapping O-grid surrounded by unstructured grid. . . . .	61
5.4	Grid quality based on angle: (a) Poisson solver, and (b) conformal mapping. . . . .	62
5.5	Hybrid grid around the wing with O-grid generated using conformal mapping, assuming exaggerated chord-wise deformation. . . . .	63
5.6	Isometric projection of deformed and undeformed grids of the Goland wing - tip deformation of 60% of wing semi-span (Cizmas and Gargoloff, 2008). . . . .	63

# Abstract

The configuration design space and flight regime of new air vehicles is vast. Determination of nonlinear aeroelastic responses, vehicle trim states and vehicle stability is a challenge that must be addressed in an efficient, methodical manner. To accomplish this, we are developing a method for determining and analyzing nonlinear aeroelastic responses using a combination of a continuation method with a variable-fidelity reduced-order model of the flowfield, a nonlinear description of structural response, and a trim model of the air vehicle capturing both rigid body and flexible body motions.

This report summarizes the accomplishments made during this funding cycle of the project. These results include new techniques developed for reduced-order modeling using the proper orthogonal decomposition (POD) method, a novel nonlinear beam model, and high-quality grid generator for aircraft with very large wing deformation.

To improve the efficiency of the reduced-order model based on POD, we developed several acceleration techniques. The most effective acceleration methods were database splitting and a new solver for linear systems with quasi-symmetric matrices. To improve the accuracy and efficiency of the POD method applied to unsteady flows with shocks, we developed a method for capturing discontinuities using mathematical morphology and a technique for augmenting the POD basis functions.

To reduce the computational time for structural modeling and to allow us to use continuation methods, we developed a novel nonlinear beam model. Though some facets of the method and model presented herein have been seen before, there are several features worth noting that distinguish this work. Compared to previous work, this method offers improvement by accounting for a non-uniform beam with the center of mass of each cross section offset from the elastic axis. This approach additionally permits rotation of the centroidal axes along the length of the undeformed beam and uses the Galerkin method to address abrupt lengthwise variations numerically. This model improves upon prior work by extending the order of the nonlinear terms retained to the third order. The method developed herein includes the ability to account for the nonlinear contribution of mass-offset, mass-offset in both dimensions, non-uniformity, principal bending and stiffness axes that vary mutually and along the length of the beam, abrupt lengthwise property changes, and the consistent retention of all third-order terms. Compared to finite element results, the method developed herein is two orders of magnitude faster, while the frequency errors are typically less than 1% (the maximum error value encountered was 3.4% for the forth mode).

Although the nonlinear beam element presented above excels on both accuracy and efficiency, not all structures can be modeled by beams. For this reason, and because we prefer to have access to the source code rather than using canned commercial codes, during this project we also developed a finite element method for plates. This finite element code was validated against NASA LaRC generic transport wing experimental data.

To improve the quality of the flow solver mesh generation for aircraft with extreme wing deformation (wing tip deformation up to 60% of the wing span) a novel grid generation algorithm

was developed using conformal mapping. Conformal mapping, an almost extinct research topic nowadays, has the advantage of generating orthogonal grids, that remain orthogonal even when the wing deforms. Consequently, the accuracy of the computational fluid dynamics (CFD) results improves. In addition, the grid remains topologically identical while the wing/fuselage deforms, which simplifies the parallel communication for the flow solver. The results included in this report show the improved grid quality of the conformal mapping grid compared to a state-of-the-art grid that uses Poisson smoothing.

# Nomenclature

## Roman Letters

$A$	Cross-sectional area
$\mathcal{B}$	Cross section-fixed coordinate system
$B$	Constant in Weinig-Manea transformation
$C$	Damping matrix
$C_{-j}$	complex constants of conformal mapping $z_1(\zeta)$
$c$	Cosine
$e_\eta$	Offset of Centroidal Axis above Elastic Axis along $\eta$ -axis
$e_\zeta$	Offset of Centroidal Axis aft of Elastic Axis along $\zeta$ -axis
$D$	Stiffness
$E$	Young's Modulus
$\mathbf{F}$	Forcing Vector
$G$	Modulus of Rigidity
$j$	Cross-Sectional Mass Moment of Inertia
$K$	Stiffness Matrix Torsion Constant
$L$	Length
$\mathcal{L}$	Lagrangian
$l$	Cross-Sectional Lagrangian Number of $z$ -direction Bending Modes
$M$	Mass Matrix
$m$	Cross-Sectional Mass Number of $y$ -direction Bending Modes
$\mathcal{N}$	Inertial Reference Coordinate System
$n$	Number of Torsional Modes
$Q$	Generalized Non-Conservative Sectional Force
$q$	Generalized Direction
$R$	constant in Weinig-Manea transformation
$s$	Position along Elastic Axis of Beam
$s$	Sine
$T$	Cross-Sectional Kinetic Energy
$\mathcal{T}$	Kinetic Energy
$t$	Time or pitch
$u$	Displacement in $x$ -direction
$V$	Cross-Sectional Potential Energy
$\mathcal{V}$	Potential Energy
$v$	Displacement in $y$ -direction
$v_i$	$y$ -direction Displacement Time coefficient for $i^{th}$ Out-of-plane Mode



${}^N\mathbf{V}$	Inertial Velocity of each Section
$\mathcal{W}$	Virtual Work Resulting from Forces
$\mathcal{W}_b$	$\mathcal{W}_{nc}$ at Boundaries ( $s = 0, L$ )
$\mathcal{W}_c$	Virtual Work Resulting from Conservative Forces
$W_i$	Mode Shape for the $i^{th}$ Bending Mode
$\mathcal{W}_{nc}$	Virtual Work Resulting from Non-Conservative Forces
$w$	Displacement in $z$ -direction
$w_i$	$z$ -direction Displacement Time coefficient for $i^{th}$ In-Plane Mode
$x$	Inertial axis in lengthwise direction
$y$	Inertial axis along plane of fixed end
$z$	Inertial axis along plane of fixed end or complex variable in airfoil domain
$z_1$	Complex variable in domain of the deformed circle
$z_2$	Complex variable in domain of the deformed ellipse

#### Greek Letters

$\delta$	Variational Operator
$\zeta$	Cross section-fixed axis or complex variable in unit circle domain
$\eta$	Cross Section-Fixed Axis
$\theta$	Second Euler Angle Rotation about $y_1$ -axis
$\Lambda$	Sweep Angle
$\lambda$	Lagrangian Multiplier
$\xi$	Cross Section-Fixed Axis
$\rho$	Mass Density
$\boldsymbol{\rho}$	Curvature Vector
$\phi$	Third Euler Angle Rotation about $\xi$ -axis Torsional Displacement
$\phi_i$	Torsional Displacement Time Coefficient for $i^{th}$ Torsional Mode
$\psi$	First Euler Angle Rotation about $z$ -axis
$\omega$	Angular Velocity of the Body Frame, Relative to the Inertial Frame

Primes denote differentiation with respect to  $s$ , while over-dots indicate differentiation with respect to time.

# Chapter 1

## Introduction

Studies of nonlinear fluid-structure interactions have been motivated by evidence that there are adverse aeroelastic responses attributed to system nonlinearities. For example, the flexibility of some new classes of air vehicles leads to large out-of-plane deformations as well as to remarkable in-plane responses (Strganac et al., 2005). In addition, limit-cycle oscillations (LCOs) occur in nonlinear aeroelastic systems and remain a persistent problem on fighter aircraft with store configurations. Such LCOs are unacceptable since aircraft performance, aircraft certification, mission capability, and human factor issues such as pilot fatigue are adversely affected. As a result, high-fidelity nonlinear aeroelastic solvers for aircraft with large wing deformation are needed for current and future air vehicles.

The goal of this project was to develop new techniques for predicting nonlinear aeroelastic responses. To achieve this goal we developed novel methods for: (i) improving the accuracy and efficiency of reduced-order modeling based on the proper orthogonal decomposition (POD) method, (ii) modeling nonlinear structural dynamics, and (iii) improving computational mesh quality for unsteady aerodynamics. This report summarizes these developments.

Chapter 2 presents the improvements of the reduced-order model based on the POD method. The first section describes a set of acceleration techniques that we developed for the POD method. The two most efficient acceleration techniques were included herein: database splitting and a solver for linear systems with quasi-symmetric matrices. The second section presents a new POD method for solving flows with discontinuities, such as shocks.

Chapter 3 presents a novel nonlinear beam model. The first section describes the derivation of the nonlinear equations of motion, followed by the modal representation which details the derivation of the linear and nonlinear mass, stiffness and damping matrices. Section three presents the numerical implementation of the structural solver, followed by solver validation.

Chapter 4 illustrates the use of the continuation method for aeroelasticity applications. The use of the continuation method was facilitated by the development of the nonlinear beam modal representation.

Chapter 5 describes the new grid generator for the flow solver. This chapter includes a section on the conformal mappings used to generate the mesh and a section on grid quality. The latter section compares the grid quality of an algebraic mesh that was improved using a Poisson solver with the quality of the conformal mapping mesh.

## Chapter 2

# Improvements of the Reduced-Order Model based on Proper Orthogonal Decomposition

This chapter presents the improvements done to the POD method during this project. The first section describes two acceleration techniques: (1) database splitting, and (2) a solver for linear systems with quasi-symmetric matrices. The second section presents a new POD method for solving flows with discontinuities, such as shocks. This section describes the method developed for capturing discontinuities using mathematical morphology and a new method that we call the augmented POD method. In the augmented POD method the POD basis modes were augmented by discontinuity modes.

### 2.1 Acceleration Techniques for the Proper Orthogonal Decomposition Method

Proper orthogonal decomposition (POD) was extensively used in aerodynamics for extracting the flow features from either experimental or numerically simulated data. The focus of the work presented herein was to use the POD method to develop a reduced-order model that diminishes the computational cost of a full-order model. It should be noted that when using POD, the name reduced-order model is somewhat misleading, because the results produced by POD reduced-order models are not necessarily lower-fidelity than to those of the full-order models. We have demonstrated that reduced-order models based on POD produce accurate results (shear stress errors less than 1%) for highly nonlinear and rather complicated transport phenomena, such as rotor-stator interaction in turbomachinery (Cizmas and Palacios, 2003) and two-phase flows (Yuan et al., 2005), if enough modes are kept in the POD approximation.

Existing POD implementations (Lieu and Farhat, 2005) reported that the ROM-based simulation was only four times faster than the full-order model simulation. Lieu and Farhat (2005) also reported that if the simulation was limited to 0.5 seconds, the aeroelastic ROM was as computationally intensive as the full-order nonlinear aeroelastic model. In this case, the ROM simulation was beneficial only if longer time-window simulations. We developed reduced-order models using POD for viscous (and two-phase) flows and obtained speedups of two orders of magnitude or more, depending on the imposed accuracy, that is, the number of modes kept in the solution (Cizmas et al., 2008). It is unclear why there is such a large difference between the speedup values reported

by the Colorado/Stanford and Texas A&M teams. It could be that the acceleration techniques reported in (Cizmas et al., 2008) and other practical implementation aspects reported in (Brenner et al., 2009) are responsible for these differences.

The full-order model of the unsteady flow used for the test case utilized for developing acceleration techniques consisted of the Reynolds-averaged Navier-Stokes equations. This full-order model was used to produce the POD basis functions. The energy spectrum for a channel flow with pressure variations of approximately 10% of the maximum pressure value is shown in Fig. 2.1. It should be noted that the amount of energy contained by the first mode is rather large, varying between 48% to 76%. These values are larger than the values obtained for other types of flows, such as turbomachinery flows or two-phase flows in chemical reactors where the energy content of the first mode is less than 30%. Consequently, fewer modes are necessary to capture the flow features for aeroelastic applications, therefore leading to larger speed-up factors.

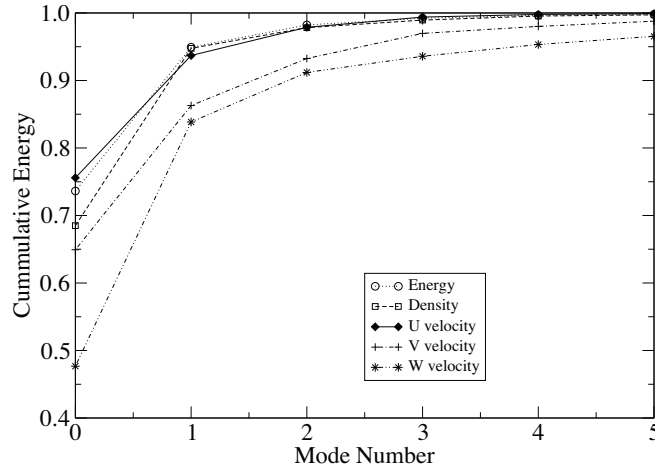


Figure 2.1: Cumulative energy spectrum.

Several acceleration methods of the POD method have been explored. The two most efficient techniques developed during this project are presented herein: (i) an algorithm for splitting the database, and (ii) an algorithm for solving quasi-symmetrical matrices. In addition to these methods, we also investigated: (1) a strategy for reducing the frequency of updating the matrix of the system of equations that generates the time coefficients of the POD, and (2) the influence of the time step adjustment strategy on the computational cost of time integration.

### 2.1.1 Database Splitting

The POD basis functions are extracted from a database of snapshots generated by numerically integrating the governing differential equations of the full-order model. Currently, it is common to use a database that includes all the snapshots. Using a single database that covers the entire time domain, however, could be too restrictive. For example, consider the transience during the start-up of the flow. The large variation in time at start-up requires more modes than are necessary to model the flow features present in the latter part of the simulation. A method to avoid this problem is to split the database of snapshots.

Splitting the database into multiple subsets produces an auto-correlation matrix that contains more relative energy in the first modes. Herein, energy (shown in Fig. 2.1) is defined as the sum of all the POD eigenvalues,  $\lambda_i$ . The relative energy captured by the  $k$ th mode is defined as  $\lambda_k / \sum_{i=1}^M \lambda_i$ . As the relative energy of the first modes increases, fewer POD modes are needed in the reconstruction to approximate the solution. Consequently, the computational cost of the reduced-order model decreases.

Computing the auto-correlation matrix for each database subset is a straightforward process. Determining the bounds of each subset to reduce the computational cost is less trivial. Two methods for the separation of the snapshots into subsets were explored.

The first method measured the time variation of the time coefficients,  $\alpha$ , of the dominant modes of each field variable. The variation of the time coefficients must be calculated and monitored for several modes for every field variable. Monitoring all of these values can, in some cases, produce conflicting information. An alternative to monitoring all five field variables was to monitor only the field variables that most affect the flow. For the aeroelastic case, the flow was most affected by the first modes of velocity in the chordwise direction.

The advantage of this method is that the end of the transient regime can be accurately detected during calculation. The disadvantage of this method is that there is not a unique value that determines the limit of the transience for all five field variables.

The second method proposed for separating the snapshots was to monitor the ratio of the change in CPU time and the change in physical time,  $\Delta t_{CPU} / \Delta t$ . During transience, longer computation times are needed per time step as shown in Fig. 2.2. The advantage of monitoring this parameter is that the time slope is a single value that describes the behavior of all five field variables. The disadvantage of this method is that it over predicts the end of the transience. The magnitude of the slope decreased rapidly until  $t = 0.3$  s and continued to decrease somewhat slower to a quasi-constant value at  $t = 0.45$  s. Placing the end of the transient region at  $t = 0.45$  s is more conservative than the 0.35 s predicted by the first method. Numerical testing showed that database splitting produced a speed-up factor of approximately 1.5.

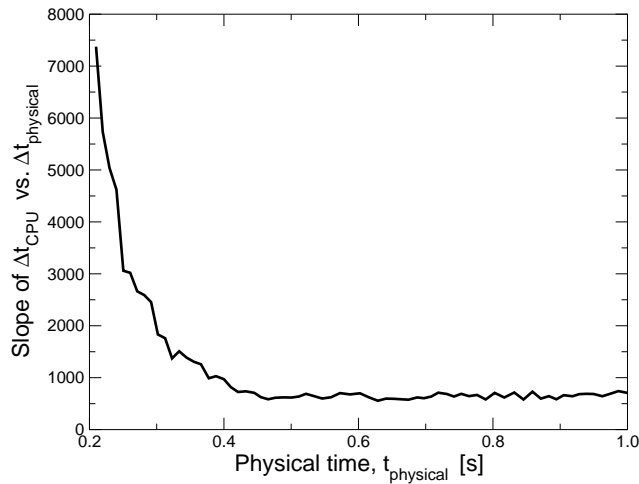


Figure 2.2: Slope of the total CPU time vs physical time measured at 0.01 s increments.

### 2.1.2 Novel Solver for Linear Systems with Quasi-symmetric Matrices

Let us consider the system of equations generated by projecting the mass conservation equation onto the basis functions extracted from an ensemble of  $\rho$  snapshots. This system can be written as (Cizmas, 2007)

$$\tilde{\mathcal{A}}^\rho \alpha^\rho = \tilde{\mathcal{B}}^\rho, \quad (2.1)$$

where  $\alpha^\rho$  is the vector of unknowns  $\alpha_i^\rho$ . The  $\ell k$  element of the  $\tilde{\mathcal{A}}^\rho$  matrix is

$$\tilde{\mathcal{A}}_{\ell k}^\rho = \{\varphi_\ell\}^T [A] \{\varphi_k\} - \sum_{nb=1}^{NB} \{\varphi_\ell\}^T [A_{nb}] \{\varphi_{k_{nb}}\}, \quad \ell, k = 1, \dots, m \quad (2.2)$$

The  $\tilde{\mathcal{A}}^\rho$  matrix is not symmetrical because of the second term  $-\sum_{nb=1}^{NB} \{\varphi_\ell\}^T [A_{nb}] \{\varphi_{k_{nb}}\}$  of the element  $\tilde{\mathcal{A}}_{\ell k}^\rho$ . The matrix would be symmetrical if  $\{\varphi_k\} = \{\varphi_{k_{nb}}\}$ . The difference between the two vectors  $\{\varphi_k\}$  and  $\{\varphi_{k_{nb}}\}$  is small, however, because the latter vector is evaluated at slightly different spatial locations compared to the first vector. Similarly, the systems of linear algebraic equations that resulted from the momentum and energy conservation have matrices that are not symmetrical. These matrices, however, are quite close to being symmetrical, and for this reason will be called quasi-symmetrical. A typical example of a quasi-symmetrical matrix is the  $\tilde{\mathcal{A}}$  matrix obtained for POD approximation with 8 modes (Cizmas, 2007)

$$\tilde{\mathcal{A}} = \begin{vmatrix} 196.4486 & 63.3060 & 6.0469 & 0.5038 & -21.3047 & 11.9071 & 2.3488 & -6.8064 \\ 63.3060 & 903.4807 & -44.1690 & 6.3410 & 14.0286 & -7.4939 & 6.1636 & 19.8724 \\ 6.0459 & -44.1687 & 243.2099 & -20.7951 & -164.8536 & 68.0529 & 19.3275 & -42.8377 \\ 0.5039 & 6.3411 & -20.7953 & 930.9194 & 31.0348 & 20.0166 & 14.3861 & 15.2768 \\ -21.3042 & 14.0288 & -164.8535 & 31.0347 & 890.8742 & 32.1664 & 42.8224 & -23.8698 \\ 11.9068 & -7.4940 & 68.0527 & 20.0167 & 32.1663 & 904.3555 & -10.8230 & 26.7999 \\ 2.3477 & 6.1634 & 19.3267 & 14.3861 & 42.8222 & -10.8228 & 872.6460 & 92.5161 \\ -6.8042 & 19.8722 & -42.8362 & 15.2768 & -23.8695 & 26.7996 & 92.5161 & 763.9839 \end{vmatrix} \quad (2.3)$$

The algorithm proposed herein for solving a system of equations  $Ax = b$ , in which the matrix  $A$  must be positive definite and quasi-symmetrical, begins by splitting the matrix into a symmetrical and a non-symmetrical part (Cizmas, 2007):

$$(A_s + A_n)x = b \quad (2.4)$$

The decomposition of the  $A$  matrix into a symmetrical and non-symmetrical part is not unique. This issue will be discussed later in the section, while for the moment one will consider that one of the possible choices was used to split the  $A$  matrix.

A solution of the symmetrical part is then obtained by solving the system of equations

$$A_s x_s^{(1)} = b \quad (2.5)$$

The solution of (2.4) is decomposed in a component obtained by solving the system (2.5) and a correction needed because the matrix  $A$  is non-symmetrical

$$x = x_s^{(1)} + x_n^{(1)} \quad (2.6)$$

Substituting (2.6) into (2.4) and deducting (2.5) yields

$$\begin{aligned}(A_s + A_n)x_n^{(1)} &= -A_n x_s^{(1)} \quad \text{or} \\ (A_s + A_n)x_n^{(1)} &= b^{(1)}\end{aligned}\tag{2.7}$$

Note that the system of equations (2.7) has the same matrix as (2.4). Consequently, an iterative process can be used to find the solution.  $x_n^{(1)}$  can be considered a correction of the solution  $x_s^{(1)}$  that is needed because the  $A$  matrix is non-symmetrical. The correction  $x_n^{(1)}$  can be split into two components: a component  $x_s^{(2)}$  obtained by solving the system  $A_s x_s^{(2)} = b^{(1)}$  and a correction needed because the matrix  $A$  is non-symmetrical, similarly to the approach used in (2.6):

$$x_n^{(1)} = x_s^{(2)} + x_n^{(2)}\tag{2.8}$$

Substituting (2.8) into (2.7) and using  $A_s x_s^{(2)} = b^{(1)}$  yields

$$(A_s + A_n)x_n^{(2)} = -A_n x_s^{(2)} \quad \text{or}\tag{2.9}$$

$$(A_s + A_n)x_n^{(2)} = b^{(2)}\tag{2.10}$$

This process of approximating the solution yields after  $p$  steps

$$x = x_s^{(1)} + x_s^{(2)} + \dots + x_s^{(p)} + x_n^{(p)},\tag{2.11}$$

where the values  $x_s^{(i)}$ ,  $1 \leq i \leq p$ , are obtained by solving the linear system

$$A_s x_s^{(i)} = b^{(i)},\tag{2.12}$$

where  $b^{(i)} = -A_n x_s^{(i-1)}$ . The iterative process of adding corrections is stopped when  $x_s^{(p)}$  is smaller than an imposed error.

The computation of  $x_s^{(i)}$  requires the solution of the linear system (2.12) several times. The Cholesky decomposition is used for the factorization of the positive-definite symmetrical matrix  $A_s$ . The method takes advantage of the fact that the  $A_s$  is constant and only the right-hand-side vector  $b^{(i)}$  changes.

The method proposed herein replaced the LU decomposition (Press et al., 1992, p. 34) that was previously used to solve the linear algebraic systems (Yuan et al., 2005). For a system with  $m$  equations, the number of operations for the LU decomposition is  $m^3/3$  while the number of operations for the Cholesky decomposition is  $m^3/6$ .

As mentioned previously in this section, the decomposition of the  $A$  matrix into a symmetrical and a non-symmetrical part is not unique. Two decompositions were explored herein in order to evaluate their effect on the convergence of the solver algorithm.

In the first decomposition, the  $A$  matrix,  $a_{ij}$ ,  $i, j = 1, \dots, m$ , was split such that the symmetrical

and non-symmetrical parts were

$$\begin{aligned}
A_s &= \begin{bmatrix} a_{11} & a_{21} & \dots & a_{m1} \\ a_{21} & a_{22} & \dots & a_{m2} \\ \vdots & \vdots & & \vdots \\ a_{m1} & a_{m2} & \dots & a_{mm} \end{bmatrix} \\
A_n &= \begin{bmatrix} 0 & a_{12} - a_{21} & \dots & a_{1m} - a_{m1} \\ 0 & 0 & \dots & a_{2m} - a_{m2} \\ \vdots & \vdots & & \vdots \\ 0 & 0 & \dots & 0 \end{bmatrix}
\end{aligned} \tag{2.13}$$

In the second decomposition, the  $A$  matrix was split into a symmetrical matrix  $A_s$  and skew-symmetrical matrix  $A_n$

$$\begin{aligned}
A_s &= \frac{1}{2}(A + A^T) \\
A_n &= \frac{1}{2}(A - A^T)
\end{aligned} \tag{2.14}$$

These two decompositions were applied to solve the system of equations  $Ax = b$  where the  $A$  matrix was given by (2.3) and the right-hand-side term  $b$  was

$$b = \{-33.601 \ 113.487 \ -8.818 \ 39.586 \ -21.221 \ 33.225 \ -49.507 \ 17.622\}^T.$$

For an imposed error of  $10^{-9}$ , the iterative solver algorithm converged for both decompositions in three steps. The vector of corrections  $x_s^{(i)}$ , shown in Table 2.1, indicates that in these cases the matrix decomposition had a minimal effect on the convergence. The Euclidean norm of the relative error between the solutions obtained using the two decompositions was  $8.9 \cdot 10^{-31}$ .

Numerical tests showed that three to four  $x_s^{(i)}$  terms in (2.11) were usually sufficient to obtain a solution with an error less than  $10^{-6}$ . Consequently, three to four  $x_s^{(i)}$  solutions of the linear algebraic system of equations (2.12) must be computed. Since only the right-hand-side term  $b^{(i)}$  changes while the matrix  $A_s$  is constant, the number of operations for the proposed method was increased by a factor proportional to  $m^2$  multiplied by the number of  $x_s^{(i)}$  terms in (2.11). As long as  $m$  is larger than 4, the computational cost of the proposed method is approximately half that of the LU decomposition.

The magnitude of the non-symmetrical terms was gradually increased in numerical tests. Herein, the degree of non-symmetry was defined as (Li et al., 2003)

$$\eta = \|A - A^T\|_F / \|A + A^T\|_F$$

where  $\| \cdot \|_F$  indicates the Frobenius (or the Hilbert-Schmidt) norm (Golub and van Loan, 1989, p. 56). The solution of the  $Ax = b$  system mentioned above was computed for three error levels:  $10^{-6}$ ,  $10^{-9}$ , and  $10^{-12}$ . The  $A$  matrix was decomposed using split option 1 (2.13). The degree of non-symmetry of the  $A$  matrix was increased by multiplying the non-symmetric matrix  $A_s$  by different factors  $X$ , ranging from 1 to  $5 \cdot 10^8$ . The variation of the degree of non-symmetry of matrix  $A$  as a function of the factor  $X$  is shown in Fig. 2.3.

The variation of the number of iterations needed for convergence as a function of the degree of non-symmetry  $\eta$  is shown in Fig. 2.4(a). It is remarkable that five or less iterations are needed for the convergence of the solution for degree of non-symmetry  $\eta = 0.01$  that corresponds to a



Table 2.1: Vector of corrections  $x_s^{(i)}$  corresponding to matrix (2.3) for decompositions (2.13) and (2.14).

	Split 1 (2.13)			Split 2 (2.14)		
	$x_s^{(1)}$	$x_s^{(2)}$	$x_s^{(3)}$	$x_s^{(1)}$	$x_s^{(2)}$	$x_s^{(3)}$
1	0.2205E+00	-0.5529E-06	0.7659E-12	0.2205E+00	-0.3159E-06	-0.3772E-11
2	-0.1401E+00	0.3505E-07	-0.1631E-12	-0.1401E+00	0.4948E-07	0.2289E-12
3	0.3053E-01	-0.2586E-06	-0.3920E-12	0.3053E-01	0.3431E-06	-0.2669E-11
4	-0.4188E-01	-0.1645E-07	0.8489E-14	-0.4188E-01	0.1406E-07	0.5404E-14
5	0.3669E-01	-0.8025E-07	-0.6626E-13	0.3669E-01	-0.2367E-07	-0.6342E-12
6	-0.4223E-01	0.4975E-07	0.3221E-13	-0.4223E-01	0.4024E-07	0.3478E-12
7	0.5685E-01	0.1344E-07	0.1147E-13	0.5685E-01	0.1726E-06	0.6542E-13
8	-0.1916E-01	-0.2588E-07	-0.1567E-13	-0.1916E-01	-0.4003E-06	-0.9619E-13

multiplying factor  $X = 10,000$ . The number of iterations increased to approximately 20 for  $\eta$  larger than 0.1 which correspond to multiplying factors larger than  $10^5$ . Certainly at these large  $X$  values the matrix is far from a quasi-symmetric matrix. If the multiplying factor  $X$  is further increased, the matrix is no longer positive definite and the algorithm cannot be used because it relies on the Cholesky decomposition.

The Eulerian norm of the difference between the solution obtained using the LU decomposition and the method proposed herein is shown in Fig. 2.4(b) as a function of the degree of non-symmetry  $\eta$ . The norm of the difference increases as the degree of non-symmetry increases. The norm of difference is, however, smaller than  $10^{-10}$  even for values of  $\eta$  as large as 0.1. Consequently, the method can be applied to a larger class of matrices than just matrices obtained in the proper orthogonal decomposition method, as long as these matrices are positive definite.

## 2.2 Proper Orthogonal Decomposition Method for Flows with Discontinuities

### 2.2.1 Augmented Proper Orthogonal Decomposition Method

The large computational time of full-order model solutions of high-fidelity, unsteady aerodynamics is a limiting factor for parametric studies in aeroelasticity. Note that in aeroelasticity, the term high-fidelity aerodynamic models currently means Reynolds-averaged Navier-Stokes solvers. To decrease computational time, reduced-order models are being developed. As illustrated above, a

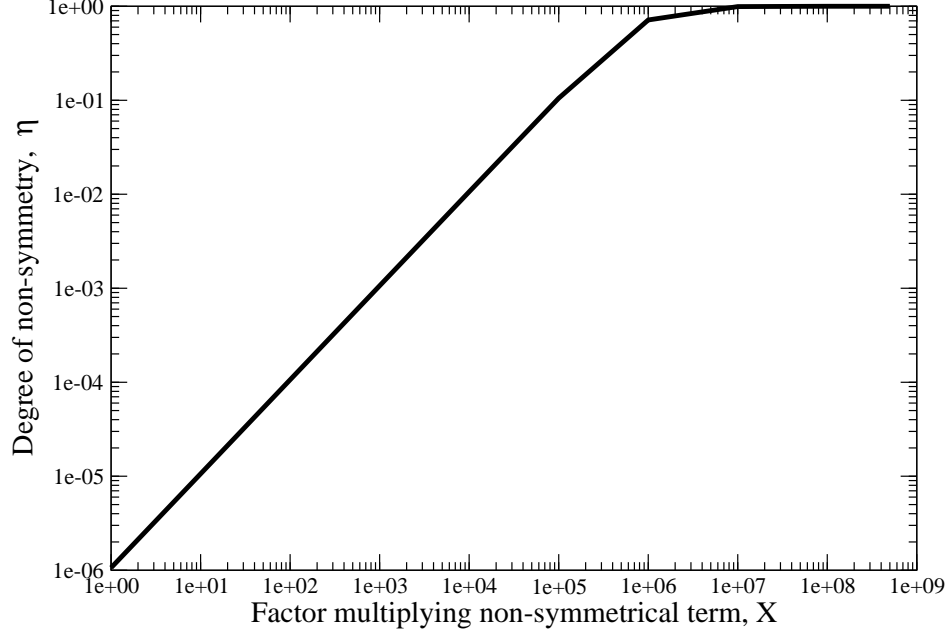


Figure 2.3: Degree of non-symmetry  $\eta$  as a function of the multiplying factor  $X$ .

promising reduced-order model is based on proper orthogonal decomposition (POD). This section presents a new POD approach that can better model flows with discontinuities, such as shock waves.

POD is a method for extracting spatially dependent orthogonal basis functions,  $\{\varphi(\mathbf{x})\}$  and time dependent orthonormal amplitude coefficients,  $\{\alpha(\mathbf{t})\}$ , from a function  $u(\mathbf{x}, \mathbf{t})$  that varies in both time and space. The function is usually parametrized by time to form a collection of  $M$  snapshots,  $u(\mathbf{x}, t_k), k \in [0, M]$ . In the POD approximation,

$$u(x, t) = \sum_{j=0}^m \alpha_j(t_k) \varphi_j(x), \quad m \leq M - 1,$$

the basis functions are computed such that the average least-squares truncation error

$$\varepsilon_m = \left\langle \left\| u(\mathbf{x}, t_k) - \sum_{j=0}^m \alpha_j(t_k) \varphi_j(\mathbf{x}) \right\|^2 \right\rangle$$

is a minimum. Here  $\|\cdot\|$  denotes the  $L^2$ -norm given by  $\|f\| = (f, f)^{\frac{1}{2}}$ ,  $(\cdot, \cdot)$  denotes the Euclidean inner product, and  $\langle \cdot \rangle$  denotes an ensemble average over the number of observations,  $\langle f \rangle = \sum_{k=1}^M f(\mathbf{x}, t_k) / M$  (Holmes et al., 1996).

The current POD methods produce unphysical oscillations for flows with moving discontinuities. These oscillations are due to dispersion errors caused by the superposition of modes of increasing frequency. This phenomenon is well known and is often referred to as the Gibbs phenomenon.

Lucia *et al.* (Lucia et al., 2003) have studied the problem of modeling flows with moving shocks using the POD method. They have proposed a domain decomposition method where the spatial domain was divided into areas where shocks were possible and where shocks were not possible. A

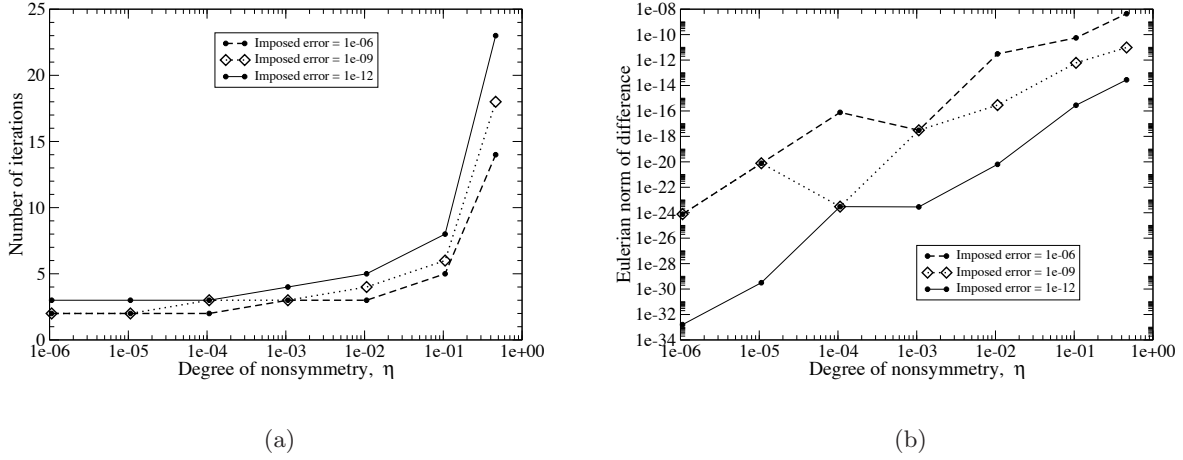


Figure 2.4: Effect of degree of non-symmetry on: (a) number of iterations, and (b) Eulerian norm of difference between the solutions of the LU decomposition and the present method.

full-order model was solved where shocks were possible and the rest of the domain was solved using a POD-based reduced-order model (ROM). This method is somewhat inefficient, particularly when a shock travels through a large portion of the spatial domain.

To better model flows with discontinuities, we propose augmenting the POD database with a set of discontinuity modes. The purpose of the discontinuity modes is to capture the moving discontinuities exactly, without the need for domain decomposition. The POD approximation can then be expressed as

$$u(\mathbf{x}, t_k) = \sum_{j=0}^m \alpha_j(t_k) \varphi_j(\mathbf{x}) + \sum_{\ell=1}^{m_A} \beta_\ell(t_k) \psi_\ell(\mathbf{x}, t_k), \quad (2.15)$$

where  $\psi_\ell$  are the discontinuity modes and  $\beta_\ell$  their time coefficients.

Note that since the POD method is guaranteed to produce orthogonal basis functions, the POD basis functions are linearly independent. The discontinuity modes, however, are not guaranteed to be linearly independent of the POD modes. Therefore, one must verify the linear independence of the discontinuity modes by appending them to the POD modal matrix and computing the singular values. As long as the smallest singular value is larger than a small number, the appended modes are linearly independent.

To illustrate the augmented POD approach we will use the first-order wave equation

$$\frac{\partial u}{\partial t} + c \frac{\partial u}{\partial x} = 0, \quad (2.16)$$

which is the simplest model for a moving discontinuity. This simple model was chosen to test the augmented POD method due to the ease of predicting the discontinuity locations

$$x_{s,\ell}(t_i) = x_{s,\ell}(t=0) + ct_i.$$

Here the discontinuity modes are defined as

$$\psi_\ell(x, t_i) = \begin{cases} 1 & x \leq x_{s,\ell}(t_i) \\ 0 & x > x_{s,\ell}(t_i) \end{cases}$$

where  $x_{s,\ell}(t_i)$  is the location of the  $\ell$ -th discontinuity at time  $t = t_i$ .

Substituting (2.15) into (2.16) yields

$$\begin{aligned} \sum_{j=1}^m \dot{\alpha}_j(t_k) \varphi_j(\mathbf{x}) + \sum_{\ell=1}^{m_a} \dot{\beta}_\ell(t_k) \psi_\ell(\mathbf{x}, t_k) + \sum_{\ell=1}^{m_a} \beta_\ell(t_k) \dot{\psi}_\ell(\mathbf{x}, t_k) \\ + c \sum_{j=0}^m \alpha_j(t_k) \varphi'_j(\mathbf{x}) + \sum_{\ell=1}^{m_a} \beta_\ell(t_k) \psi'_\ell(\mathbf{x}, t_k) = 0 \end{aligned} \quad (2.17)$$

where  $u' := \frac{\partial u}{\partial x}$  and  $\dot{u} := \frac{\partial u}{\partial t}$  are used for the spatial and temporal derivatives, respectively.

A ROM was constructed by doing a Galerkin projection of (2.17) onto the augmented basis functions, which produced a system of ordinary differential equations (ODEs)

$$[A] \begin{Bmatrix} \dot{\alpha} \\ \dot{\beta} \end{Bmatrix} + [B] \begin{Bmatrix} \alpha \\ \beta \end{Bmatrix} + \{d\} = \{0\}, \quad (2.18)$$

where  $[A] \in \mathbb{R}^{m+m_a} \times \mathbb{R}^{m+m_a}$ ,  $\{\alpha\} \in \mathbb{R}^m$ ,  $\{\beta\} \in \mathbb{R}^{m_a}$  and  $\{d\} \in \mathbb{R}^{m+m_a}$ . The ODE system (2.18) was solved using a Runge-Kutta-Fehlberg routine (Fehlberg, 1969). Further details of the implementation are given in (Brenner et al., 2009).

For this test case, the initial velocity profile was a simple quadratic function

$$u(x, t) = a + b(x - ct) + d(x - ct)^2.$$

A single discontinuity was introduced in the initial condition according to

$$u(x, t = 0) = \begin{cases} a + bx + dx^2 + 1 & x \leq x_{s,1}(t = 0), \\ a + bx + dx^2 & x > x_{s,1}(t = 0). \end{cases}$$

Since only one discontinuity is present in the flow, only one discontinuity mode was needed, *i.e.*,  $m_a = 1$ .

Figure 2.5 shows the velocity profile after one time unit for a full-order model, a POD-based ROM with no augmentation and a POD-based ROM with augmentation. The full-order model solution was computed using an explicit finite difference method that was first-order accurate in space and time and shows some numerical dissipation around the discontinuity. The ROM without augmentation shows the characteristic oscillations of the Gibbs phenomenon. The ROM with augmentation produces the best results, showing a crisp representation of the discontinuity with only one POD mode and one discontinuity mode.

## 2.2.2 Discontinuities Capturing using Mathematical Morphology

The POD acceleration methods resulted in a reduction of the computational time of two orders of magnitude compared to the full-order model (Cizmas et al., 2008), as mentioned in the previous section. In spite of the speed-up values, the effectiveness of the proper orthogonal decomposition

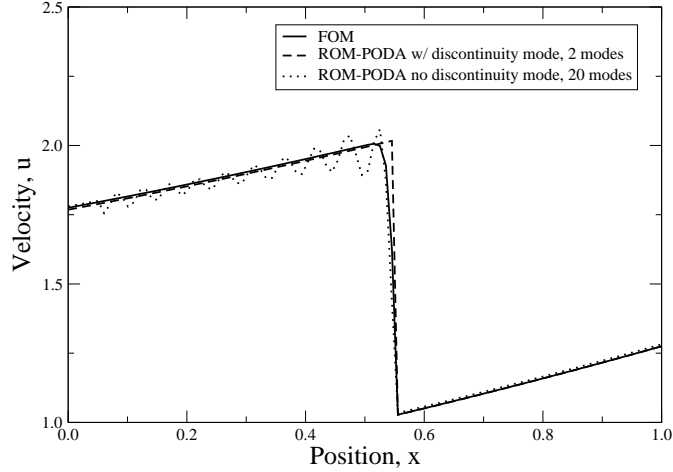


Figure 2.5: Velocity profile at  $t = 1.0$  for full-order model, reduced-order model with 20 modes and no discontinuity mode, and reduced-order model with 2 modes, including a discontinuity mode (Brenner et al., 2009).

method is challenged by the presence of flow discontinuities, such as shock waves (Lucia et al., 2003). To improve POD robustness and performance when dealing with discontinuities, such as shock waves, we developed a POD method in which the basis functions were augmented by discontinuity basis functions, as shown in 2.2.1. The discontinuity basis functions were generated by detecting the flow discontinuities in the full-order model using a morphology method. This section presents the methodology we used to detect these discontinuities.

Developed in the 1960's by Georges Matheron and Jean Serra at the Ecole des Mines de Paris, France, mathematical morphology is a method for the analysis of spatial structures (Soille, 2003). Morphology is heavily based on set theory, integral geometry, and lattice algebra. Morphology was originally developed to describe porous media, where the porous material can be characterized as a binary image containing pores or solid surrounding material (Soille, 2003). While this method has primarily been used in the image processing community, it also has been used on a wide variety of spatial structures. Herein the theory and application of morphology is extended to locating discontinuities in flows.

Morphology attempts to extract structures of interest located within the whole spatial domain, herein referred to as an image, by performing various set operations over so-called structuring elements. Structuring elements are used to probe the image with various shapes that describe the structure of interest. Structuring elements can take on any number of shapes, from simple rods (straight elements) to circles, or in extreme cases, galaxy shapes. Structuring elements can also be applied in combinations to create larger structuring elements of varying shapes. While there is not a limitation to what shapes or size the structuring elements can take, these structuring elements must be aligned in the same direction throughout the image. Failure to maintain the same alignment throughout will distort the structures that are sought. In addition, structuring elements can only be applied to highly structured images. Images not in a highly structured state must be transformed to this state before applying the morphological operations as usual.

The structuring element, denoted as  $b$ , is a locally defined quantity in the local coordinates  $(k, l)$ . The values of  $(k, l)$  are defined depending on the total size of the structuring element. If  $(0, 0)$  is the point of interest in local  $(k, l)$  coordinates, then for a five point vertical rod structuring element the global coordinates would be  $(i, j - 2l)$ ,  $(i, j - l)$ ,  $(i, j)$ ,  $(i, j + l)$ , and  $(i, j + 2l)$ .  $b$  assumes the value of the image,  $f$ , at these coordinates.

While morphology can perform a wide variety of operations over the structuring elements, all of these operations can be described by combinations of two elementary operations: erosion and dilation. Both of these operations can be described as shifts in the data set. Erosion is the minimum of these shifts of the image,  $f(i, j)$ , over the structuring element,  $b(k, l)$ , given as

$$e(f) = \min(f(i + k, j + l) - b(k, l)). \quad (2.19)$$

Dilation is the maximum of these shifts over the same structuring element,

$$d(f) = \max(f(i - k, j - l) + b(k, l)). \quad (2.20)$$

Using equations (2.19) and (2.20) in conjunction, more powerful operations can be performed. While these operations are not inherently morphological in nature, they are useful for detecting discontinuities in flows. These operations include blurring, blur/erosion, dilation/blur, and thresholding.

Blurring is used in image processing as a noise reduction technique. This operation is required for a preliminary elimination of extreme values. Blurring is also required for locating step-type edges (Lee et al., 1987). Without blurring, the area around a step edge is not a local maximum or minimum, and the erosion and dilation operations will not extract discontinuities of that type (Lee et al., 1987). Blurring is defined as

$$blur(f) = \frac{\sum_{p=i-L}^{i+L} f(p)}{K} \quad L = \frac{K-1}{2}. \quad (2.21)$$

Here blurring is defined over the reduced stencil size of nodes,  $K$ .

While blurring is necessary, using a reduced stencil that is too large will over-blur the image, resulting in overly distorted edges that are impossible to discern. A good reduced stencil size for blurring is  $K = 3$  (Lee et al., 1987); *i.e.*, when using a vertical rod structuring element and looking at the center point, the values used to blur the center point are, in global coordinates:  $(i, j - l)$ ,  $(i, j)$ , and  $(i, j + l)$ . A consequence of this stencil size for blurring is that the structuring elements must be at least two elements larger than the blurring stencil in order to mitigate possible over-distortion of the edges.

The blur/erosion ( $be$ ) and dilation/blur ( $db$ ) operators were proposed by Lee et al. (1987). These operations act over the structuring elements and are used to eliminate obvious points where edges are not located using the standard erosion and dilation operations in conjunction with blurring. These combination operators initially blur the image and then apply the erosion and dilation operators to the blurred image. The  $be$  and  $db$  operators are defined as

$$be(f) = blur(f) - e(blur(f)) \quad (2.22)$$

and

$$db(f) = d(blur(f)) - blur(f), \quad (2.23)$$

respectively.

The last operation required to detect edges is thresholding. Thresholding is an image segmentation technique used to isolate areas of interest in the image. For non-binary images, thresholding is almost always required to completely extract the desired information from the image. Grayscale images can take on a wide variety of values, causing the previously described operations to assign more than two points to an edge, where the edge is defined as being only two points in width; thresholding ensures that each edge is only two points in width. Thresholding can be applied globally or semi-globally, where globally is a binary fix to the image and semi-globally maintains the original value of the edge. We use global thresholding, defined as (Ritter and Wilson, 2000)

$$thres(f) = \begin{cases} 1 & \alpha \leq f \leq \beta \\ 0 & \text{otherwise} \end{cases}$$

The constants  $\alpha$  and  $\beta$  are user defined values specific for the image or set of images if the group of images describe the same general phenomenon.

All of the previously described operations, when combined, allow for the detection of edges in images with two-point edge strength. The algorithm for edge detection, described by Lee et al. (1987), is adapted here for multiphase flow.

1. Read in the images with discontinuities to be detected.
2. Create the structuring elements. Herein, we used four rod-type structuring elements that are five units in length and have the following orientations: horizontal, vertical, and diagonal (45 and 135 degrees with respect to the horizontal).
3. Blur the image using Equation (2.21) with  $K = 3$ .
4. Compute the erosion and dilation of the blurred images using equations (2.19) and (2.20).
5. Compute values of the blur/erosion and dilation/blur operators with equations (2.22) and (2.23).
6. Determine the maximum values of the  $be$  and  $db$  operators

$$\max(be_i(f)) \quad i = 1, \dots, 4$$

and

$$\max(db_i(f)) \quad i = 1, \dots, 4.$$

where  $i$  represents each of the four structuring elements.

7. Determine the edge strength

$$Indicator(f) = \min(\max(db(f)), \max(be(f))). \quad (2.24)$$

8. Apply the global thresholding to the images given by Equation (2.24). This gives edges for the discontinuity that are only two points in width.

The method developed to detect discontinuities was tested on an airfoil operating at Mach 0.85. Figure 2.6 shows the edge strength index (2.24) contours. This indicator captures not only the shock discontinuity shown in Fig. 2.7 but also the discontinuities due to the vortex shedding and the interaction between the shock and the boundary layer. The discontinuities were detected with two-point accuracy.

Mathematical morphology was shown to extract key features of the flow by using a simple set of operations. Regardless of the original grid arrangement of the data, the morphological detection algorithm captured the discontinuities.

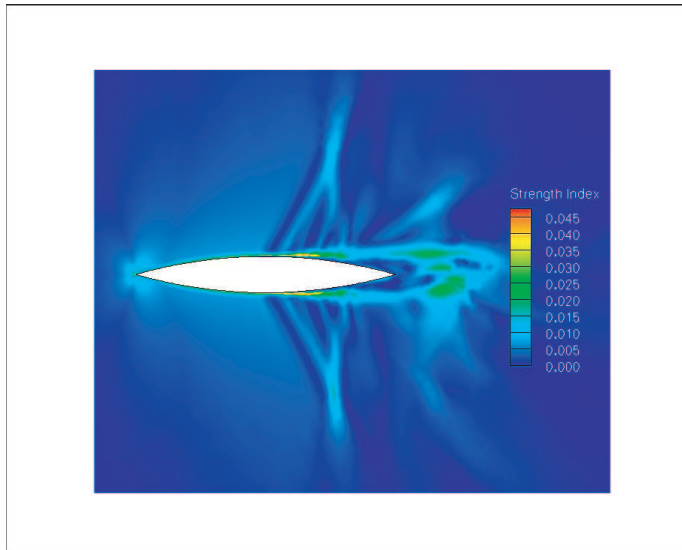


Figure 2.6: Edge strength index.

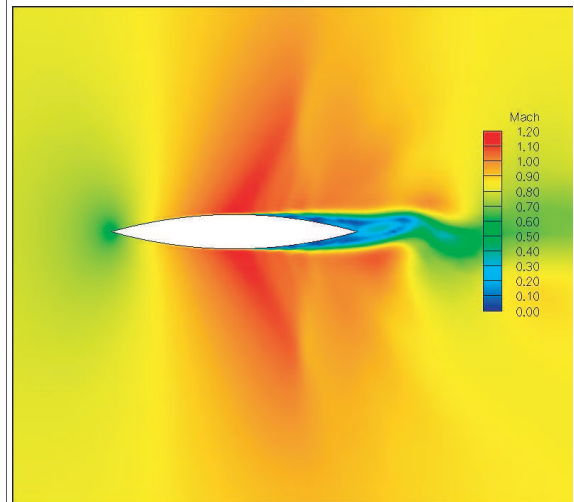


Figure 2.7: Mach number contours.



## Chapter 3

# A Novel Nonlinear Beam Model

This chapter presents the development of a novel nonlinear beam model. This work was motivated by the need to reduce the computational time for structural modeling and to allow us to use continuation methods. The first section presents the derivation of the nonlinear equations of motion, followed by the modal representation of the beam. The third section describes the numerical implementation of the nonlinear beam solver, followed by the solver validation. The last section briefly presents the development of a finite element method code for plates that was needed to avoid using canned commercial codes and to maintain control of the source code while doing aeroelastic simulations.

### 3.1 Derivation of the Nonlinear Equations of Motion

#### 3.1.1 Overview

In this section, the nonlinear flexural-flexural-torsional equations of motion are derived for a beam with a straight elastic axis, along which the cross sections can vary arbitrarily and abruptly. The cross sections of the undeformed beam can have a center of mass offset from the elastic axis and the principal centroidal and bending axes variably and uniquely rotated about the elastic axis. Finally, due to the consistent retention of nonlinear terms, the equations are valid for large deformations, within the scope of the validity of elasticity.

#### 3.1.2 Definition of Parameters

The beam is assumed to have an elastic axis that is straight when undeformed. The inertial reference coordinate system  $\mathcal{N}(x, y, z)$  is located at the fixed end of the beam, where the  $x$ -axis is coincident with the undeformed elastic axis and positive in the direction of the free end. The cross-sectional coordinate system  $\mathcal{B}(\xi, \eta, \zeta)$  is fixed to each cross section during deformation. When the beam is undeformed, the cross-sectional coordinate system is parallel to the reference coordinate system. To describe the orientation of the cross-sectional coordinate system relative to the reference coordinate system, three Euler angle rotations are invoked. The inertial frame is rotated an angle  $\psi$  about the  $z$ -axis,  $\theta$  about the first intermediate  $y$ -axis, and  $\phi$  about the second intermediate  $x$ -axis, which is in turn the  $\xi$ -axis. Each of these angles is a function of time  $t$  and position  $s$  along the deformed elastic axis. These coordinate systems and transformations are similar to those used in [Crespo da Silva and Glynn \(1978a\)](#). Figure 3.1 illustrates the two coordinate systems.

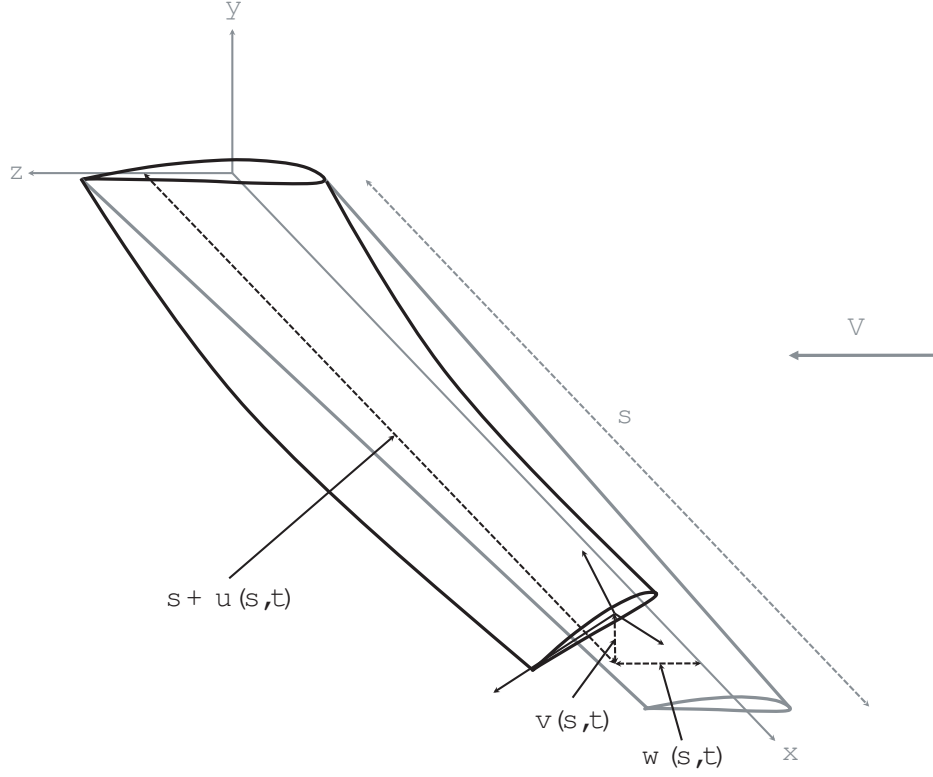


Figure 3.1: Diagram of Deformed Beam

To characterize the beam, the following parameters are used.

$$m(s) = \iint_A \rho d\eta d\zeta \quad (3.1a)$$

$$j_\xi(s) = \iint_A \rho (\eta^2 + \zeta^2) d\eta d\zeta \quad (3.1b)$$

$$j_\eta(s) = \iint_A \rho \zeta^2 d\eta d\zeta \quad (3.1c)$$

$$j_\zeta(s) = \iint_A \rho \eta^2 d\eta d\zeta \quad (3.1d)$$

$$j_{\eta\zeta}(s) = - \iint_A \rho \eta \zeta d\eta d\zeta \quad (3.1e)$$

$$D_\xi(s) = GK \quad (3.1f)$$

$$D_\eta(s) = \iint_A E \zeta^2 d\eta d\zeta \quad (3.1g)$$

$$D_\zeta(s) = \iint_A E \eta^2 d\eta d\zeta \quad (3.1h)$$

$$D_{\eta\zeta}(s) = - \iint_A E \eta \zeta d\eta d\zeta \quad (3.1i)$$

In this report, nonlinearities will be described by an order that will indicate how many factors of the displacements  $u$ ,  $v$ ,  $w$ , and  $\phi$  comprise a term. These factors may include spatial and/or time derivatives of the displacements.

### 3.1.3 The Lagrangian

The angular velocity expressed in the cross-sectional frame is

$$\boldsymbol{\omega}(s, t) = \left\{ \begin{array}{c} \dot{\phi} - \dot{\psi} \sin \theta \\ \dot{\psi} \cos \theta \sin \phi + \dot{\theta} \cos \phi \\ \dot{\psi} \cos \theta \cos \phi - \dot{\theta} \sin \phi \end{array} \right\}_{\mathcal{B}} = \left\{ \begin{array}{c} \omega_{\xi} \\ \omega_{\eta} \\ \omega_{\zeta} \end{array} \right\}_{\mathcal{B}}. \quad (3.2)$$

Love's kinetic analogy (Crespo da Silva and Glynn, 1978a; Love, 1944) enables the curvature vector to be calculated in a manner similar to that of the angular velocity, replacing temporal differentiation with spatial differentiation:

$$\boldsymbol{\rho}(s, t) = \left\{ \begin{array}{c} \phi' - \psi' \sin \theta \\ \psi' \cos \theta \sin \phi + \theta' \cos \phi \\ \psi' \cos \theta \cos \phi - \theta' \sin \phi \end{array} \right\}_{\mathcal{B}} = \left\{ \begin{array}{c} \rho_{\xi} \\ \rho_{\eta} \\ \rho_{\zeta} \end{array} \right\}_{\mathcal{B}}. \quad (3.3)$$

One of the fundamental assumptions of the beam model is that cross sections perpendicular to the elastic axis remain perpendicular and rigid. The inertial velocity of each point on a cross section of the beam can be decomposed into the sum of the velocity of the intersection of the elastic axis with that cross section and the velocity of the point on the cross section, relative to the intersection:

$$\mathbf{V} = \left\{ \begin{array}{c} \dot{u} \\ \dot{v} \\ \dot{w} \end{array} \right\}_{\mathcal{N}} + \boldsymbol{\omega} \times \left\{ \begin{array}{c} 0 \\ \eta \\ \zeta \end{array} \right\}_{\mathcal{B}}. \quad (3.4)$$

Resolving the second velocity contribution into the inertial frame provides

$$\mathbf{V} = \left\{ \begin{array}{l} (\zeta\omega_{\eta} - \eta\omega_{\zeta}) c\psi c\theta + \eta\omega_{\xi} (s\phi s\psi + c\phi c\psi s\theta) + \zeta\omega_{\xi} (c\phi s\psi - c\psi s\phi s\theta) + \dot{u} \\ (\zeta\omega_{\eta} - \eta\omega_{\zeta}) s\psi c\theta - \eta\omega_{\xi} (s\phi c\psi - c\phi s\psi s\theta) - \zeta\omega_{\xi} (c\phi c\psi + s\psi s\phi s\theta) + \dot{v} \\ - (\zeta\omega_{\eta} - \eta\omega_{\zeta}) s\theta + \eta\omega_{\xi} c\phi c\theta - \zeta\omega_{\xi} s\phi c\theta + \dot{w} \end{array} \right\}_{\mathcal{N}} \quad (3.5)$$

Correspondingly, the cross-sectional kinetic energy is determined by

$$T = \frac{1}{2} \iint_A \rho \mathbf{V} \cdot \mathbf{V} d\eta d\zeta, \quad (3.6)$$

which, when expanded, simplifies to

$$\begin{aligned} T = & \frac{1}{2} m (\dot{u}^2 + \dot{v}^2 + \dot{w}^2) + \frac{1}{2} (j_{\xi} \omega_{\xi}^2 + j_{\eta} \omega_{\eta}^2 + j_{\zeta} \omega_{\zeta}^2) + j_{\eta\zeta} \omega_{\eta} \omega_{\zeta} \\ & + m e_{\zeta} \omega_{\xi} [(c\phi s\psi - s\phi c\psi s\theta) \dot{u} - (s\phi s\psi s\theta + c\phi c\psi) \dot{v} - s\phi c\theta \dot{w}] \\ & + m e_{\zeta} \omega_{\eta} [c\psi c\theta \dot{u} + c\theta s\psi \dot{v} - s\theta \dot{w}] \\ & + m e_{\eta} \omega_{\xi} [(s\phi s\psi + c\phi c\psi s\theta) \dot{u} + (c\phi s\psi s\theta - s\phi c\psi) \dot{v} + c\phi c\theta \dot{w}] \\ & - m e_{\eta} \omega_{\zeta} [c\psi c\theta \dot{u} + c\theta s\psi \dot{v} - s\theta \dot{w}]. \end{aligned} \quad (3.7)$$

Additionally, the potential energy of each cross section is

$$V = \frac{1}{2} (D_{\xi} \rho_{\xi}^2 + D_{\eta} \rho_{\eta}^2 + D_{\zeta} \rho_{\zeta}^2) + D_{\eta\zeta} \rho_{\eta} \rho_{\zeta}. \quad (3.8)$$

With the kinetic and potential energy for each cross section known, the cross-sectional Lagrangian

is simply

$$l = T - V. \quad (3.9)$$

### 3.1.4 Inextensionality Constraint

It is assumed that the length of the beam, specifically the elastic axis, remains constant during deformation. Applying the Pythagorean theorem to an infinitesimal length  $ds$  of the beam yields

$$ds^2 = dv^2 + dw^2 + (ds + du)^2 \quad (3.10)$$

or

$$1 = v'^2 + w'^2 + (1 + u')^2. \quad (3.11)$$

Furthermore, this constraint enables  $\psi$  and  $\theta$  to be expressed in terms of the derivatives of the displacement:

$$\psi = \tan^{-1} \frac{v'}{1 + u'} \quad (3.12)$$

$$\theta = \tan^{-1} \frac{-w'}{\sqrt{(1 + u')^2 + v'^2}} \quad (3.13)$$

### 3.1.5 Hamilton's Principle

With the Lagrangian known for each cross section and multiplying the inextensionality constraint by a Lagrange multiplier, the extended form of Hamilton's principle provides the governing equations of motion associated with the variations  $\delta u$ ,  $\delta v$ ,  $\delta w$ , and  $\delta \phi$  (Crespo da Silva and Glynn, 1978a; Meirovitch, 1967). These are derived in Appendix A and presented below:

$$G'_u = \left[ A_\psi \frac{\partial \psi}{\partial u'} + A_\theta \frac{\partial \theta}{\partial u'} + \lambda (1 + u') \right]' = \frac{\partial^2 l}{\partial t \partial \dot{u}} - Q_u \quad (3.14)$$

$$G'_v = \left[ A_\psi \frac{\partial \psi}{\partial v'} + A_\theta \frac{\partial \theta}{\partial v'} + \lambda v' \right]' = \frac{\partial^2 l}{\partial t \partial \dot{v}} - Q_v \quad (3.15)$$

$$G'_w = \left[ A_\theta \frac{\partial \theta}{\partial w'} + \lambda w' \right]' = \frac{\partial^2 l}{\partial t \partial \dot{w}} - Q_w \quad (3.16)$$

$$A_\phi = Q_\phi, \quad (3.17)$$

where

$$A_\alpha = \frac{\partial^2 l}{\partial t \partial \dot{\alpha}} + \frac{\partial^2 l}{\partial s \partial \alpha'} - \frac{\partial l}{\partial \alpha} \quad (\alpha = \psi, \theta, \phi). \quad (3.18)$$

The above equations are simplified by carrying out the following substitutions and Taylor series expansions:

$$\psi = \tan^{-1} \frac{v'}{1 + u'} \approx v' \left( 1 + \frac{v'^2}{6} + \frac{w'^2}{2} \right) \quad (3.19a)$$

$$\frac{\partial \psi}{\partial u'} = \frac{-v'}{(1+u')^2 + v'^2} \approx -v' \quad (3.19b)$$

$$\frac{\partial \psi}{\partial v'} = \frac{(1+u')}{(1+u')^2 + v'^2} \approx 1 - \frac{v'^2}{2} + \frac{w'^2}{2} \quad (3.19c)$$

$$\theta = \tan^{-1} \frac{-w'}{\sqrt{(1+u')^2 + v'^2}} \approx -w' \left( 1 + \frac{w'^2}{6} \right) \quad (3.19d)$$

$$\frac{\partial \theta}{\partial u'} = \frac{w' (1+u')}{\sqrt{(1+u')^2 + v'^2}} \approx w' \quad (3.19e)$$

$$\frac{\partial \theta}{\partial v'} = \frac{v' w'}{\sqrt{(1+u')^2 + v'^2}} \approx v' w' \quad (3.19f)$$

$$\frac{\partial \theta}{\partial w'} = -\sqrt{(1+u')^2 + v'^2} \approx -1 + \frac{w'^2}{2} \quad (3.19g)$$

$$u' = -\frac{1}{2} (v'^2 + w'^2) \quad (3.19h)$$

$$u = -\frac{1}{2} \int_0^s (v'^2 + w'^2) d\hat{s}. \quad (3.19i)$$

The terms in the extensional equation (3.14) are expanded in Taylor series to quadratic order, and the terms in the bending and torsional equations (3.15)-(3.17) are expanded to cubic order. The extensional equation only requires quadratic order as it is used to determine  $\lambda$ , which only appears when multiplied by a spatial derivative of a displacement in the bending equations.

### 3.1.6 Application of the Galerkin Method

Invoking the Galerkin method facilitates discretization of the beam, particularly with regard to abrupt property changes along the length. For a linear cantilevered beam, the boundary conditions are known (Bisplinghoff et al., 1996). For the case of the nonlinear beam, the boundary conditions remain the same and are obtained from the boundary components resulting from integration by parts of Hamilton's principle (Crespo da Silva and Glynn, 1978b).

#### 3.1.6.1 Bending Equations of Motion

The following set of mode shapes (Bisplinghoff et al., 1996) is used when applying the Galerkin method to the bending equations of motion.

$$W_i(s) = \cosh\left(\frac{\beta_i s}{L}\right) - \cos\left(\frac{\beta_i s}{L}\right) - \sigma_i \left[ \sinh\left(\frac{\beta_i s}{L}\right) - \sin\left(\frac{\beta_i s}{L}\right) \right], \quad (3.20)$$

where

$$\sigma_i = \frac{\cosh \beta_i + \cos \beta_i}{\sinh \beta_i + \sin \beta_i} \quad (3.21)$$

$$1 + \cos \beta_i \cosh \beta_i = 0. \quad (3.22)$$

Additionally,  $W_i(0) = W_i'(0) = W_i''(L) = W_i'''(L) = 0$ .

Multiplying (3.15) and (3.16) by  $W_i$ , expanding the rightmost side, integrating over the length of the beam, and performing integration by parts yields

$$\begin{aligned}
& W_i(L) \left[ A_\psi \frac{\partial \psi}{\partial v'} + A_\theta \frac{\partial \theta}{\partial v'} \right]_{s=L} - \int_0^L W_i' \left( A_\psi \frac{\partial \psi}{\partial v'} + A_\theta \frac{\partial \theta}{\partial v'} \right) ds + \int_0^L W_i (\lambda v')' ds \\
&= \int_0^L W_i \left[ m\ddot{v} - me_\eta \left( \dot{\phi}^2 + \phi\ddot{\phi} + \ddot{\phi}v'w' + 2\dot{\phi}w'\dot{v}' + \dot{v}'^2 + 2\dot{\phi}v'\dot{w}' + 2\dot{\phi}\dot{v}'\dot{w}' \right) \right. \\
&\quad - me_\eta (v'\ddot{v}' + \phi w'\ddot{v}' + \phi v'\ddot{w}') + me_\zeta \left( \phi\dot{\phi}^2 - \ddot{\phi} + \frac{1}{2}\phi^2\ddot{\phi} + \frac{1}{2}\ddot{\phi}v'^2 + 2\dot{\phi}v'\dot{v}' \right) \\
&\quad \left. + me_\zeta (\phi\dot{v}'^2 - 2\dot{v}'\dot{w}' + \phi v'\ddot{v}' - w'\ddot{v}' - v'\ddot{w}') - Q_v \right] ds
\end{aligned} \tag{3.23}$$

and

$$\begin{aligned}
& W_i(L) \left[ A_\theta \frac{\partial \theta}{\partial w'} \right]_{s=L} - \int_0^L W_i' \left( A_\theta \frac{\partial \theta}{\partial w'} \right) ds + \int_0^L W_i (\lambda w')' ds \\
&= \int_0^L W_i \left[ m\ddot{w} - me_\eta \left( \phi\dot{\phi}^2 - \ddot{\phi} + \frac{1}{2}\phi^2\ddot{\phi} + \frac{1}{2}\ddot{\phi}w'^2 + 2\dot{\phi}w'\dot{w}' \right) \right. \\
&\quad \left. - me_\eta (\phi\dot{w}'^2 + \phi w'\ddot{w}') - me_\zeta \left( \dot{\phi}^2 + \phi\ddot{\phi} + \dot{w}'^2 + w'\ddot{w}' \right) - Q_w \right] ds.
\end{aligned} \tag{3.24}$$

### 3.1.6.2 Torsional Equation of Motion

The set of mode shapes (Bisplinghoff et al., 1996) used when applying the Galerkin method to the torsional equation of motion is

$$\Phi_i(s) = \sqrt{2} \sin \frac{\gamma_i s}{L}, \tag{3.25}$$

where

$$\gamma_i = \frac{(2i-1)\pi}{2}. \tag{3.26}$$

Furthermore,  $\Phi_i(0) = \Phi_i'(L) = 0$ .

Analogous to the bending equations, (3.17) is multiplied by  $\Phi_i$  and integrated over the length of the beam, providing

$$\int_0^L A_\phi \Phi_i ds = \int_0^L Q_\phi \Phi_i ds. \tag{3.27}$$

### 3.1.7 The Lagrange Multiplier

The terms of interest in (3.23) and (3.24) are  $\int_0^L W_i (\lambda v')' ds$  and  $\int_0^L W_i (\lambda w')' ds$ , which are obtained from (3.14). Letting  $A_u(s, t) = A_\psi \frac{\partial \psi}{\partial u'} + A_\theta \frac{\partial \theta}{\partial u'}$  and observing that  $u$  and the time and

space derivatives thereof are quadratic terms, a quadratic expression for  $A_u$  is obtained:

$$\begin{aligned} A_u(s, t) = & j_{\eta\zeta} (\ddot{v}'w' + v'\ddot{w}') - j_\zeta v'\ddot{v}' - j_\eta w'\ddot{w}' \\ & + D'_\zeta v'v'' + D'_\eta w'w'' + D_\zeta v'v''' + D_\eta w'w''' \\ & - D'_{\eta\zeta} (w'v'' + v'w'') - D_{\eta\zeta} (w'v''' + v'w'''). \end{aligned} \quad (3.28)$$

Equation (3.14) is integrated from the free end of the beam to  $s$ :

$$\begin{aligned} \int_L^s [A_u(\hat{s}, t) + \lambda(\hat{s}, t) (1 + u')] d\hat{s} = & \int_L^s \left[ m\ddot{u} + me_\eta (-\ddot{\phi}w' - 2\dot{\phi}\dot{w}' - \ddot{v}' - \phi\ddot{w}') \right. \\ & \left. + me_\zeta (\ddot{\phi}v' + 2\dot{\phi}\dot{v}' + \phi\ddot{v}' - \ddot{w}') - Q_u \right] d\hat{s} \end{aligned} \quad (3.29)$$

Since  $\lambda$  is quadratic,  $(1 + u')^{-1} \approx 1$ . Knowing this, that  $G_u(L, t) = 0$  (Crespo da Silva and Glynn, 1978b), and invoking the expression for  $u$  obtained in (3.19i), (3.29) simplifies to

$$\begin{aligned} \lambda(s, t) = & -A_u(s, t) + \int_L^s \left[ -m \int_0^{\hat{s}} (\dot{v}'^2 + v'\ddot{v}' + \dot{w}'^2 + w'\ddot{w}') d\tilde{s} \right. \\ & + me_\eta (-\ddot{\phi}w' - 2\dot{\phi}\dot{w}' - \ddot{v}' - \phi\ddot{w}') \\ & \left. + me_\zeta (\ddot{\phi}v' + 2\dot{\phi}\dot{v}' + \phi\ddot{v}' - \ddot{w}') - Q_u \right] d\hat{s}, \end{aligned} \quad (3.30)$$

and at  $L$ ,

$$\lambda(L, t) = [-j_{\eta\zeta} (\ddot{v}'w' + v'\ddot{w}') + j_\zeta v'\ddot{v}' + j_\eta w'\ddot{w}']_{s=L}. \quad (3.31)$$

With  $\lambda$  known,  $\int_0^L W_i (\lambda v')' ds$  and  $\int_0^L W_i (\lambda w')' ds$  are determinable. Beginning with integration by parts of the former,

$$\int_0^L W_i (\lambda v')' ds = - \int_0^L W_i' v' \lambda ds + W_i(L, t) \lambda(L, t) v'(L, t), \quad (3.32)$$

which is expanded as

$$\begin{aligned} \int_0^L W_i (\lambda v')' ds = & \int_0^L W_i' v' A_u(s, t) ds \\ & - \int_0^L W_i' v' \int_L^s \left\{ -m \int_0^{\hat{s}} (\dot{v}'^2 + v'\ddot{v}' + \dot{w}'^2 + w'\ddot{w}') d\tilde{s} \right. \\ & + me_\eta (-\ddot{\phi}w' - 2\dot{\phi}\dot{w}' - \ddot{v}' - \phi\ddot{w}') \\ & + me_\zeta (\ddot{\phi}v' + 2\dot{\phi}\dot{v}' + \phi\ddot{v}' - \ddot{w}') - Q_u \left. \right\} d\hat{s} ds \\ & + W_i(L, t) \lambda(L, t) v'(L, t). \end{aligned} \quad (3.33)$$

$A_u$  contains derivatives of the spatially dependent parameters, which are eliminated by further integrating by parts, ultimately yielding

$$\begin{aligned}
\int_0^L W_i (\lambda v')' ds = & - \int_0^L \left\{ D_\zeta \left( v' v''^2 W_i' + v'^2 v''' W_i' + v'^2 v'' W_i'' + v' v''^2 W_i' \right) \right. \\
& + D_\eta \left( v' w''^2 W_i' + v' w' w''' W_i' + v' w' w'' W_i'' + v'' w' w'' W_i' \right) \\
& - D_{\eta\zeta} \left( v'^2 w' W_i' + v' v''' w' W_i' + v' v'' w' W_i'' \right) \\
& \left. - D_{\eta\zeta} \left( 3v' v'' w'' W_i' + v'^2 w''' W_i' + v'^2 w'' W_i'' \right) \right\} ds \\
& + \int_0^L W_i' v' \left\{ j_{\eta\zeta} (\ddot{v}' w' + v' \ddot{w}') - j_\zeta v' \ddot{v}' - j_\eta w' \ddot{w}' \right. \\
& + D_\zeta v' v''' + D_\eta w' w''' - D_{\eta\zeta} (w' v''' + v' w''') \left. \right\} ds \\
& - \int_0^L W_i' v' \int_L^s \left\{ -m \int_0^{\hat{s}} (\dot{v}'^2 + v' \ddot{v}' + \dot{w}'^2 + w' \ddot{w}') d\tilde{s} \right. \\
& + m e_\eta (-\ddot{\phi} w' - 2\dot{\phi} \dot{w}' - \ddot{v}' - \phi \ddot{w}') \\
& + m e_\zeta (\ddot{\phi} v' + 2\dot{\phi} \dot{v}' + \phi \ddot{v}' - \ddot{w}') - Q_u \left. \right\} d\hat{s} ds \\
& + W_i \left[ -j_{\eta\zeta} (v' \ddot{v}' w' + v'^2 \ddot{w}') + j_\zeta v'^2 \ddot{v}' + j_\eta v' w' \ddot{w}' \right]_{s=L}
\end{aligned} \tag{3.34}$$

and similarly

$$\begin{aligned}
\int_0^L W_i (\lambda w')' ds = & - \int_0^L \left\{ D_\zeta \left( w' v''^2 W_i' + w' v' v''' W_i' + w' v' v'' W_i'' + v' v'' w'' W_i' \right) \right. \\
& + D_\eta \left( w' w''^2 W_i' + w'^2 w''' W_i' + w'^2 w'' W_i'' + w' w''^2 W_i' \right) \\
& - D_{\eta\zeta} \left( v' w''^2 W_i' + v' w' w''' W_i' + v' w' w'' W_i'' \right) \\
& \left. - D_{\eta\zeta} \left( 3v'' w' w'' W_i' + v''' w'^2 W_i' + w'^2 v'' W_i'' \right) \right\} ds \\
& + \int_0^L W_i' w' \left\{ j_{\eta\zeta} (\ddot{v}' w' + v' \ddot{w}') - j_\zeta v' \ddot{v}' - j_\eta w' \ddot{w}' \right. \\
& + D_\zeta v' v''' + D_\eta w' w''' - D_{\eta\zeta} (w' v''' + v' w''') \left. \right\} ds \\
& - \int_0^L W_i' w' \int_L^s \left\{ -m \int_0^{\hat{s}} (\dot{v}'^2 + v' \ddot{v}' + \dot{w}'^2 + w' \ddot{w}') d\tilde{s} \right. \\
& + m e_\eta (-\ddot{\phi} w' - 2\dot{\phi} \dot{w}' - \ddot{v}' - \phi \ddot{w}') \\
& + m e_\zeta (\ddot{\phi} v' + 2\dot{\phi} \dot{v}' + \phi \ddot{v}' - \ddot{w}') - Q_u \left. \right\} d\hat{s} ds \\
& + W_i \left[ -j_{\eta\zeta} (\ddot{v}' w'^2 + v' w' \ddot{w}') + j_\zeta v' \ddot{v}' w' + j_\eta w'^2 \ddot{w}' \right]_{s=L}.
\end{aligned} \tag{3.35}$$



### 3.1.8 The Equations of Motion

At this point, everything can be determined. Remaining terms containing derivatives of the spatially dependent parameters are integrated by parts to distribute the derivative into the co-factors.

Consequently, the equation of motion in the  $y$ -direction for each  $i$  is

$$\begin{aligned}
& W_i(L) \left[ (me_\eta - me_\zeta \phi) \int_0^s (\dot{v}'^2 + v' \ddot{v}' + \dot{w}'^2 + w' \ddot{w}') d\hat{s} + me_\eta (-\ddot{v}v' - \phi \ddot{v}w') \right. \\
& + me_\zeta (\phi \ddot{v}v' - \ddot{v}w') + j_\xi (\ddot{\phi}w' + \dot{\phi}\dot{w}' + 2w'\dot{v}'\dot{w}' + w'^2\ddot{v}') + j_\eta (-\dot{\phi}\dot{w}' + \phi^2\ddot{v}') \\
& + j_\eta (-\phi\ddot{w}' + 2\phi\dot{\phi}\dot{v}') + j_\zeta (-2\phi\dot{\phi}\dot{v}' + v'\dot{v}'^2 + \dot{\phi}\dot{w}' + v'\dot{w}'^2 + \ddot{v}' - \phi^2\ddot{v}') \\
& + j_\zeta (v'^2\ddot{v}' + \phi\ddot{w}' + v'w'\ddot{w}') + j_{\eta\zeta} (2\dot{\phi}\dot{v}' + 4\phi\dot{\phi}\dot{w}' + 2\phi\ddot{v}' - \ddot{w}' + 2\phi^2\ddot{w}') \\
& \quad \left. - \frac{1}{2}j_{\eta\zeta} (v'^2\ddot{w}' + w'^2\ddot{w}') - D_\xi w'\phi'' \right]_{s=L} \\
& - \int_0^L \left\{ W_i' \left[ (me_\eta - me_\zeta \phi) \int_0^s (\dot{v}'^2 + v' \ddot{v}' + \dot{w}'^2 + w' \ddot{w}') d\hat{s} \right. \right. \\
& + me_\eta (-\ddot{v}v' - \phi \ddot{v}w') + me_\zeta (\phi \ddot{v}v' - \ddot{v}w') + j_\xi (\ddot{\phi}w' + \dot{\phi}\dot{w}' + 2w'\dot{v}'\dot{w}' + w'^2\ddot{v}') \\
& + j_\eta (-\dot{\phi}\dot{w}' + \phi^2\ddot{v}' - \phi\ddot{w}' + 2\phi\dot{\phi}\dot{v}') + j_\zeta (-2\phi\dot{\phi}\dot{v}' + v'\dot{v}'^2 + \dot{\phi}\dot{w}' + v'\dot{w}'^2 + \ddot{v}') \\
& + j_\zeta (-\phi^2\ddot{v}' + v'^2\ddot{v}' + \phi\ddot{w}' + v'w'\ddot{w}') + j_{\eta\zeta} (2\dot{\phi}\dot{v}' + 4\phi\dot{\phi}\dot{w}' + 2\phi\ddot{v}' - \ddot{w}') \\
& \quad + j_{\eta\zeta} \left( 2\phi^2\ddot{w}' - \frac{1}{2}v'^2\ddot{w}' - \frac{1}{2}w'^2\ddot{w}' \right) + D_\zeta (v'v''^2 + v''w'w'') \\
& + D_{\eta\zeta} (-v'v''w'' + w'w''^2) + v' \int_L^{\hat{s}} -m \int_0^{\hat{s}} (\dot{v}'^2 + v' \ddot{v}' + \dot{w}'^2 + w' \ddot{w}') d\hat{s} \\
& + me_\eta (-\ddot{\phi}w' - 2\dot{\phi}\dot{w}' - \ddot{v}' - \phi\ddot{w}') + me_\zeta (\ddot{\phi}v' + 2\dot{\phi}\dot{v}' + \phi\ddot{v}' - \ddot{w}') - Q_u d\hat{s} \Big] \\
& + W_i'' \left[ D_\xi (\phi'w' + w'^2v'') + D_\eta (\phi^2v'' - \phi w'') + D_\zeta (v'' - \phi^2v'' + v'^2v'') \right. \\
& + D_\zeta (\phi w'' + v'w'w'') + D_{\eta\zeta} \left( 2\phi v'' - w'' + 2\phi^2w'' - \frac{1}{2}v'^2w'' - \frac{1}{2}w'^2w'' \right) \Big] \Big\} ds \\
& = \int_0^L W_i \left( m\ddot{v} - me_\eta (\dot{\phi}^2 + \phi\ddot{\phi} + \ddot{\phi}v'w' + 2\dot{\phi}w'\dot{v}' + \dot{v}'^2 + 2\dot{\phi}v'\dot{w}' + 2\phi\ddot{v}'\dot{w}') \right. \\
& \quad - me_\eta (+v'\ddot{v}' + \phi w'\ddot{v}' + \phi v'\ddot{w}') + me_\zeta \left( \phi\dot{\phi}^2 - \ddot{\phi} + \frac{1}{2}\phi^2\ddot{\phi} + \frac{1}{2}\ddot{\phi}v'^2 \right) \\
& \quad \left. + me_\zeta (2\dot{\phi}v'\dot{v}' + \phi\dot{v}'^2 - 2\dot{v}'\dot{w}' + \phi v'\ddot{v}' - w'\ddot{v}' - v'\ddot{w}') - Q_v \right) ds. \tag{3.36}
\end{aligned}$$

Additionally, the equation of motion in the  $z$ -direction is

$$\begin{aligned}
W_i(L) & \left[ (me_\eta\phi + me_\zeta) \int_0^s (\dot{v}'^2 + v'\ddot{v}' + \dot{w}'^2 + w'\ddot{w}') d\hat{s} - me_\eta (\phi\ddot{v}' + \phi\ddot{w}') \right. \\
& + me_\zeta (-\ddot{v}v' - \ddot{w}w') - j_\xi (\dot{\phi}\dot{v}' + w'\dot{v}'^2) + j_\eta (-\dot{\phi}\dot{v}' - 2\phi\dot{\phi}\dot{w}' - \phi\ddot{v}' + \ddot{w}') \\
& + j_\eta (-\phi^2\ddot{w}' + w'\dot{w}'^2 + w'^2\ddot{w}') + j_\zeta (\dot{\phi}\dot{v}' + w'\dot{v}'^2 + 2\phi\dot{\phi}\dot{w}' + \phi\ddot{v}' + \phi^2\ddot{w}') \\
& + j_\zeta v'w'\ddot{v}' - j_{\eta\zeta} (-4\phi\dot{\phi}\dot{v}' + v'\dot{v}'^2 + 2\dot{\phi}\dot{w}' + 2w'\dot{v}'\dot{w}' + v'\dot{w}'^2 + \ddot{v}' - 2\phi^2\ddot{v}') \\
& \quad \left. - j_{\eta\zeta} \left( \frac{1}{2}v'^2\ddot{v}' + \frac{1}{2}w'^2\ddot{v}' + 2\phi\ddot{w}' + 2v'w'\ddot{w}' \right) \right]_{s=L} \\
& - \int_0^L \left\{ W_i' \left[ (me_\eta\phi + me_\zeta) \int_0^s (\dot{v}'^2 + v'\ddot{v}' + \dot{w}'^2 + w'\ddot{w}') d\hat{s} \right. \right. \\
& - me_\eta (\phi\ddot{v}' + \phi\ddot{w}') + me_\zeta (-\ddot{v}v' - \ddot{w}w') - j_\xi (\dot{\phi}\dot{v}' + w'\dot{v}'^2) - j_\eta \dot{\phi}\dot{v}' \\
& + j_\eta (-2\phi\dot{\phi}\dot{w}' - \phi\ddot{v}' + \ddot{w}' - \phi^2\ddot{w}' + w'\dot{w}'^2 + w'^2\ddot{w}') + j_\zeta (\dot{\phi}\dot{v}' + w'\dot{v}'^2) \\
& + j_\zeta (2\phi\dot{\phi}\dot{w}' + \phi\ddot{v}' + \phi^2\ddot{w}' + v'\ddot{v}'w') - j_{\eta\zeta} (-4\phi\dot{\phi}\dot{v}' + v'\dot{v}'^2 + 2\dot{\phi}\dot{w}') \\
& - j_{\eta\zeta} (2w'\dot{v}'\dot{w}' + v'\dot{w}'^2 + \ddot{v}' - 2\phi^2\ddot{v}' + \frac{1}{2}v'^2\ddot{v}' + \frac{1}{2}w'^2\ddot{v}' + 2\phi\ddot{w}' + 2v'w'\ddot{w}') \\
& + D_\xi (\phi'v'' + w'v''^2) + D_\eta w'w''^2 + D_\zeta v'v''w'' - D_{\eta\zeta} (v''w'w'' + v'w''^2) \\
& + w' \int_L^s -m \int_0^{\hat{s}} (\dot{v}'^2 + v'\ddot{v}' + \dot{w}'^2 + w'\ddot{w}') d\tilde{s} - me_\eta \ddot{\phi}w' \\
& + me_\eta (-2\dot{\phi}\dot{w}' - \ddot{v}' - \phi\ddot{w}') + me_\zeta (\ddot{\phi}v' + 2\dot{\phi}\dot{v}' + \phi\ddot{v}' - \ddot{w}') - Q_u d\hat{s} \Big] \\
& + W_i'' \left[ D_\eta (-\phi v'' + w'' - \phi^2 w'' + w'^2 w'') + D_\zeta (\phi v'' + \phi^2 w'' + v'v''w') \right. \\
& \quad \left. + D_{\eta\zeta} \left( -v'' + 2\phi^2 v'' - \frac{1}{2}v'^2 v'' - \frac{1}{2}w'^2 v'' - 2\phi w'' - 2v'w'w'' \right) \right] \Big\} ds \\
& = \int_0^L W_i \left( m\ddot{w} - me_\eta \left( \phi\dot{\phi}^2 - \ddot{\phi} + \frac{1}{2}\phi^2\ddot{\phi} + \frac{1}{2}\ddot{\phi}w'^2 + 2\dot{\phi}w'\dot{w}' \right) \right. \\
& \quad \left. - me_\eta (\phi\dot{w}'^2 + \phi w'\ddot{w}') - me_\zeta (\dot{\phi}^2 + \phi\ddot{\phi} + \dot{w}'^2 + w'\ddot{w}') - Q_w \right) ds. \tag{3.37}
\end{aligned}$$

Finally, the torsional equation of motion is

$$\begin{aligned}
& \int_0^L \left\{ \Phi_i \left[ (me_\eta w' - me_\zeta v') \int_0^s (\dot{v}'^2 + v' \ddot{v}' + \dot{w}'^2 + w' \ddot{w}') d\hat{s} \right. \right. \\
& \quad + me_\eta \left( -\phi \ddot{v} + \ddot{w} - \frac{1}{2} \phi^2 \ddot{w} - \ddot{v} v' w' - \frac{1}{2} \ddot{w} w'^2 \right) \\
& \quad + me_\zeta \left( -\ddot{v} + \frac{1}{2} \phi^2 \ddot{v} - \phi \ddot{w} + \frac{1}{2} \ddot{v} v'^2 \right) \\
& \quad + j_\xi (\ddot{\phi} + \dot{v}' \dot{w}' + w' \ddot{v}') + j_\eta (-\phi \dot{v}'^2 + \dot{v}' \dot{w}' + \phi \dot{w}'^2) \\
& \quad + j_\zeta (\phi \dot{v}'^2 - \phi \dot{w}'^2 - \dot{v}' \dot{w}') - j_{\eta\zeta} (\dot{v}'^2 - \dot{w}'^2 + 4\phi \dot{v}' \dot{w}') \\
& \quad + D_\eta (\phi v''^2 - v'' w'' - \phi w''^2) + D_\zeta (-\phi v''^2 + v'' w'' + \phi w''^2) \\
& \quad \left. + D_{\eta\zeta} (v''^2 + 4\phi v'' w'' - w''^2) \right] + \Phi'_i D_\xi (\phi' + v'' w') \Big\} ds = \int_0^L Q_\phi \Phi_i ds. \tag{3.38}
\end{aligned}$$

The effects of including all the cubic non-linear terms was assessed on the Heavy Goland wing. The parameters of the Heavy Goland wing, which include airfoil shape, mass properties and wing stiffness are presented in (Eastep and Olsen, 1980) and will not be repeated in here.

An analysis of the Heavy Goland wing using a nonlinear structural model and a simple aerodynamics approach was presented in (Strganac et al., 2005). The same nonlinear structural model was later coupled with a RANS model (Cizmas et al., 2007). The structural model included the mechanics of both the traditional out-of-plane and torsional components plus an additional in-plane mode of motion. This additional mode and the presence of nonlinear effects led to remarkable nonlinear dynamic interactions (Cizmas et al., 2007). In both cases, the structural model did not include all the cubic nonlinear terms.

The results shown in Figs. 3.2-3.3 highlight the effect of the cubic nonlinear terms of the structural model and underscore the importance of the nonlinear effects in aeroelastic simulations. Figure 3.2 shows that missing some of the cubic terms did not affect the LCO prediction. Figure-3.3, however, shows that the numerical simulation using all cubic nonlinearities predicted flutter, while the case that was missing some of the cubic nonlinear terms did not. Consequently, in the flutter case, it was important to keep all the cubic terms.

## 3.2 Modal Representation

### 3.2.1 Introduction

The equations of motion (3.36)-(3.38) are nonlinear, coupled partial differential equations in time and space. As mentioned previously, the boundary conditions are known. Therefore, it is possible to represent the deformations as an infinite sum of the product of spatially dependent, orthogonal mode shapes and time-dependent coefficients. Taking the mode shapes invoked in the Galerkin method, the displacements can be expressed as follows:

$$w = \sum_{i=1}^l w_i(t) W_i(s) \quad v = \sum_{i=1}^m v_i(t) W_i(s) \quad \phi = \sum_{i=1}^n \phi_i(t) \Phi_i(s). \tag{3.39}$$

Upon invoking these mode shapes, the partial differential equations reduce to a system of ordinary differential equations in time, for which the time coefficients are the unknown quantities.

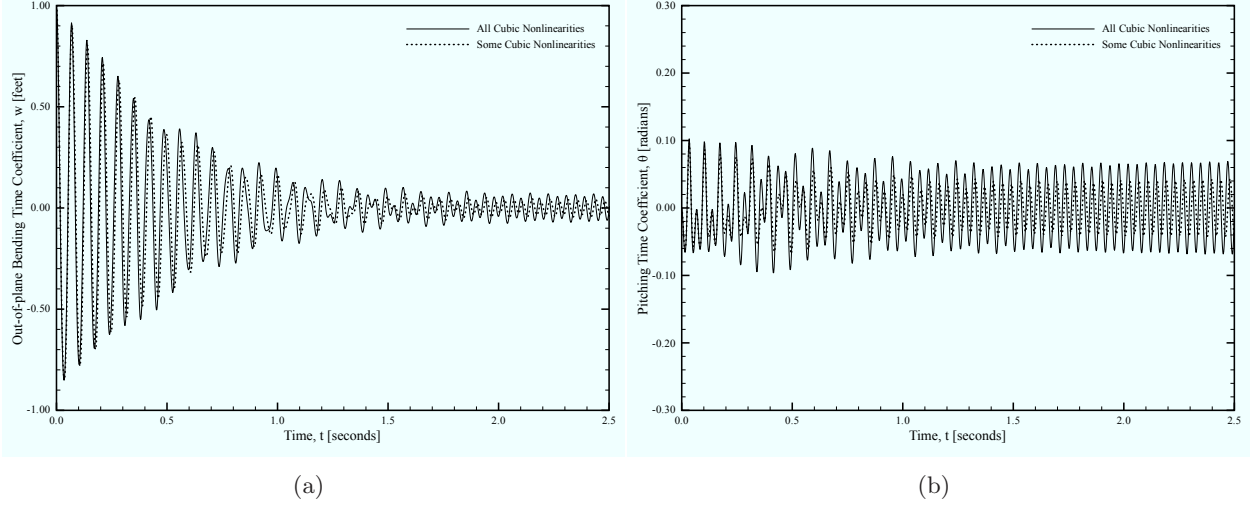


Figure 3.2: Heavy Goland Wing time coefficients at LCO: (a) out-of-plane bending, and (b) pitching.

Therefore, the equations of motion are written in the following manner using linear and non-linear arrays:

$$[M_L + M_{NL}] \begin{Bmatrix} \ddot{\mathbf{w}} \\ \ddot{\mathbf{v}} \\ \ddot{\phi} \end{Bmatrix} + [C_L + C_{NL}] \begin{Bmatrix} \dot{\mathbf{w}} \\ \dot{\mathbf{v}} \\ \dot{\phi} \end{Bmatrix} + [K_L + K_{NL}] \begin{Bmatrix} \mathbf{w} \\ \mathbf{v} \\ \phi \end{Bmatrix} = \mathbf{F}_L + \mathbf{F}_{NL}, \quad (3.40)$$

where  $\mathbf{w}$ ,  $\mathbf{v}$ , and  $\phi$  each represent vectors containing the time coefficients:  $\{w_1, \dots, w_l\}^T$ ,  $\{v_1, \dots, v_m\}^T$ , and  $\{\phi_1, \dots, \phi_n\}^T$ .

Each of the matrices is  $(l + m + n) \times (l + m + n)$  and can be expressed as the concatenation of 9 submatrices with the following dimensions:

$$\begin{bmatrix} [l \times l] & [l \times m] & [l \times n] \\ [m \times l] & [m \times m] & [m \times n] \\ [n \times l] & [n \times m] & [n \times n] \end{bmatrix}. \quad (3.41)$$

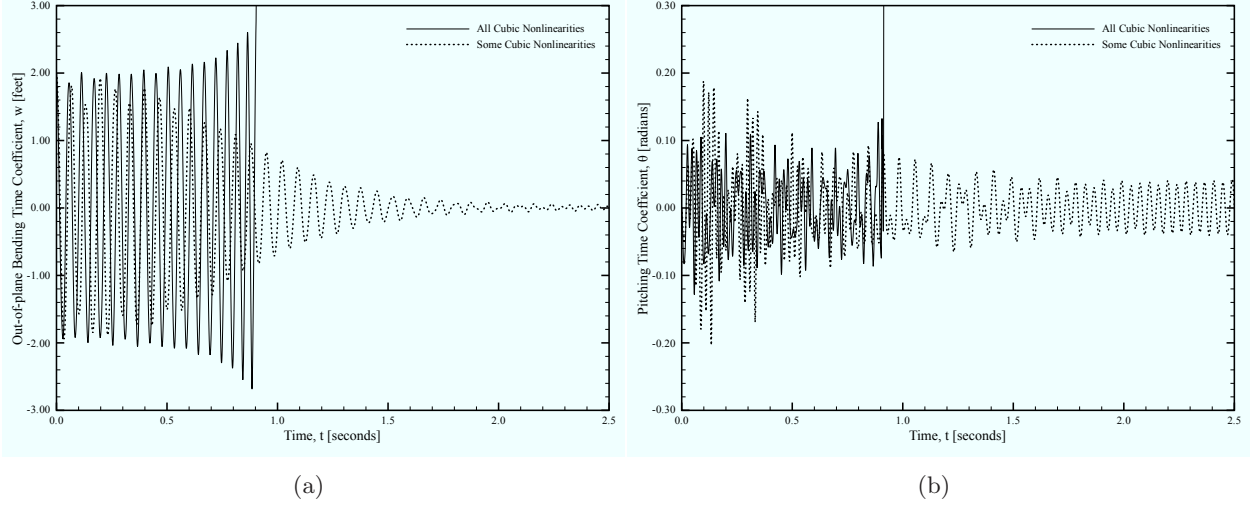


Figure 3.3: Heavy Goland Wing time coefficients at flutter: (a) out-of-plane bending, and (b) pitching.

### 3.2.2 Linear Matrices

#### 3.2.2.1 Linear Mass Matrix

The linear mass matrix is defined as follows:

$$\begin{aligned}
 [M_L]_{i,j} &= \int_0^L (W_i m W_j + W'_i j_\eta W'_j) ds - [W_i j_\eta W'_j]_{s=L} \\
 [M_L]_{i,l+j} &= - \int_0^L W'_i j_\eta \zeta W'_j ds + [W_i j_\eta \zeta W'_j]_{s=L} \\
 [M_L]_{i,l+m+j} &= \int_0^L W_i m e_\eta \Phi_j ds \\
 [M_L]_{l+i,j} &= - \int_0^L W'_i j_\eta \zeta W'_j ds + [W_i j_\eta \zeta W'_j]_{s=L} \\
 [M_L]_{l+i,l+j} &= \int_0^L (W_i m W_j + W'_i j_\zeta W'_j) ds - [W_i j_\zeta W'_j]_{s=L} \\
 [M_L]_{l+i,l+m+j} &= - \int_0^L W_i m e_\zeta \Phi_j ds \\
 [M_L]_{l+m+i,j} &= \int_0^L \Phi_i m e_\eta W_j ds \\
 [M_L]_{l+m+i,l+j} &= - \int_0^L \Phi_i m e_\zeta W_j ds \\
 [M_L]_{l+m+i,l+m+j} &= \int_0^L \Phi_i j_\xi \Phi_j ds.
 \end{aligned} \tag{3.42}$$

### 3.2.2.2 Linear Damping Matrix

In the equations of motion, there are no linear occurrences of the first time derivative of any of the deformations. Therefore, the linear damping matrix is zero:

$$[C_L] = 0. \quad (3.43)$$

### 3.2.2.3 Linear Stiffness Matrix

The nonzero submatrices of the linear stiffness matrix are

$$\begin{aligned} [K_L]_{i,j} &= \int_0^L W_i'' D_\eta W_j'' ds \\ [K_L]_{i,l+j} &= - \int_0^L W_i'' D_{\eta\zeta} W_j'' ds \\ [K_L]_{l+i,j} &= - \int_0^L W_i'' D_{\eta\zeta} W_j'' ds \\ [K_L]_{l+i,l+j} &= \int_0^L W_i'' D_\zeta W_j'' ds \\ [K_L]_{l+m+i,l+m+j} &= \int_0^L \Phi_i' D_\xi \Phi_j' ds. \end{aligned} \quad (3.44)$$

### 3.2.3 Nonlinear Matrices

In determining the nonlinear matrices, there are several possibilities concerning where to assign terms from the equations of motion. This decision is done systematically such that terms containing second-order time derivatives are assigned to the mass matrix, remaining terms that contain first-order time derivatives are assigned to the damping matrix, and terms containing no time derivatives are assigned to the stiffness matrix. Furthermore, for terms containing factors that have the same-order time derivative, placement within the matrix is done such that the term with the lowest-order spatial derivative is the unknown. Finally, for instances in which the temporal and spatial derivatives of the factors are both of the same order, the spatial derivative of  $v$  is taken to be the unknown.

### 3.2.3.1 Nonlinear Mass Matrix

The nonlinear mass matrix is

$$\begin{aligned}
[M_{NL}]_{i,j} = & \int_0^L \left\{ W'_i (me_\eta \phi + me_\zeta) \int_0^s w' W'_j d\hat{s} + W'_i [-me_\eta \phi w' - me_\zeta w'] W_j \right. \\
& + W'_i w' \int_L^s (-me_\eta \phi - me_\zeta) W'_j d\hat{s} \\
& + W'_i \left( -2j_{\eta\zeta} \phi - 2j_{\eta\zeta} v' w' - j_\eta \phi^2 + j_\eta w'^2 + j_\zeta \phi^2 \right) W'_j \\
& - W'_i w' \int_L^s m \int_0^{\hat{s}} w' W'_j d\tilde{s} d\hat{s} + W_i [-me_\eta \phi w' - me_\zeta w'] W'_j \Big\} ds \\
& - \left[ W_i (me_\eta \phi + me_\zeta) \int_0^s w' W'_j d\hat{s} + W_i [-me_\eta \phi w' - me_\zeta w'] W_j \right. \\
& \left. + W_i \left( -2j_{\eta\zeta} \phi - 2j_{\eta\zeta} v' w' + j_\eta w'^2 - j_\eta \phi^2 + j_\zeta \phi^2 \right) W'_j \right]_{s=L} \\
\\
[M_{NL}]_{i,l+j} = & \int_0^L \left\{ W'_i (me_\eta \phi + me_\zeta) \int_0^s v' W'_j d\hat{s} + W'_i [-me_\eta \phi v' - me_\zeta v'] W_j \right. \\
& + W'_i w' \int_L^s (-me_\eta + me_\zeta \phi) W'_j d\hat{s} \\
& + W'_i \left( 2j_{\eta\zeta} \phi^2 - \frac{1}{2} j_{\eta\zeta} v'^2 - \frac{1}{2} j_{\eta\zeta} w'^2 - j_\eta \phi + j_\zeta \phi + j_\zeta v' w' \right) W'_j \\
& - W'_i w' \int_L^s m \int_0^{\hat{s}} v' W'_j d\tilde{s} d\hat{s} \Big\} ds \\
& - \left[ W_i (me_\eta \phi + me_\zeta) \int_0^s v' W'_j d\hat{s} + W_i [-me_\eta \phi v' - me_\zeta v'] W_j \right. \\
& \left. + W_i \left( 2j_{\eta\zeta} \phi^2 - \frac{1}{2} j_{\eta\zeta} v'^2 - \frac{1}{2} j_{\eta\zeta} w'^2 - j_\eta \phi + j_\zeta \phi + j_\zeta v' w' \right) W'_j \right]_{s=L} \\
\\
[M_{NL}]_{i,l+m+j} = & \int_0^L \left\{ W'_i w' \int_L^s (-me_\eta w' + me_\zeta v') \Phi_j d\hat{s} \right. \\
& \left. + W_i \left[ -me_\eta \left( \frac{1}{2} \phi^2 + \frac{1}{2} w'^2 \right) - me_\zeta \phi \right] \Phi_j \right\} ds
\end{aligned}$$

$$\begin{aligned}
[M_{NL}]_{l+i,j} = & \int_0^L \left\{ W'_i (me_\eta - me_\zeta \phi) \int_0^s w' W'_j d\hat{s} \right. \\
& + W'_i v' \int_L^s (-me_\eta \phi - me_\zeta) W'_j d\hat{s} \\
& + W_i [-me_\eta \phi v' - me_\zeta v'] W'_j - W'_i v' \int_L^s m \int_0^{\hat{s}} w' W'_j d\tilde{s} d\hat{s} \\
& + W'_i \left( 2j_{\eta\zeta} \phi^2 - \frac{1}{2} j_{\eta\zeta} v'^2 - \frac{1}{2} j_{\eta\zeta} w'^2 - j_\eta \phi + j_\zeta \phi + j_\zeta v' w' \right) W'_j \Big\} ds \\
& - \left[ W_i (me_\eta - me_\zeta \phi) \int_0^s w' W'_j d\hat{s} + W_i [-me_\eta \phi v' - me_\zeta v'] W'_j \right. \\
& \left. + W_i \left( 2j_{\eta\zeta} \phi^2 - \frac{1}{2} j_{\eta\zeta} v'^2 - \frac{1}{2} j_{\eta\zeta} w'^2 - j_\eta \phi + j_\zeta \phi + j_\zeta v' w' \right) W'_j \right]_{s=L}
\end{aligned}$$

$$\begin{aligned}
[M_{NL}]_{l+i,l+j} = & \int_0^L \left\{ W'_i (me_\eta - me_\zeta \phi) \int_0^s v' W'_j d\hat{s} \right. \\
& + W'_i [-me_\eta (v' + \phi w') + me_\zeta (\phi v' - w')] W'_j \\
& + W'_i v' \int_L^s (-me_\eta + me_\zeta \phi) W'_j d\hat{s} \\
& + W_i [-me_\eta (v' + \phi w') + me_\zeta (\phi v' - w')] W'_j \\
& + W'_i \left( 2j_{\eta\zeta} \phi + j_\xi w'^2 + j_\eta \phi^2 - j_\zeta \phi^2 + j_\zeta v'^2 \right) W'_j \\
& - W'_i v' \int_L^s m \int_0^{\hat{s}} v' W'_j d\tilde{s} d\hat{s} \Big\} ds - \left[ W_i (me_\eta - me_\zeta \phi) \int_0^s v' W'_j d\hat{s} \right. \\
& + W_i [-me_\eta (v' + \phi w') + me_\zeta (\phi v' - w')] W'_j \\
& \left. + W_i \left( 2j_{\eta\zeta} \phi + j_\xi w'^2 + j_\eta \phi^2 - j_\zeta \phi^2 + j_\zeta v'^2 \right) W'_j \right]_{s=L}
\end{aligned}$$

$$\begin{aligned}
[M_{NL}]_{l+i,l+m+j} = & \int_0^L \left\{ W'_i v' \int_L^s (-me_\eta w' + me_\zeta v') \Phi_j d\hat{s} + W'_i j_\xi w' \Phi_j \right. \\
& + W_i \left[ -me_\eta (\phi + v' w') + me_\zeta \left( \frac{1}{2} \phi^2 + \frac{1}{2} v'^2 \right) \right] \Phi_j \Big\} ds \\
& - [W_i j_\xi w' \Phi_j]_{s=L}
\end{aligned}$$

$$\begin{aligned}
[M_{NL}]_{l+m+i,j} = & \int_0^L \Phi_i \left\{ (me_\eta w' - me_\zeta v') \int_0^s w' W'_j d\hat{s} \right. \\
& + \left[ -me_\eta \left( \frac{1}{2} \phi^2 + \frac{1}{2} w'^2 \right) - me_\zeta \phi \right] W'_j \Big\} ds
\end{aligned}$$

$$\begin{aligned}
[M_{NL}]_{l+m+i,l+j} = & \int_0^L \Phi_i \left\{ (me_\eta w' - me_\zeta v') \int_0^s v' W'_j d\hat{s} + j_\xi w' W'_j \right. \\
& + \left[ -me_\eta (\phi + v' w') + me_\zeta \left( \frac{1}{2} \phi^2 + \frac{1}{2} v'^2 \right) \right] W'_j \Big\} ds. \tag{3.45}
\end{aligned}$$



### 3.2.3.2 Nonlinear Damping Matrix

The nonlinear damping matrix is

$$\begin{aligned}
[C_{NL}]_{i,j} &= \int_0^L \left\{ W'_i (me_\eta \phi + me_\zeta) \int_0^s \dot{w}' W'_j d\hat{s} + W_i (-me_\eta \phi \dot{w}' - me_\zeta \dot{w}') W'_j \right. \\
&\quad \left. + W'_i (-j_{\eta\zeta} v' \dot{w}' + j_\eta w' \dot{w}') W'_j - W'_i w' \int_L^s m \int_0^{\hat{s}} \dot{w}' W'_j d\tilde{s} d\hat{s} \right\} ds \\
&\quad - \left[ W_i (me_\eta \phi + me_\zeta) \int_0^s \dot{w}' W'_j d\hat{s} + W_i (-j_{\eta\zeta} v' \dot{w}' + j_\eta w' \dot{w}') W'_j \right]_{s=L} \\
[C_{NL}]_{i,l+j} &= \int_0^L \left\{ W'_i (me_\eta \phi + me_\zeta) \int_0^s \dot{v}' W'_j d\hat{s} \right. \\
&\quad \left. + W'_i (-j_{\eta\zeta} v' \dot{v}' - 2j_{\eta\zeta} w' \dot{w}' - j_\xi w' \dot{v}' + j_\zeta \dot{v}' w') W'_j \right. \\
&\quad \left. - W'_i w' \int_L^s m \int_0^{\hat{s}} \dot{v}' W'_j d\tilde{s} d\hat{s} \right\} ds \\
&\quad - \left[ W_i (me_\eta \phi + me_\zeta) \int_0^s \dot{v}' W'_j d\hat{s} \right. \\
&\quad \left. + W_i (-j_{\eta\zeta} v' \dot{v}' - 2j_{\eta\zeta} w' \dot{w}' - j_\xi w' \dot{v}' + j_\zeta \dot{v}' w') W'_j \right]_{s=L} \\
[C_{NL}]_{i,l+m+j} &= \int_0^L \left\{ W'_i w' \int_L^s (-2me_\eta \dot{w}' + 2me_\zeta \dot{v}') \Phi_j d\hat{s} \right. \\
&\quad \left. + W_i \left[ -me_\eta (\phi \dot{\phi} + 2w' \dot{w}') - me_\zeta \dot{\phi} \right] \Phi_j + W'_i (4j_{\eta\zeta} \phi \dot{v}' - 2j_{\eta\zeta} \dot{w}') \Phi_j \right. \\
&\quad \left. + W'_i (-j_\xi \dot{v}' - j_\eta \dot{v}' - 2j_\eta \phi \dot{w}' + j_\zeta \dot{v}' + 2j_\zeta \phi \dot{w}') \Phi_j \right\} ds \\
&\quad - \left[ W_i (4j_{\eta\zeta} \phi \dot{v}' - 2j_{\eta\zeta} \dot{w}' - j_\xi \dot{v}' - j_\eta \dot{v}' - 2j_\eta \phi \dot{w}' + j_\zeta \dot{v}') \Phi_j \right]_{s=L} \\
&\quad - 2 \left[ W_i j_\zeta \phi \dot{w}' \Phi_j \right]_{s=L} \\
[C_{NL}]_{l+i,j} &= \int_0^L \left\{ W'_i (me_\eta - me_\zeta \phi) \int_0^s \dot{w}' W'_j d\hat{s} + W'_i j_\zeta v' \dot{w}' W'_j \right. \\
&\quad \left. - W'_i v' \int_L^s m \int_0^{\hat{s}} \dot{w}' W'_j d\tilde{s} d\hat{s} \right\} ds \\
&\quad - \left[ W_i (me_\eta - me_\zeta \phi) \int_0^s \dot{w}' W'_j d\hat{s} + W_i j_\zeta v' \dot{w}' W'_j \right]_{s=L}
\end{aligned}$$

$$\begin{aligned}
[C_{NL}]_{l+i,l+j} &= \int_0^L \left\{ W'_i (me_\eta - me_\zeta \phi) \int_0^s \dot{v}' W'_j d\hat{s} \right. \\
&\quad + W_i [-me_\eta (\dot{v}' + 2\phi \dot{w}') + me_\zeta (\phi \dot{v}' - 2\dot{w}')] W'_j \\
&\quad + W'_i (2j_\xi w' \dot{w}' + j_\zeta v' \dot{v}') W'_j - W'_i v' \int_L^s m \int_0^{\hat{s}} \dot{v}' W'_j d\tilde{s} d\hat{s} \Big\} ds \\
&\quad - \left[ W_i (me_\eta - me_\zeta \phi) \int_0^s \dot{v}' W'_j d\hat{s} + W_i (2j_\xi w' \dot{w}' + j_\zeta v' \dot{v}') W'_j \right]_{s=L} \\
[C_{NL}]_{l+i,l+m+j} &= \int_0^L \left\{ W'_i v' \int_L^s (-2me_\eta \dot{w}' + 2me_\zeta \dot{v}') \Phi_j d\hat{s} \right. \\
&\quad + W_i [-me_\eta (\dot{\phi} + 2w' \dot{v}' + 2v' \dot{w}') + me_\zeta (\phi \dot{\phi} + 2v' \dot{v}')] \Phi_j \\
&\quad + W'_i (2j_{\eta\zeta} \dot{v}' + 4j_{\eta\zeta} \phi \dot{w}' + j_\xi \dot{w}' - j_\eta \dot{w}' + 2j_\eta \phi \dot{v}' + j_\zeta \dot{w}') \Phi_j \\
&\quad - 2W'_i j_\zeta \phi \dot{v}' \Phi_j \Big\} ds - [W_i (2j_{\eta\zeta} \dot{v}' + 4j_{\eta\zeta} \phi \dot{w}' + j_\xi \dot{w}' - j_\eta \dot{w}') \Phi_j]_{s=L} \\
&\quad - [W_i (2j_\eta \phi \dot{v}' + j_\zeta \dot{w}' - 2j_\zeta \phi \dot{v}') \Phi_j]_{s=L} \\
[C_{NL}]_{l+m+i,j} &= \int_0^L \left\{ \Phi_i (me_\eta w' - me_\zeta v') \int_0^s \dot{w}' W'_j d\hat{s} \right. \\
&\quad + \Phi_i (j_{\eta\zeta} \dot{w}' + j_\eta \phi \dot{w}' - j_\zeta \phi \dot{w}') W'_j \Big\} ds \\
[C_{NL}]_{l+m+i,l+j} &= \int_0^L \left\{ \Phi_i (me_\eta w' - me_\zeta v') \int_0^s \dot{v}' W'_j d\hat{s} + \Phi_i (-j_{\eta\zeta} \dot{v}' - 4j_{\eta\zeta} \phi \dot{w}') W'_j \right. \\
&\quad + \Phi_i (j_\xi \dot{w}' - j_\eta \phi \dot{v}' + j_\eta \dot{w}' + j_\zeta \dot{v}' \phi - j_\zeta \dot{w}') W'_j \Big\} ds. \tag{3.46}
\end{aligned}$$

### 3.2.3.3 Nonlinear Stiffness Matrix

The nonlinear stiffness matrix is

$$\begin{aligned}
[K_{NL}]_{i,j} &= \int_0^L \left\{ W'_i (D_\xi v''^2 + D_\eta w''^2 - D_{\eta\zeta} v'' w'') W'_j \right. \\
&\quad + W''_i \left( D_\eta w' w'' - \frac{1}{2} D_{\eta\zeta} v'' w' \right) W'_j \Big\} ds \\
[K_{NL}]_{i,l+j} &= \int_0^L \left\{ W'_i (D_\zeta v'' w'' - D_{\eta\zeta} w''^2) W'_j \right. \\
&\quad + W''_i \left( D_\zeta v'' w' - \frac{1}{2} D_{\eta\zeta} v' v'' - 2D_{\eta\zeta} w' w'' \right) W'_j \Big\} ds
\end{aligned}$$

$$\begin{aligned}
[K_{NL}]_{i,l+m+j} &= \int_0^L \left\{ W_i' D_\xi v'' \Phi_j' + W_i'' (-D_\eta v'' - D_\eta \phi w'' + D_\zeta v'' + D_\zeta \phi w'') \Phi_j \right. \\
&\quad \left. + W_i'' (2D_{\eta\zeta} \phi v'' - 2D_{\eta\zeta} w'') \Phi_j \right\} ds \\
[K_{NL}]_{l+i,j} &= \int_0^L \left\{ W_i' (D_\zeta v'' w'' + D_{\eta\zeta} w''^2) W_j' \right. \\
&\quad \left. + W_i'' \left( D_\xi w' v'' - \frac{1}{2} D_{\eta\zeta} w' w'' \right) W_j' \right\} ds \\
[K_{NL}]_{l+i,l+j} &= \int_0^L \left\{ W_i' (D_\zeta v''^2 - D_{\eta\zeta} v'' w'') W_j' \right. \\
&\quad \left. + W_i'' \left( D_\zeta v' v'' + D_\zeta w' w'' - \frac{1}{2} D_{\eta\zeta} v' w'' \right) W_j' \right\} ds \\
[K_{NL}]_{l+i,l+m+j} &= \int_0^L \left\{ W_i'' (D_\eta \phi v'' - D_\eta w'' - D_\zeta \phi v'' + D_\zeta w'' + 2D_{\eta\zeta} v'') \Phi_j \right. \\
&\quad \left. + 2W_i'' D_{\eta\zeta} \phi w'' \Phi_j + W_i'' D_\xi w' \Phi_j' \right\} ds + [W_i D_\xi w' \Phi_j'']_{s=L} \\
[K_{NL}]_{l+m+i,j} &= \int_0^L \left\{ -\Phi_i D_{\eta\zeta} w'' W_j'' + \Phi_i' D_\xi v'' W_j' \right\} ds \\
[K_{NL}]_{l+m+i,l+j} &= \int_0^L \Phi_i (-D_\eta w'' + D_\zeta w'' + D_{\eta\zeta} v'') W_j'' ds \\
[K_{NL}]_{l+m+i,l+m+j} &= \int_0^L \Phi_i (D_\eta v''^2 - D_\eta w''^2 - D_\zeta v''^2 + D_\zeta w''^2 + 4D_{\eta\zeta} v'' w'') \Phi_j ds. \quad (3.47)
\end{aligned}$$

### 3.2.4 Forcing Vectors

#### 3.2.4.1 Linear Forcing Vector

The linear forcing vector is

$$\begin{aligned}
\{F_L\}_i &= \int_0^L W_i Q_w ds \\
\{F_L\}_{l+i} &= \int_0^L W_i Q_v ds \\
\{F_L\}_{l+m+i} &= \int_0^L \Phi_i Q_\phi ds. \quad (3.48)
\end{aligned}$$

### 3.2.4.2 Nonlinear Forcing Vector

The nonlinear forcing vector is

$$\begin{aligned}\{F_{NL}\}_i &= - \int_0^L W_i w' \int_s^L Q_u d\hat{s} ds \\ \{F_{NL}\}_{l+i} &= - \int_0^L W_i v' \int_s^L Q_u d\hat{s} ds.\end{aligned}\tag{3.49}$$

## 3.3 Numerical Implementation of the Structural Solver

### 3.3.1 Overview

The assumed-mode ordinary differential equation of motion (3.40) is evaluated numerically in FORTRAN 90 using explicit integration. Essentially, this process consists of calculating the mass, damping, and stiffness matrices and the force vectors at each time step.

### 3.3.2 Matrices

The time-invariant linear matrices are calculated only once using Simpson's  $\frac{1}{3}$  rule. The forcing vectors and nonlinear matrices are dependent upon time and, consequently, calculated for every time step.

From a computational perspective, the triple integrals in the nonlinear mass and damping matrices are particularly expensive. However, since the deformations are expressed in terms of separable variables, the time-dependent contribution can be extracted, enabling the spatial integrals to be computed once and accordingly multiplied by the corresponding time coefficients and summed subsequently.

For example, in the triple integral

$$- \int_0^L W'_i(s) w'(s, t) \int_s^L m(\hat{s}) \int_0^{\hat{s}} \dot{v}'(\tilde{s}, t) W'_j(\tilde{s}) d\tilde{s} d\hat{s} ds,\tag{3.50}$$

the deformations are expanded in terms of mode shapes and time coefficients:

$$\int_0^L W'_i(s) \left\{ \sum_{a=1}^l w_a(t) W'_a(s) \right\} \int_s^L m(\hat{s}) \int_0^{\hat{s}} \left\{ \sum_{b=1}^m \dot{v}_b(t) W'_b(\tilde{s}) \right\} W'_j(\tilde{s}) d\tilde{s} d\hat{s} ds.\tag{3.51}$$

The time coefficients and summations are rearranged to yield

$$\sum_{a=1}^l \sum_{b=1}^m \left\{ w_a(t) \dot{v}_b(t) \int_0^L W'_i(s) W'_a(s) \int_s^L m(\hat{s}) \int_0^{\hat{s}} W'_b(\tilde{s}) W'_j(\tilde{s}) d\tilde{s} d\hat{s} ds \right\}.\tag{3.52}$$

Furthermore,

$$\int_0^{\hat{s}} W'_b(\tilde{s}) W'_j(\tilde{s}) d\tilde{s}\tag{3.53}$$

has a closed form solution, essentially reducing the calculation of the triple integral at every time step to a once-computed double integral that undergoes double summation at subsequent time steps.

The remaining integrals in the nonlinear matrices are calculated in a similar manner, reducing the integrals to double summations.

### 3.3.3 Forcing Vectors

The forcing vectors are computed at every time step using Simpson's  $\frac{1}{3}$  rule. For the case of  $p$  point loads  $\mathbf{F}_i(t)$ , expressed in the inertial frame,

$$\mathbf{Q} = \begin{Bmatrix} Q_u \\ Q_v \\ Q_w \end{Bmatrix} = \sum_{i=1}^p \delta(s - s_i) \mathbf{F}_i, \quad (3.54)$$

where  $\delta(s)$  is the Dirac delta function (Haberman, 2004). This is done similarly for  $Q_\phi$  with the moment about the  $\xi$ -axis, leading to

$$\begin{aligned} \{F_L\}_i &= \int_0^L W_i Q_w ds = \sum_{j=1}^p W_i(s_j) F_{z_j}(t) \\ \{F_L\}_{l+i} &= \int_0^L W_i Q_v ds = \sum_{j=1}^p W_i(s_j) F_{y_j}(t) \\ \{F_L\}_{l+m+i} &= \int_0^L \Phi_i Q_\phi ds = \sum_{k=1}^q \Phi_i(s_k) M_{\xi_k}(t) \end{aligned} \quad (3.55)$$

and

$$\begin{aligned} \{F_{NL}\}_i &= - \int_0^L W_i w' \int_s^L Q_u ds = - \sum_{j=1}^p F_{x_j}(t) \int_0^{s_j} W_i(s) w'(s, t) ds \\ \{F_{NL}\}_{l+i} &= - \int_0^L W_i v' \int_s^L Q_u ds = - \sum_{j=1}^p F_{x_j}(t) \int_0^{s_j} W_i(s) v'(s, t) ds, \end{aligned} \quad (3.56)$$

or

$$\begin{aligned} \{F_{NL}\}_i &= - \sum_{j=1}^p \sum_{a=1}^l F_{x_j}(t) w_a(t) \int_0^{s_j} W_i(s) W'_a(s) ds \\ \{F_{NL}\}_{l+i} &= - \sum_{j=1}^p \sum_{a=1}^m F_{x_j}(t) v_a(t) \int_0^{s_j} W_i(s) W'_a(s) ds, \end{aligned} \quad (3.57)$$

where the integral has a closed-form solution.

### 3.3.4 Solution

Letting the time coefficients be represented by

$$\mathbf{X} = \{w_1, \dots, w_l, v_1, \dots, v_m, \phi_1, \dots, \phi_n\}, \quad (3.58)$$

equation (3.40) is rewritten such that

$$\frac{d}{dt} \begin{Bmatrix} \mathbf{X} \\ \dot{\mathbf{X}} \end{Bmatrix} = \begin{Bmatrix} \dot{\mathbf{X}} \\ [M_L + M_{NL}]^{-1} \{ \mathbf{F}_L + \mathbf{F}_{NL} - [K_L + K_{NL}] \mathbf{X} - [C_{NL}] \dot{\mathbf{X}} \} \end{Bmatrix}, \quad (3.59)$$

or in shorthand as

$$\dot{\mathbf{Y}} = \mathbf{F}(\mathbf{Y}, t). \quad (3.60)$$

At each point in time, (3.59) is integrated using a fourth-order Runge-Kutta method (Gerald and Wheatley, 2004):

$$\mathbf{Y}_{n+1} = \mathbf{Y}_n + \frac{1}{6} \Delta t (\mathbf{k}_1 + 2\mathbf{k}_2 + 2\mathbf{k}_3 + \mathbf{k}_4), \quad (3.61)$$

where

$$t_{n+1} = t_n + \Delta t \quad (3.62)$$

$$\mathbf{k}_1 = \mathbf{F}(\mathbf{Y}_n, t_n) \quad (3.63)$$

$$\mathbf{k}_2 = \mathbf{F}\left(\mathbf{Y}_n + \frac{1}{2} \Delta t \mathbf{k}_1, t_n + \frac{1}{2} \Delta t\right) \quad (3.64)$$

$$\mathbf{k}_3 = \mathbf{F}\left(\mathbf{Y}_n + \frac{1}{2} \Delta t \mathbf{k}_2, t_n + \frac{1}{2} \Delta t\right) \quad (3.65)$$

$$\mathbf{k}_4 = \mathbf{F}(\mathbf{Y}_n + \Delta t \mathbf{k}_3, t_n + \Delta t). \quad (3.66)$$

This provides the time coefficients and the first derivatives of the time coefficients for each time step. Consequently, the deformation of the elastic axis can be calculated with respect to time by summing the product of the time coefficients and the mode shapes at the position of interest. Knowing the deformed position of each point along the elastic axis as well as  $\phi$ , the angle about  $\xi$ , which the cross section coordinate system is rotated, enables the displacement of any point on the structure to be calculated.

## 3.4 Structural Solver Validation

### 3.4.1 Method

The structural solver is validated by comparing results with those generated by Abaqus, a commercial finite element software package. Validation consists of comparing frequencies and deflections obtained with the beam model developed herein and the commercial finite element code Abaqus.

### 3.4.2 Natural Frequencies

Three beams are used as test cases for comparing natural frequencies obtained by using Abaqus and the present beam model. Each of the beams is modeled in Abaqus using quadratic three-dimensional continuum elements. Furthermore, for each case, a grid convergence test is done by refining the mesh twice. The five frequencies corresponding to the first five vibrational modes are compared with those obtained by the linear contribution to the beam model. For these comparisons, the beam model uses five mode shapes for each of the three independent degrees of freedom.

The linear contribution to the beam model provides a system of 15 coupled linear second-order differential equations for which a sinusoidal analytical solution is obtainable for the mode shape time coefficients. This solution provides the natural frequencies of the beam.

### 3.4.2.1 Case 1: A Tapered Beam

The first beam used for frequency comparison is a tapered, homogeneous beam composed of aluminum alloy 6061-T6. This beam choice provides an initial example of a non-uniform beam. 6061-T6 has a density of 2710 kg/m<sup>3</sup>, a Young's modulus of 70 GPa, and a shear modulus of 26 GPa (Beer et al., 2006). The beam is shown in Figure 3.4. It is 20 cm long and consists of a 2 cm × 1 cm cross section at the fixed end and a 1 cm × 1 cm cross section at the free end. The properties of the tapered beam are listed in Table 3.1. For a rectangular cross section with dimensions  $a \times b$ , where  $a$  is the greater of the two, the torsion constant can be approximated as follows (Roark et al., 2002):

$$K = ab^3 \left[ \frac{1}{3} - 0.21 \frac{b}{a} \left( 1 - \frac{b^4}{12a^4} \right) \right] \quad (3.67)$$

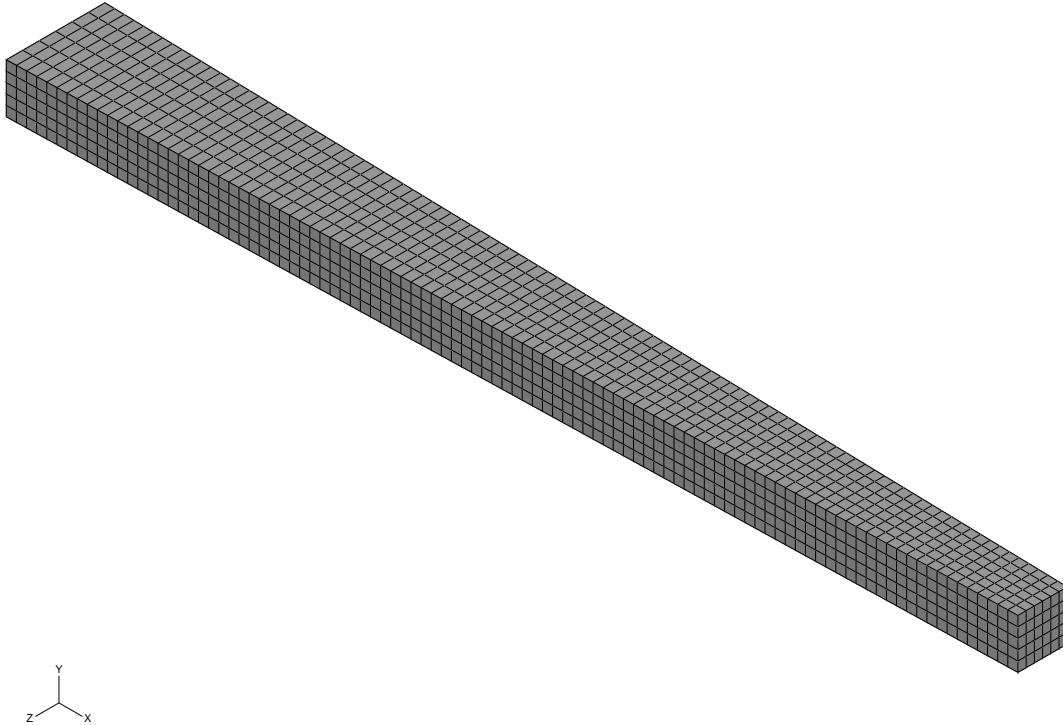


Figure 3.4: Tapered beam with 100×5×6 mesh.

Table 3.2 shows the mesh sizes for the three finite element meshes. For each of the three meshes, the first five frequencies are tabulated in Table 3.3. The error is measured by taking the absolute value of the difference between the frequencies of the finest finite element mesh and the assumed-mode solution and dividing by that of the finite element mesh.

The assumed-mode solution favorably agrees with the finite element solution, providing little

Table 3.1: Properties of tapered beam.

Parameter	Value
$m(s)$	$0.542 - 1.355s$ kg/m
$j_\xi(s)$	$(0.22583 - 1.4679s + 3.3875s^2 - 2.8229s^3) \times 10^{-4}$ kg m <sup>2</sup> /m
$j_\eta(s)$	$(0.18067 - 1.3550s + 3.3875s^2 - 2.8229s^3) \times 10^{-4}$ kg m <sup>2</sup> /m
$j_\zeta(s)$	$(0.045167 - 0.11292s) \times 10^{-4}$ kg m <sup>2</sup> /m
$j_{\eta\zeta}(s)$	0 kg m <sup>2</sup> /m
$D_\xi(s)$	$173.33 + \frac{9.1 \times 10^{-10}}{(0.02-0.05s)^5} - \frac{1.092}{(0.02-0.05s)}$ $-433.33s - \frac{(2.275 \times 10^{-9}s)}{(0.02-0.05s)^5} + \frac{(2.73s)}{(0.02-0.05s)}$ N m <sup>2</sup>
$D_\eta(s)$	$466.67 - 3500s + 8750s^2 - 7291.7s^3$ N m <sup>2</sup>
$D_\zeta(s)$	$116.67 - 291.67s$ N m <sup>2</sup>
$D_{\eta\zeta}(s)$	0 N m <sup>2</sup>

Table 3.2: Finite element mesh sizes of tapered beam.

Mesh Number	Elements Along $x, y, z$	Total Elements
1	$50 \times 3 \times 3$	450
2	$67 \times 3 \times 5$	1005
3	$100 \times 5 \times 6$	3000

Table 3.3: First five frequencies of tapered beam.

Mode	Abaqus			Modal Representation [Hz]	Error
	Mesh 1 [Hz]	Mesh 2 [Hz]	Mesh 3 [Hz]		
1	252.75	252.71	252.64	251.89	0.297%
2	445.46	445.38	445.30	446.20	0.202%
3	1362.1	1361.8	1361.4	1370.8	0.686%
4	2081.4	2080.8	2080.4	2130.5	2.41%
5	3594.1	3593.4	3592.1	3671.3	2.16%



error.

### 3.4.2.2 Case 2: A Twisted Beam

A twisted, homogeneous beam composed of aluminum alloy 6061-T6 is the second beam used for frequency comparison. This beam is chosen as it provides an example of a non-uniform beam for which the principal mass and bending axes vary with respect to the reference coordinate system. The beam is shown in Figure 3.5. It is 10 m long and consists of a  $1\text{ m} \times 0.5\text{ m}$  cross section that is unrotated at the fixed end and linear rotated such that it is at a  $45^\circ$  angle about the centroidal axis at the free end. The properties of the twisted beam are presented in Table 3.4. For a rectangular cross section with an aspect ratio of 2, the torsion constant  $K$  is  $0.229ab^3$ , where  $a$  and  $b$  are respectively the lengths of the longer and shorter sides (Ugural and Fenster, 1981).

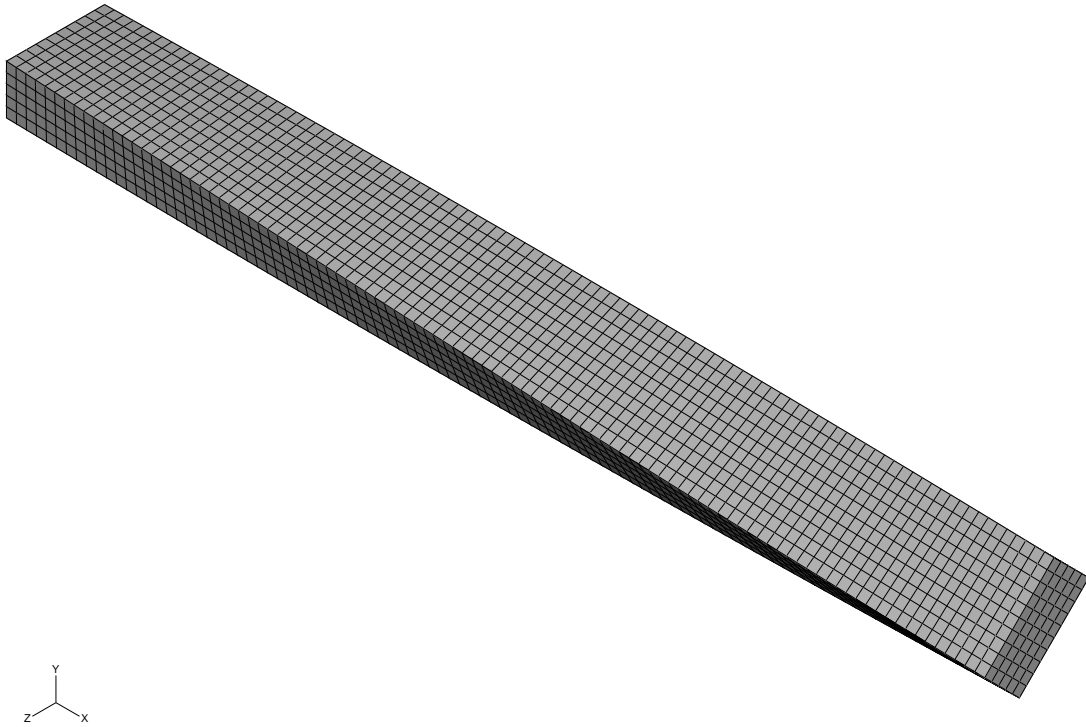


Figure 3.5: Twisted beam with  $100 \times 5 \times 10$  mesh.

As with the tapered beam, Table 3.5 provides the mesh sizes for the three finite element meshes. For each of the three meshes, the first five frequencies and the error are tabulated in Table 3.6. The assumed-mode solution agrees nicely with the finite element solution.

### 3.4.2.3 Case 3: A Composite Beam

The final beam used for frequency analysis is a uniform composite beam consisting of aluminum alloy 6061-T6 and steel. Steel has a density of  $7860\text{ kg/m}^3$ , a Young's modulus of  $200\text{ GPa}$ , and a modulus of rigidity of  $77.2\text{ GPa}$  (Beer et al., 2006). Three quarters of the beam are aluminum, while the remaining quarter is steel. The beam is shown in Figure 3.6. This beam is selected because it provides an example of a beam for which the mass and elastic centers of each cross section are

Table 3.4: Properties of Twisted Beam

Parameter	Value
$m(s)$	1355 kg/m
$j_\xi(s)$	141.15 kg m <sup>2</sup> /m
$j_\eta(s)$	$70.573 + 42.344 \cos \frac{\pi s}{20}$ kg m <sup>2</sup> /m
$j_\zeta(s)$	$70.573 - 42.344 \cos \frac{\pi s}{20}$ kg m <sup>2</sup> /m
$j_{\eta\zeta}(s)$	$-42.344 \sin \frac{\pi s}{20}$ kg m <sup>2</sup> /m
$D_\xi(s)$	$7.4425 \times 10^8$ N m <sup>2</sup>
$D_\eta(s)$	$(1.8229 + 1.0938 \cos \frac{\pi s}{20}) \times 10^9$ N m <sup>2</sup>
$D_\zeta(s)$	$(1.8229 - 1.0938 \cos \frac{\pi s}{20}) \times 10^9$ N m <sup>2</sup>
$D_{\eta\zeta}(s)$	$-1.0938 \cos \frac{\pi s}{20} \times 10^9$ N m <sup>2</sup>

Table 3.5: Finite element mesh sizes of twisted beam.

Mesh Number	Elements Along $x, y, z$	Total Elements
1	$50 \times 2 \times 5$	500
2	$67 \times 3 \times 7$	1407
3	$100 \times 5 \times 10$	5000

Table 3.6: First five frequencies of twisted beam.

Mode	Abaqus			Modal Representation [Hz]	Error
	Mesh 1 [Hz]	Mesh 2 [Hz]	Mesh 3 [Hz]		
1	4.1440	4.1423	4.1410	4.1291	0.288%
2	8.0006	7.9981	7.9961	8.0229	0.335%
3	26.265	26.253	26.245	26.483	0.907%
4	46.756	46.737	46.723	48.425	3.64%
5	58.102	58.041	58.024	57.407	1.06%

offset in both dimensions. Furthermore, the principal bending and mass axes are neither parallel mutually nor to the reference coordinate system. The beam is 1 m long with a  $5\text{ cm} \times 3\text{ cm}$  cross section. The properties of the composite beam are presented in Table 3.7. The torsional stiffness is approximated by multiplying an area-weighted average of the modulus of rigidity by the result of (3.67) for the cross section.

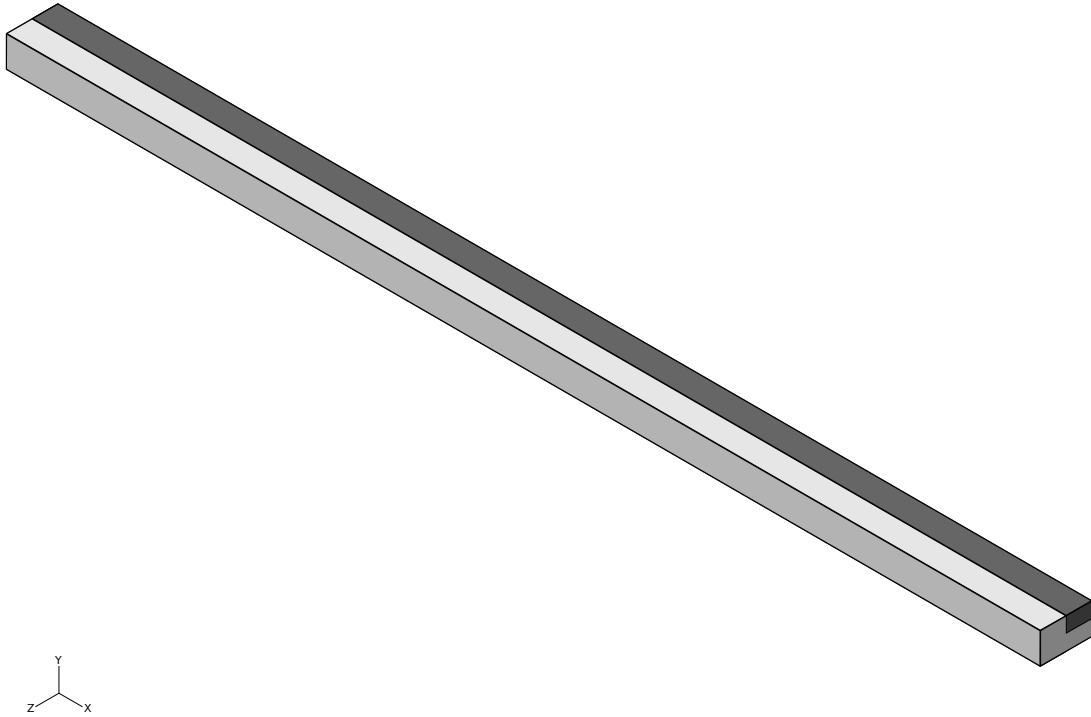


Figure 3.6: Composite beam.

Table 3.8 tabulates the mesh sizes for the three finite element meshes, and Table 3.9 lists the first five frequencies and the error. The frequencies calculated by the beam modal representation provided accurate results while reducing the computational time by approximately two orders of magnitude.

Table 3.7: Properties of composite beam.

Parameter	Value
$e_\eta(s)$	$3.7524 \times 10^{-5} \text{ m}$
$e_\zeta(s)$	$-6.2539 \times 10^{-5} \text{ m}$
$m(s)$	$5.9963 \text{ kg/m}$
$j_\xi(s)$	$1.5668 \times 10^{-3} \text{ kg m}^2/\text{m}$
$j_\eta(s)$	$1.1521 \times 10^{-3} \text{ kg m}^2/\text{m}$
$j_\zeta(s)$	$0.41474 \times 10^{-3} \text{ kg m}^2/\text{m}$
$j_{\eta\zeta}(s)$	$0.12276 \times 10^{-3} \text{ kg m}^2/\text{m}$
$D_\xi(s)$	$1.0931 \times 10^4 \text{ N m}^2$
$D_\eta(s)$	$2.9616 \times 10^4 \text{ N m}^2$
$D_\zeta(s)$	$1.0662 \times 10^4 \text{ N m}^2$
$D_{\eta\zeta}(s)$	$0.31212 \times 10^4 \text{ N m}^2$

Table 3.8: Finite element mesh sizes of composite beam.

Mesh Number	Elements Along $x, y, z$	Total Elements
1	$77 \times 2 \times 4$	616
2	$100 \times 4 \times 6$	2400
3	$143 \times 4 \times 8$	4576

Table 3.9: First five frequencies of composite beam.

Mode	Abaqus			Modal Representation [Hz]	Error
	Mesh 1 [Hz]	Mesh 2 [Hz]	Mesh 3 [Hz]		
1	23.099	23.091	23.089	23.036	0.230%
2	39.675	39.668	39.665	39.662	0.00756%
3	144.18	144.13	144.12	144.30	0.125%
4	245.73	245.68	245.66	248.21	1.04%
5	401.19	401.01	400.98	403.61	0.656%

### 3.5 Finite Element Method Code for Plates

Although the nonlinear beam element presented above excels on both accuracy and efficiency, not all structures can be modeled by beams. For this reason, and because we prefer to have access to the source code rather than using canned commercial codes, during this project we also developed a finite element method for plates.

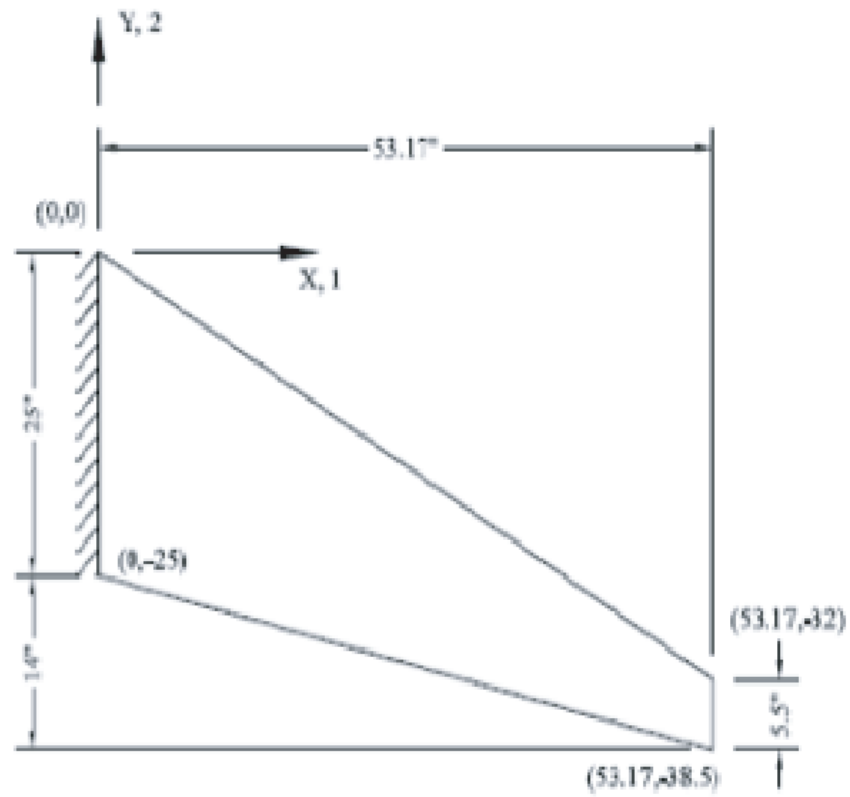
The Bogner-Fox-Schmit (BFS) rectangular conforming element was considered for rectangular and triangular finite elements used herein (Bogner et al., 1966). The FEM employed three-node triangular Mindlin (MIN3) plate element with an improved transverse shear term (Tessler and Hughes, 1985). The nodal degree of freedom (DOF) of each BFS element was composed of 16 bending and 8 in-plane DOF. The MIN3 element has a total of 15 DOF, 5 at each apex node. The bending node DOF comprises transverse displacements and normal rotations, and the in-plane node DOF comprises in-plane displacements. The elements have been studied for similar cases, including composite panels under the combined aerodynamic and acoustic pressures based on modal analysis. Further, the MIN3 triangular element was used to study LCO of arbitrary laminated anisotropic composite rectangular plates. The FEM used the BFS and Min3 elements. The Generic Transport Wing (GTW), as described by Edwards et al. (2009), was examined in detail.

The Generic Transport Wing (GTW) provided us a platform for computational fluid dynamics/computational structural mechanics experimental validation. The GTW was used in legacy experiments within the NASA LaRC TDT Facility. Features of the GTW include: a structure of solid aluminum with balsa skin, LCO responses exhibited within the transonic regime, LCOs exhibited with a winglet present and noticeable differences in vibration characteristics from the baseline, and repeatable measurements of LCO. The GTW geometry is shown in the Fig. 3.7.

Indeed, the LCO was present on the GTW with winglet (as well as the other configurations), and the winglet made noticeable differences in the vibration characteristics. The plate-based FEM model we developed was used to replicate the results published by Edwards et al. (2009). The vibration characteristics are given in Table 3.10, and the first three modes are illustrated in Fig. 3.8.

Table 3.10: First four frequencies of generic transport wing.

Mode	Measured [Hz]	FEM [Hz]	Error [%]
1st bending	4.08	4.07	0.245
2nd bending	14.0	14.5	3.571
1st torsion	31.5	29.3	6.984
2nd torsion	58.1	57.4	1.205



Generic Transport Wing (GTW)

Figure 3.7: Generic transport wing.

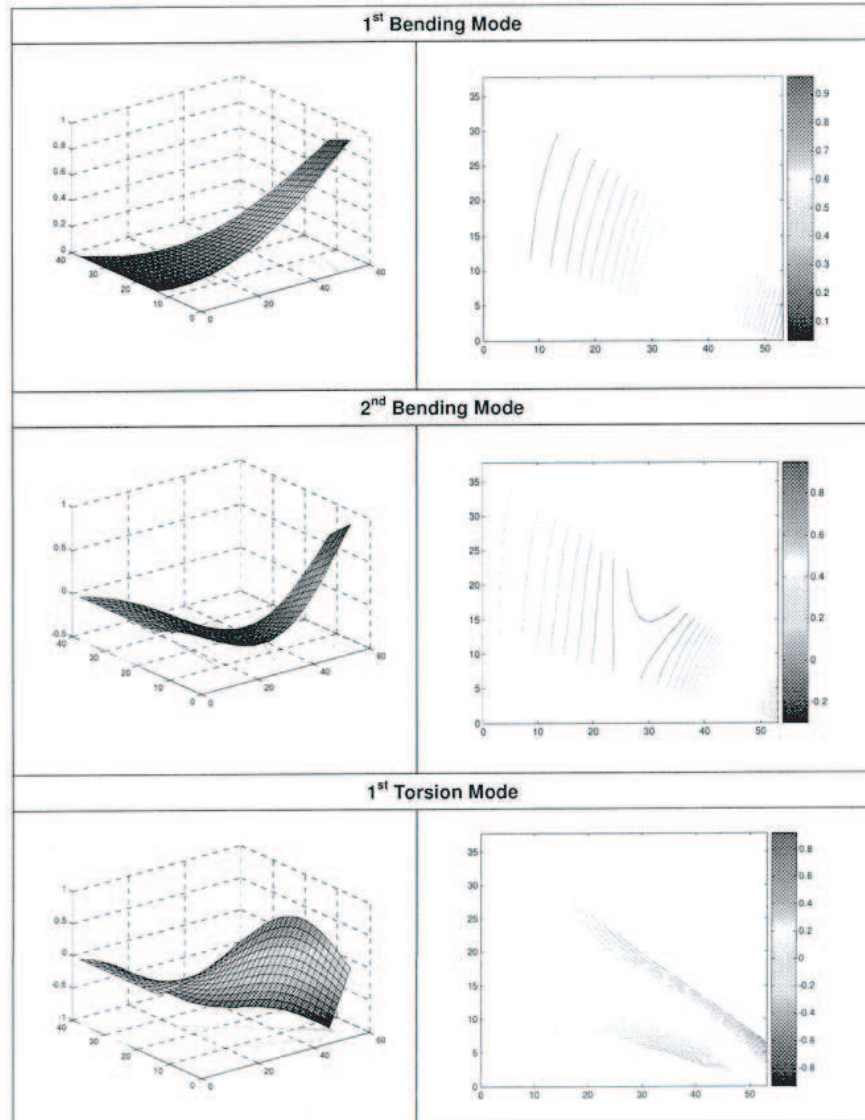


Figure 3.8: Generic transport wing: first three modes.

## Chapter 4

# Continuation Methods

Since the design space of new air vehicles is vast, determination of nonlinear responses, vehicle trim states and vehicle stability must be addressed in an efficient, methodical manner. Numerical Continuation will reveal various bifurcation characteristics including both subcritical and supercritical bifurcations. The former case is of significant interest because the subcritical bifurcations indicate limit cycle oscillations below the linear stability boundary. Further, subcritical bifurcations depend upon disturbances, and have a hysteresis between onset and recovery speeds. This behavior cannot be studied with linear methods. Subcritical bifurcations are anticipated for highly deformable, high aspect ratio wings and may reveal adverse vehicle performance.

Numerical continuation methods offer a robust and efficient solution to these needs. In our opinion, one limitation is the ability to properly represent the aerodynamic loads as appropriate for the regime. However, with the inclusion of the variable-fidelity reduced-order model, the Continuation Method permits direct analysis of the system without requiring explicit linearization or compromise on a physical description of the flow. Thus, the trim states of the nonlinear system and the stability characteristics of the air vehicle can be evaluated in a continuous manner as system parameters are varied. Continuation Methods are direct methods for examining the bifurcation characteristics of the nonlinear equations.

We use the software tool AUTO for continuation and bifurcation analyzes of the nonlinear ordinary differential equations (Doedel, 1981). AUTO automates the computation of solutions of this parameter-dependent system of equations. The system possesses multiple solutions, and it is valuable to compute the set of solutions and search for those solutions with specific desirable properties as a system parameter is varied. This solution set forms a bifurcation diagram, i.e., a smooth curve (or surface) representing the solution for the varying system parameter. Tools such as AUTO facilitate parametric studies and minimize time consuming numerical simulations. The computation of such bifurcation diagrams and associated singularities is captured within the domain of the numerical continuation algorithm. AUTO has the capability to compute periodic solutions such as the limit cycle oscillations (LCOs). In addition, AUTO determines the stability of the steady state solutions. AUTO permits a two-parameter continuation solution of Hopf and other bifurcation points. A detailed description on the features of AUTO can be found in (Doedel et al., 2002).

The method permits direct eigen-analysis of the system without resorting to explicit linearization. Thus, the nonlinear trim states and their stability characteristic can be evaluated in a continuous manner as a single system parameter is varied using the exact nonlinear expressions. Eigenvalues obtained by the method are used to ascertain the extent of coupling between rigid body and flexible body modes. Various bifurcation points of the system are found and permit evaluation



of stability boundaries. Also, the method is used to examine the presence of LCOs. In such a situation, the dynamic characteristic of the system is dependent on initial condition.

We have applied the continuation method to the nonlinear aeroelastic responses for vehicles with moderate-to-high deformations. The wing was modeled using nonlinear structural equations of motion for a cantilevered beam with in-plane, out-of-plane, and torsional couplings. In the form of a bifurcation diagram, Fig. 4.1 is an example of a bifurcation diagram created as part of the continuation tool. The tool permits nonlinear analysis of the set of governing equations. The approach detects the bifurcation points, determines equilibria and stability states, determines amplitude of periodic solutions (e.g., stable LCOs), and rapidly identifies character of design. We have shown that it duplicates time-domain simulation, but such exhaustive simulation to “bracket” the stability boundaries is avoided.

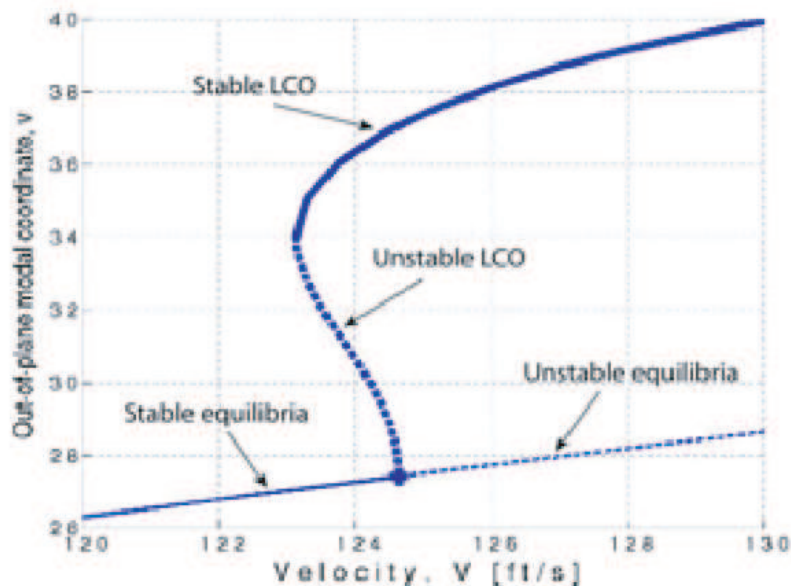


Figure 4.1: Example bifurcation diagram showing the effect of trim constraint.

Figure 4.1 shows amplitudes of the out-of-plane modal coordinate, equilibria, and limit cycles as the freestream velocity is varied. Bifurcation occurs at the critical velocity. From the bifurcation point, the thin solid line represents a branch of stable equilibria, the thin dashed line represents a branch of unstable equilibria, and the thick solid line represents a branch of stable LCOs. An important observation is that the trim model shows a change in amplitude in both equilibria and LCOs. In addition, the continuation tool allows one to explore the parameter space without missing details.

Figure 4.2 shows results for the wing with a trim constraint such that the wing possesses a root angle. Under flight conditions requiring a root angle of attack to satisfy the trim constraint, the static deformation and stability characteristics change. The trim condition leads to a statically deformed shape of the wing that must vary with the freestream velocity and, as one might expect, static deformation of the wing increases with increasing freestream velocity. The system loses stability at a velocity of approximately 124 ft/sec.

The left view of Fig. 4.2 shows a bifurcation diagram with the supercritical branch which describes the response at velocities higher than the bifurcation point. The nature of bifurcation

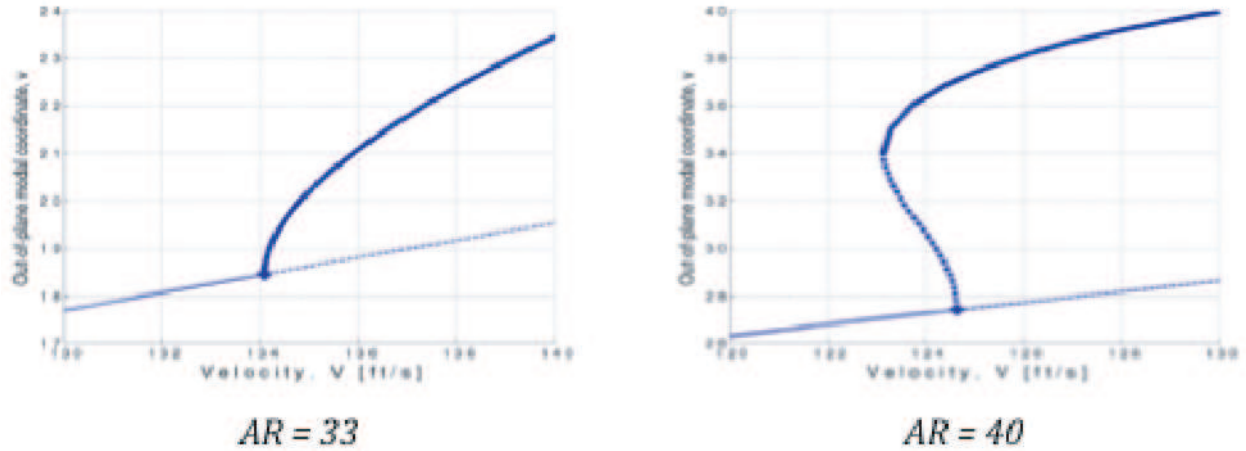


Figure 4.2: Sensitivity to aspect ratio: transition to subcritical from supercritical behavior at angle of attach 2.8 deg and in-plane to out-of-plane stiffness ratio,  $\beta_n=4$ .

depends on the angle of attack imposed by the trim condition as well as system design properties such as the in-plane to out-of-plane stiffness ratios ( $\beta_n$ ). In addition, the right view indicates the vehicle transitions to a subcritical branch at a higher aspect ratios. In linear analysis, the bifurcation point is the flutter velocity, and is the only response predicted by such analysis. The supercritical branch, as well as the stable branch (solid line) in the right view, describes limit cycle behavior. The nonlinear dynamics of this system are governed by the existence of a disturbance. With a disturbance, the system becomes entrained in the LCO with amplitude as shown by the thick solid line.

In summary, the Continuation Method provides an efficient method of nonlinear analysis for the aeroelastic system. The method eliminates “bracketing” approaches inherent of time domain simulation of nonlinear equations. Continuation detects bifurcations, defines equilibria and stability, determines amplitude of LCOs, characteristics, and identifies design characteristics in a rapid, comprehensive manner.

## Chapter 5

# A Novel Flow Solver Grid Generator for Aircraft with Extreme Wing Deformation

Grid generation is an important part of computational fluid dynamics, which greatly affects the accuracy of the numerical results. Grid quality has an even stronger effect on solution accuracy when simulating unsteady flows, and especially when the mesh deforms, like in aeroelasticity simulations. This chapter presents a new grid generation algorithm for aircraft with extreme wing deformation. The next section briefly presents background information on the grid generator that was enhanced during this project. The following section presents the conformal mappings proposed to enhance the existing grid generator. The last section compares the grid qualities of the two grid generators.

### 5.1 Background information

The new grid generation algorithm proposed herein was implemented into an existing mesh generation code (Cizmas and Gargoloff, 2008). This existing grid generation code discretized the computational domain of the flow solver using a hybrid grid consisting of hexahedra and triangular prisms. Because of the wing-fuselage configuration, it was possible to divide the computational domain into layers that were topologically identical, as shown in Fig. 5.1. Therefore, a 2.5-D grid could be used to discretize the 3-D domain, which simplified the grid generation algorithm.

The topologically identical nodes of adjacent layers were interconnected to generate the volume elements that were either triangular prisms or hexahedra. To better control mesh size near the wing, each layer had a structured O-grid around the wing, and an unstructured grid at the exterior of the O-grid. The O-grid allowed clustering cells in the direction normal to the structure to properly capture boundary layer effects. The unstructured grid was flexible in filling the rest of the domain.

The O-grid algorithm previously used (Cizmas and Gargoloff, 2008) was based on a Poisson solver which did not enforce grid orthogonality. As a result, the quality of the O-grid deteriorated near the leading and trailing edges of the wing. To alleviate this problem, a conformal mapping algorithm was developed herein, which assured grid orthogonality over the entire O-grid. Grid orthogonality is also beneficial for the cases when wing chord-wise bending is significant. In these cases, a good quality grid based on the Poisson solver is difficult to obtain for all chord-wise bending configurations.

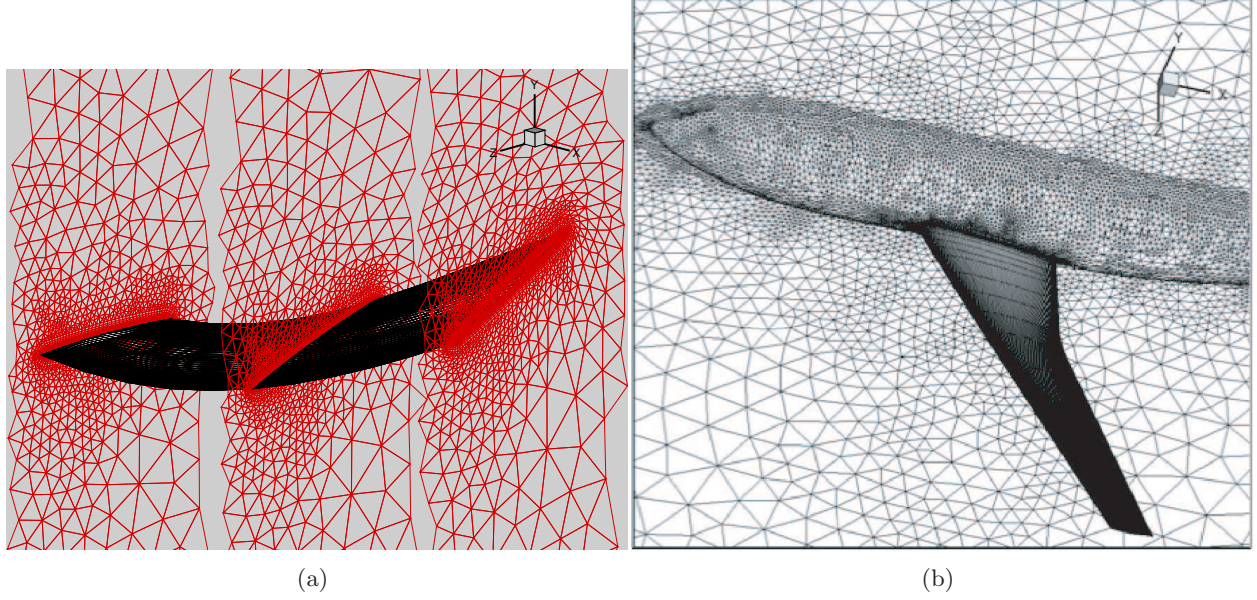


Figure 5.1: Grid generator: (a) detail of topologically identical layers along the wing, and (b) aircraft configuration.

## 5.2 Conformal Mapping

The conformal mapping used herein to generate the O-grid is an extension of the Carafoli method for determining the velocity and pressure distribution on airfoil cascades, assuming the flow is inviscid, incompressible and potential (Berbente and Cizmas, 1990). This conformal mapping is used for two purposes: (1) to generate the grid around the wing, and (2) to provide a start-up value for the velocity and pressure field in the O-grid.

The conformal mapping proposed herein consisted of three transformations that mapped the exterior of a unit circle onto either an isolated airfoil or an airfoil in a cascade. It is known that when the distance between airfoils is larger than approximately three chords, the effect of the neighboring airfoil is negligible. As a result, the user has the option to generate a grid for either an isolated airfoil or a cascade airfoil by selecting the distance between airfoils. Therefore, this grid generation algorithm can also be used for turbomachinery flows.

The first conformal mapping of the sequence is the Weinig-Manea transformation (Berbente and Cizmas, 1990)

$$z = \frac{t}{2\pi} \left( e^{i\lambda} \ln \frac{\zeta + R}{\zeta - R} + e^{-i\lambda} \ln \frac{R\zeta + 1}{R\zeta - 1} + B \right), \quad (5.1)$$

where  $t$  was the cascade pitch,  $\lambda$  was the stagger angle,  $\zeta$  was the complex variable of the mapped circle domain,  $z$  was the complex variable of the airfoil domain, and  $R$  and  $B$  were constants that were determined as a function of the solidity and stagger angle. Function (5.1) maps the exterior of the unit circle into a cascade of flat plates. Using (5.1) with the translation and homothety of the unit circle generates cascade airfoils with various thicknesses and curvatures.

To generate the grid and find the velocity field for a given airfoil, a conformal mapping similar to (5.1) would be needed, which maps the unit circle onto the wing airfoil. To achieve this goal,

a series of conformal mappings are determined by going backward, that is, from the airfoil to the unit circle.

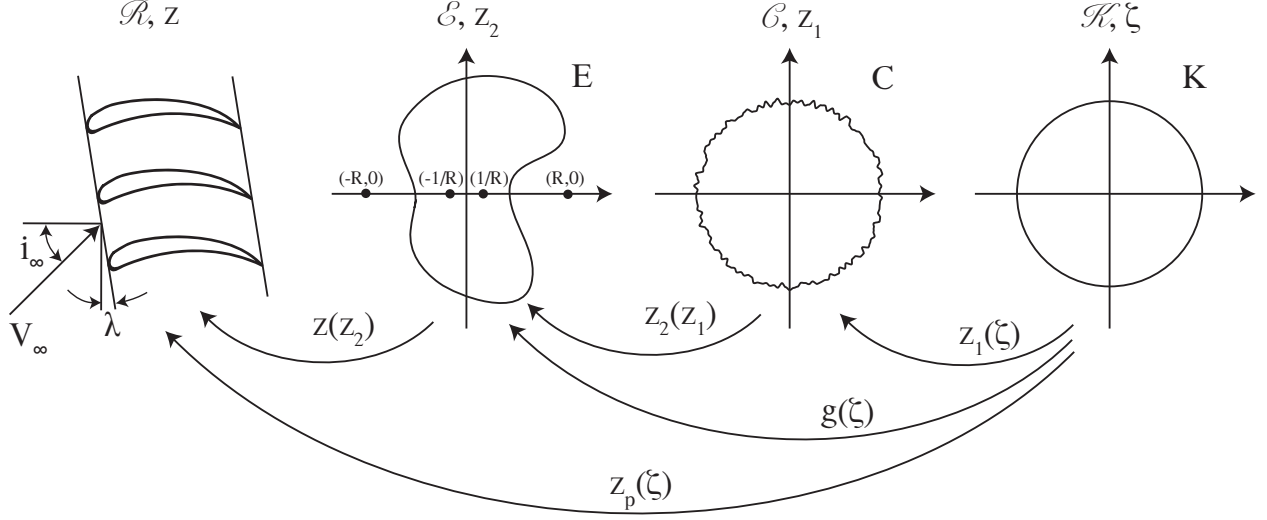


Figure 5.2: Conformal mapping components.

The sequence of mappings, shown in Fig. 5.2, consists of: (1) conformal mapping  $z(z_2)$  given by (5.1) where  $\zeta$  was substituted by  $z_2$ , (2) conformal mapping

$$z_2 = \left( z_1 - \frac{c^2}{z_1} \right) e^{i\tau} + z_0 \quad (5.2)$$

which represents the mapping of a circle to an ellipse, where  $\tau$  is the angle of the axes of the ellipse,  $c^2 = (b^2 - a^2)/4$  with  $a$  and  $b$  being the axes of the ellipse, and (3) conformal mapping

$$z_1 = \sum_{j=-1}^{m-2} C_{-j} \zeta^j, \quad C_{-j} \in \mathbb{C}, \quad (5.3)$$

where the constants  $C_{-j}$  were determined given a contour  $C$  in plane  $\mathcal{C}$ .

The implementation of the numerical algorithm that calculates the conformal mapping is briefly described herein. For a given airfoil shape, the Newton-Raphson method was used to determine the shape of the contour  $E$  in plane  $\mathcal{E}$ . The closest ellipse to contour  $E$  was then obtained by determining  $z_0$ ,  $a$ ,  $b$  and  $\tau$  using the least squares method. The coordinates of contour  $C$  in plane  $\mathcal{C}$  were determined using a Newton-Raphson method applied to the conformal mapping (5.2). The complex coefficients  $C_{-j}$  were determined by rewriting (5.3) in polar coordinates

$$z_1 = \sum_{j=-1}^{m-2} (A_{-j} + iB_{-j}) r^{-j} (\cos j\varphi - i \sin j\varphi),$$

dividing the unit circle  $K$  in  $2m$  equal segments ( $m = 2^k, k \in \mathbb{N}$ ) and using the orthogonality of trigonometric functions with discrete arguments.

Once the conformal mappings  $z_2(z_1)$  and  $z_1(\zeta)$  are known, the conformal mapping from the



unit circle to the airfoil was calculated as

$$z_p = z \circ z_2 \circ z_1$$

Figure 5.3 shows a detail of the structured and unstructured grids as seen along the  $y$ -axis. The structured O-grid was generated using the conformal mapping approach presented above.

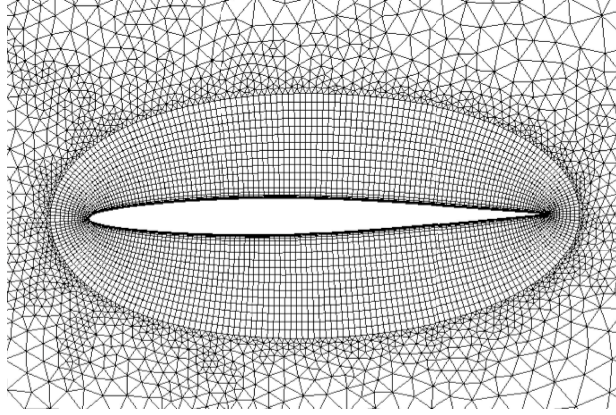


Figure 5.3: Conformal mapping O-grid surrounded by unstructured grid.

### 5.3 Grid Quality

The quality of the unstructured mesh was investigated in (Cizmas and Gargoloff, 2008). To evaluate the quality of the structured mesh, an indicator based on angles is proposed herein. This indicator assessed the quality of the layers perpendicular to the wing span direction. Therefore, the three-dimensional grid quality was reduced to a two-dimensional grid quality problem.

Based on angles, the cell with the highest quality is a rectangle. Consequently, the quality indicator was defined as  $q = 0.25 \sum_{i=1,4} \sin \alpha_i$ , where  $\alpha_i$  is the angle at corner  $i$ . As a result, the mesh quality improved as the indicator got closer to 1, the maximum value of  $q$ .

Figure 5.4 shows the contour plots of the mesh quality indicator of an O-grid generated using the Poisson solver and the conformal mapping. The grid generated using the Poisson solver had 6250 nodes while the grid generated using the conformal mapping had 6400 nodes. The average angle for the Poisson solver was 63 deg, while for the conformal mapping was 81 deg. Note that although the conformal mapping generates an orthogonal grid, the edges of the cells are approximated by straight lines and therefore the average angle was not 90 deg. Figure 5.4 shows that the grid quality of the conformal mapping grid is superior to that of the Poisson solver.

To test the conformal mapping algorithm for extreme cases of cross-wise bending, the wing deformation was amplified as shown in Fig. 5.5. As expected, the quality of the grid generated using conformal mapping was good, in spite of the large cross-wise deformation.

The grid generation algorithm was designed such that the grid connectivity remained unchanged, while the mesh deformed as the wing bent and twisted under aerodynamic loads. The algorithm for grid deformation was applied in two steps: (1) grid translation, and (2) grid rotation about the three axes (Cizmas and Gargoloff, 2008). The O-grid layers deformed as the wing cross-

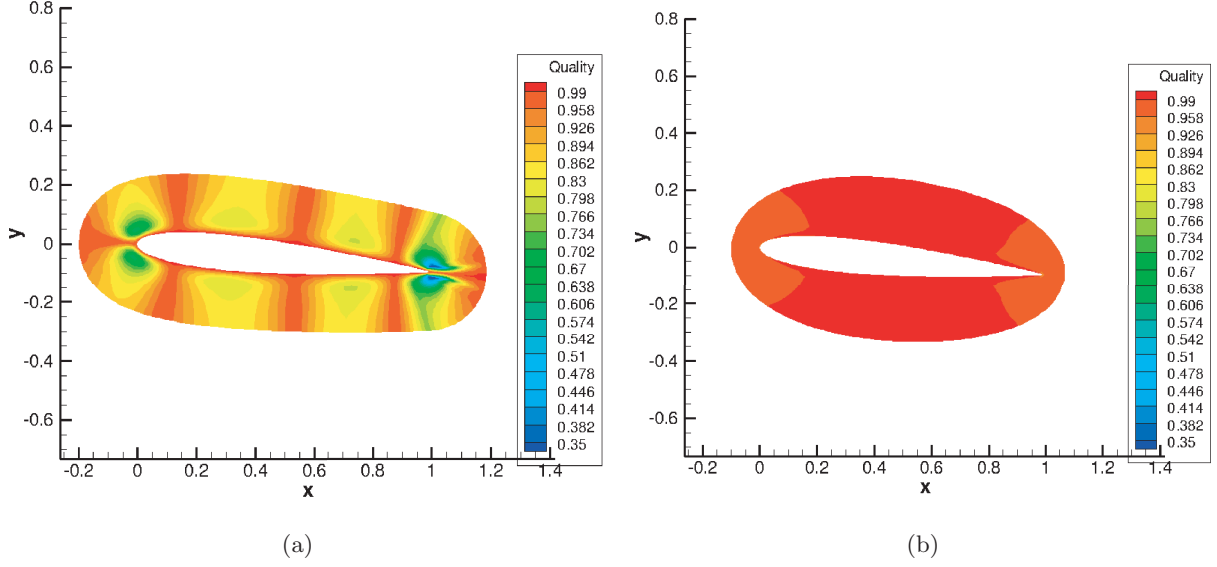


Figure 5.4: Grid quality based on angle: (a) Poisson solver, and (b) conformal mapping.

section deformed. The unstructured grid was deformed in the  $xz$ -plane using a spring analogy technique (Batina, 1990). The nodes of each layer were also translated in the  $y$ -direction according to the wing deformation.

The grid was rotated and stretched about the  $x$ -,  $y$ -, and  $z$ -axes. The numerical values of the rotation angles  $\theta_x$ ,  $\theta_y$ , and  $\theta_z$  were calculated using data provided by the structural solver (Cizmas and Gargoloff, 2008). Figure 5.6 shows the undeformed and deformed grids for the Goland wing (Eastep and Olsen, 1980; Snyder et al., 2003). In this case, the deformation at the tip was approximately 60% of the wing semi-span length, illustrating that the grid deformation algorithm is robust and precludes the need for regriding, even at large deformations.

This grid generation and deformation algorithm allowed the reduction of the computational cost of grid generation by a factor of 3.6 or more (Cizmas and Gargoloff, 2008), while maintaining the grid topology unchanged. Having an unchanged topology, while the grid deformed, simplified both the parallel and multigrid algorithms.

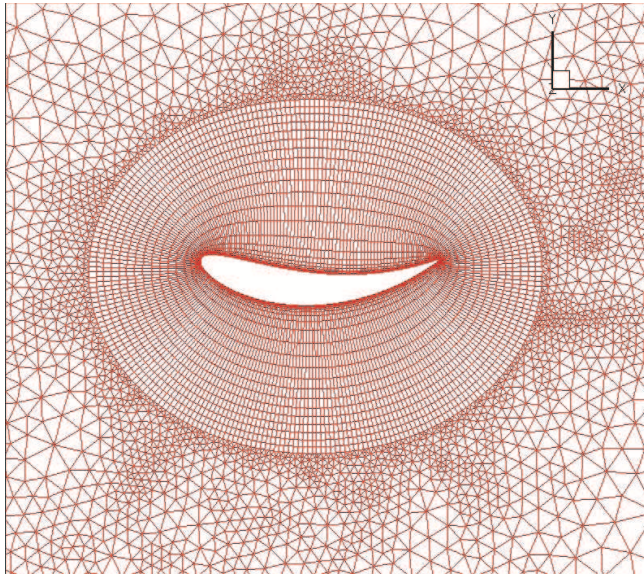


Figure 5.5: Hybrid grid around the wing with O-grid generated using conformal mapping, assuming exaggerated chord-wise deformation.

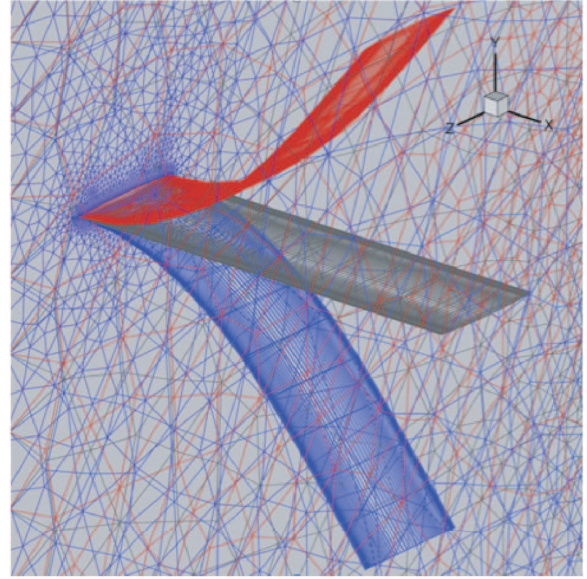


Figure 5.6: Isometric projection of deformed and undeformed grids of the Goland wing - tip deformation of 60% of wing semi-span (Cizmas and Gargoloff, 2008).



# Bibliography

- Batina, J. T. (1990, August). Unsteady Euler airfoil solutions using unstructured dynamic meshes. *AIAA Journal* 28(8), 1381–1388.
- Beer, F. P., E. R. Johnston, Jr., and J. T. DeWolf (2006). *Mechanics of Materials* (4 ed.). McGraw-Hill Higher Education.
- Berbente, C. and P. Cizmas (1990). An extension of flat plate cascade conformal mapping to cascades of a specified shape. *Journal of the Romanian Academy, Studii si Cercetari de Mecanica Aplicata* 49(5-6), 466–476. (in Romanian).
- Bisplinghoff, R. L., H. Ashley, and R. L. Halfman (1996). *Aeroelasticity*. Dover Publications, Inc.
- Bogner, F. K., R. L. Fox, and L. A. Schmit (1966). The generation of inter-element compatible stiffness and mass matrices by the use of interpolation formulas. Technical Report AFFDL-TR-66-80, Wright-Patterson AFB, Ohio. pp. 396-443.
- Brenner, T. A., P. G. A. Cizmas, T. J. O’Brien, and R. W. Breault (2009, January). Practical aspects of the implemenation of proper orthogonal decomposition. In *47th AIAA Aerospace Sciences Meeting*, Orlando, FL.
- Brenner, T. A., R. L. Fontenot, P. G. A. Cizmas, T. J. O’Brien, and R. W. Breault (2009). Augmented Proper Orthogonal Decomposition for Problems with Moving Discontinuities. *Powder Technology*. submitted for publication.
- Cizmas, P. G. A. (2007, January). An acceleration approach for reduced-order models based on proper orthogonal decomposition. In *45th Aerospace Sciences Meeting and Exhibit*, AIAA Paper 2007-713, Reno, Nevada.
- Cizmas, P. G. A. and J. I. Gargoloff (2008, May-June). Mesh generation and deformation algorithm for aeroelastic simulations. *Journal of Aircraft* 45(3), 1062–1066.
- Cizmas, P. G. A., J. I. Gargoloff, T. W. Strganac, and P. S. Beran (2007, June). A numerical method for nonlinear aeroelastic analysis of wings with large deformation. In *International Forum on Aeroelasticity and Structural Dynamics*, Stockholm.
- Cizmas, P. G. A. and A. Palacios (2003, March-April). Proper orthogonal decomposition of turbine rotor-stator interaction. *AIAA Journal of Propulsion and Power* 19(2), 268–281.
- Cizmas, P. G. A., B. R. Richardson, T. A. Brenner, T. J. O’Brien, and R. W. Breault (2008). Acceleration techniques for reduced-order models based on proper orthogonal decomposition. *Journal of Computational Physics* 227, 7791–7812.

- Crespo da Silva, M. R. M. and C. C. Glynn (1978a). Nonlinear flexural-flexural-torsional dynamics of inextensional beams. i. equations of motion. *The Journal of Structural Mechanics* 6(4), 437–448.
- Crespo da Silva, M. R. M. and C. C. Glynn (1978b). Nonlinear flexural-flexural-torsional dynamics of inextensional beams. ii. forced motions. *The Journal of Structural Mechanics* 6(4), 449–461.
- Doedel, E. J. (1981). Auto: A program for the automatic bifurcation analysis of autonomous systems. In *Proceedings of the 10th Manitoba Conference on Numerical Mathematics and Computations*, University of Manitoba, Winnipeg, Canada, pp. 265–284.
- Doedel, E. J., R. C. Paffenroth, A. R. Champneys, T. F. Fairgrieve, Y. A. Kuznetsov, B. Sandstede, and X. J. Wang (2002). Auto2000: Continuation and bifurcation software for ordinary differential equations. Technical report, California Institute of Technology.
- Eastep, F. E. and J. J. Olsen (1980). Transonic flutter analysis of a rectangular wing with conventional airfoil sections. *AIAA Journal* 18(10), 1159–1164.
- Edwards, J. W., C. V. Spain, D. F. Keller, and R. W. Moses (2009, July-August). Transport wing flutter model transonic limit cycle oscillation test. *Journal of Aircraft* 46(4), 1104–1113.
- Fehlberg, E. (1969). Low-order classical Runge-Kutta formulas with stepsize control and their application to some heat transfer problems. Technical report, NASA, USA.
- Gerald, C. F. and P. O. Wheatley (2004). *Applied Numerical Analysis* (7 ed.). Pearson Education, Inc.
- Golub, G. H. and C. F. van Loan (1989). *Matrix Computation* (Second ed.). Baltimore: The Johns Hopkins University Press.
- Haberman, R. (2004). *Applied Partial Differential Equations with Fourier Series and Boundary Value Problems* (4 ed.). Pearson Education, Inc.
- Holmes, P., J. L. Lumley, and G. Berkooz (1996). *Turbulence, Coherent Structures, Dynamical Systems and Symmetry*. Cambridge University Press.
- Lee, J. S. J., R. Haralick, and L. Shapiro (1987, April). Morphological edge detection. *IEEE J. of Robotics and Automation* RA-3(2), 142–156.
- Li, N., Y. Saad, and E. Chow (2003). Crout versions of ilu for general sparse matrices. *SIAM Journal of Scientific Computing* 25(2), 716–728.
- Lieu, T. and C. Farhat (2005, December). Adaptation of POD-based aeroelastic ROMs for varying Mach number and angle of attack: Application to a complete F-16 configuration. In *U. S. Air Force T&E Days*, AIAA Paper 2005-7666, Nashville, Tennessee.
- Love, A. E. H. (1944). *A Treatise on the Mathematical Theory of Elasticity* (4 ed.). Dover Publications, Inc.
- Lucia, D. J., P. S. Beran, and P. I. King (2003, March-April). Reduced order modeling of an elastic panel in transonic flow. *Journal of Aircraft* 40(2), 338–347.
- Meirovitch, L. (1967). *Analytical Methods in Vibrations*. Macmillan.

- Press, W. H., W. T. Vetterling, S. A. Teukolsky, and B. P. Flannery (1992). *Numerical Recipes in FORTRAN - The Art of Scientific Computing* (Second ed.). Cambridge.
- Ritter, G. and J. Wilson (2000). *Computer Vision Algorithms in Image Algebra* (2nd ed.), Chapter 4, pp. 137–138. CRC Press.
- Roark, R. J., W. C. Young, and R. G. Budynas (2002). *Roark's Formulas for Stress and Strain* (7 ed.). McGraw-Hill, Inc.
- Snyder, R. D., J. N. Scott, N. S. Khot, P. S. Beran, and J. V. Zweber (2003, April). Predictions of store-induced limit-cycle oscillations using Euler and Navier-Stokes fluid dynamics. In *44th AIAA/ASME/ASCE/AHS Structures, Structural Dynamics, and Materials Conference*, AIAA Paper 2003-1727, Norfolk, Virginia.
- Soille, P. (2003). *Morphological Image Analysis: Principles and Applications* (2nd ed.). Springer-Verlag.
- Strganac, T. W., P. G. Cizmas, C. Nickkawde, J. Gargoloff, and P. S. Beran (2005). Aeroelastic analysis for future air vehicle concepts using a fully nonlinear methodology. In *AIAA/ASME/ASCE/AHS/ASC Structures, Structural Dynamics and Materials Conference*, AIAA Paper 2005-2171, Austin, Texas, pp. 4575–4608.
- Tessler, A. and T. J. R. Hughes (1985). A three-node mindlin plate element with improved transverse shear. *Computer Methods in Applied Mechanics and Engineering* 50(1), 7–91. cauta.
- Ugural, A. C. and S. K. Fenster (1981). *Advanced Stength and Applied Elasticity*. Elsevier.
- Yuan, T., P. G. Cizmas, and T. O'Brien (2005). A reduced-order model for a bubbling fluidized bed based on proper orthogonal decomposition. *Computers and Chemical Engineering* 30(2), 243–259.

## Acknowledgment/Disclaimer

This work was sponsored by the Air Force Office of Scientific Research, USAF, under grant/contract number FA9550-07-1-0289. The views and conclusions contained herein are those of the authors and should not be interpreted as necessarily representing the official policies or endorsements, either expressed or implied, of the Air Force of Scientific Research or the U.S. Government.

## Personnel Supported During Duration of Grant

Paul G. A. Cizmas	Professor, Texas A&M University
Thomas W. Strganac	Professor, Texas A&M University
Gregory D. Worley	Graduate Student, Texas A&M University
Amy Lucas	Graduate Student, Texas A&M University
Brian A. Freno	Graduate Student, Texas A&M University

## Publications

Journal articles:

1. Gargoloff, J. I. and Cizmas, P. G. A., "Mesh Generation and Deformation Algorithm for Aeroelasticity Simulations," *Journal of Aircraft* Vol. 45, No. 3, 2008, pp. 1062-1066.
2. Cizmas, P. G. A., Gargoloff, J. I., Strganac, T. W. and Beran, P. S. "A Parallel Multigrid Algorithm for Aeroelasticity Simulations," *Journal of Aircraft* Vol. 47, No. 1, 2010.

Conference papers:

1. Cizmas, P. G. A., Freno, B. A., Brenner, T. A., Worley, G. D., "A High-Fidelity Nonlinear Aeroelastic Model for Aircraft with Large Wing Deformation," *International Forum on Aeroelasticity and Structural Dynamics*, Seattle, WA, June 2009.
2. McFarland, D. M., Cizmas, P., Strganac, T., Bergman, L., Lee, Y., Vakakis, A., Hubbard, S., "Aeroelastic Analysis of a Transonic Wing for Design of Local Nonlinear Attachments," AIAA Paper 2009-2365, *50th AIAA/ASME/ASCE/AHS/ASC Structures, Structural Dynamics, and Materials Conference*, Palm Springs, CA, May 2009.
3. Cizmas, P. G. A., Strganac, T. W., Richardson, B. R., and Brenner, T. A., "Techniques for Reducing the Computational Cost of Proper Orthogonal Decomposition," *The 44th Annual Technical Meeting of the Society of Engineering Science, October 2007*, College Station, Texas, October, 2007.
4. Cizmas, P. G. A., Gargoloff, J. I., Strganac, T. W., and Beran, P. S., "A Numerical Method for Nonlinear Aeroelastic Analysis of Wings with Large Deformation," *International Forum on Aeroelasticity and Structural Dynamics*, Stockholm, Sweden, June, 2007.

## Honors and Awards Received

NONE

## **AFRL Point of Contact**

Dr. Philip Beran and Dr. Richard Snyder

## Appendix A

# Nonlinear Beam - Hamilton's Principle

The extended form of Hamilton's principle is

$$\delta I = \delta \int_{t_1}^{t_2} (\mathcal{T} + \mathcal{W}) dt = 0. \quad (\text{A.1})$$

Noting that

$$\mathcal{L} = \mathcal{T} - \mathcal{V} \quad (\text{A.2})$$

$$\mathcal{W} = \mathcal{W}_c + \mathcal{W}_{nc} \quad (\text{A.3})$$

$$\delta \mathcal{V} = -\delta \mathcal{W}_c, \quad (\text{A.4})$$

Hamilton's principle can be rewritten as [Meirovitch \(1967\)](#)

$$\delta I = \delta \int_{t_1}^{t_2} (\mathcal{L} + \mathcal{W}_{nc}) dt = 0, \quad (\text{A.5})$$

where

$$\delta \mathcal{W}_{nc} = \delta \mathcal{W}_B + \int_0^L (Q_u \delta u + Q_v \delta v + Q_w \delta w + Q_\phi \delta \phi) ds. \quad (\text{A.6})$$

This leads to

$$\delta I = \int_{t_1}^{t_2} \left\{ \delta \mathcal{L} + \delta \mathcal{W}_B + \int_0^L (Q_u \delta u + Q_v \delta v + Q_w \delta w + Q_\phi \delta \phi) ds \right\} dt = 0, \quad (\text{A.7})$$

which, upon accounting for the inextensionality constraint, becomes

$$\begin{aligned} \delta I = \int_{t_1}^{t_2} \left\{ \int_0^L \left( \delta l + \delta \left[ \frac{1}{2} \lambda \left( 1 - (1 + u')^2 + v'^2 + w'^2 \right) \right] \right) ds \right. \\ \left. + \delta \mathcal{W}_B + \int_0^L (Q_u \delta u + Q_v \delta v + Q_w \delta w + Q_\phi \delta \phi) ds \right\} dt = 0. \end{aligned} \quad (\text{A.8})$$

The variations of the cross-sectional Lagrangian,  $\theta$ , and  $\psi$  are

$$\begin{aligned}\delta l = & \frac{\partial l}{\partial \dot{u}} \delta \dot{u} + \frac{\partial l}{\partial \dot{v}} \delta \dot{v} + \frac{\partial l}{\partial \dot{w}} \delta \dot{w} + \frac{\partial l}{\partial \psi} \delta \psi + \frac{\partial l}{\partial \dot{\psi}} \delta \dot{\psi} + \frac{\partial l}{\partial \psi'} \delta \psi' \\ & + \frac{\partial l}{\partial \theta} \delta \theta + \frac{\partial l}{\partial \dot{\theta}} \delta \dot{\theta} + \frac{\partial l}{\partial \theta'} \delta \theta' + \frac{\partial l}{\partial \phi} \delta \phi + \frac{\partial l}{\partial \dot{\phi}} \delta \dot{\phi} + \frac{\partial l}{\partial \phi'} \delta \phi'\end{aligned}\quad (\text{A.9})$$

$$\delta \theta = \frac{\partial \theta}{\partial u'} \delta u' + \frac{\partial \theta}{\partial v'} \delta v' + \frac{\partial \theta}{\partial w'} \delta w' \quad (\text{A.10})$$

$$\delta \psi = \frac{\partial \psi}{\partial u'} \delta u' + \frac{\partial \psi}{\partial v'} \delta v'. \quad (\text{A.11})$$

The variation of the cross-sectional Lagrangian is then written as

$$\begin{aligned}\delta l = & \frac{\partial l}{\partial \dot{u}} \delta \dot{u} + \frac{\partial l}{\partial \dot{v}} \delta \dot{v} + \frac{\partial l}{\partial \dot{w}} \delta \dot{w} + \frac{\partial l}{\partial \psi} \left( \frac{\partial \psi}{\partial u'} \delta u' + \frac{\partial \psi}{\partial v'} \delta v' \right) \\ & + \frac{\partial l}{\partial \dot{\psi}} \left( \frac{\partial^2 \psi}{\partial t \partial u'} \delta u' + \frac{\partial \psi}{\partial u'} \delta \dot{u}' + \frac{\partial^2 \psi}{\partial t \partial v'} \delta v' + \frac{\partial \psi}{\partial v'} \delta \dot{v}' \right) \\ & + \frac{\partial l}{\partial \psi'} \left( \frac{\partial^2 \psi}{\partial s \partial u'} \delta u' + \frac{\partial \psi}{\partial u'} \delta u'' + \frac{\partial^2 \psi}{\partial s \partial v'} \delta v' + \frac{\partial \psi}{\partial v'} \delta v'' \right) \\ & + \frac{\partial l}{\partial \theta} \left( \frac{\partial \theta}{\partial u'} \delta u' + \frac{\partial \theta}{\partial v'} \delta v' + \frac{\partial \theta}{\partial w'} \delta w' \right) \delta \theta \\ & + \frac{\partial l}{\partial \dot{\theta}} \left( \frac{\partial^2 \theta}{\partial t \partial u'} \delta u' + \frac{\partial \theta}{\partial u'} \delta \dot{u}' + \frac{\partial^2 \theta}{\partial t \partial v'} \delta v' + \frac{\partial \theta}{\partial v'} \delta \dot{v}' + \frac{\partial^2 \theta}{\partial t \partial w'} \delta w' + \frac{\partial \theta}{\partial w'} \delta \dot{w}' \right) \\ & + \frac{\partial l}{\partial \theta'} \left( \frac{\partial^2 \theta}{\partial s \partial u'} \delta u' + \frac{\partial \theta}{\partial u'} \delta u'' + \frac{\partial^2 \theta}{\partial s \partial v'} \delta v' + \frac{\partial \theta}{\partial v'} \delta v'' + \frac{\partial^2 \theta}{\partial s \partial w'} \delta w' + \frac{\partial \theta}{\partial w'} \delta w'' \right) \\ & + \frac{\partial l}{\partial \phi} \delta \phi + \frac{\partial l}{\partial \dot{\phi}} \delta \dot{\phi} + \frac{\partial l}{\partial \phi'} \delta \phi'\end{aligned}\quad (\text{A.12})$$

Expanding (A.8) and performing integration by parts to express the integrand in terms of the variations  $\delta u$ ,  $\delta v$ ,  $\delta w$ , and  $\delta \phi$  yields

$$\begin{aligned}
\delta I = & \int_{t_1}^{t_2} \int_0^L \left\{ \left[ -\frac{\partial^2 l}{\partial s \partial \psi} \frac{\partial \psi}{\partial u'} - \frac{\partial l}{\partial \psi} \frac{\partial^2 \psi}{\partial s \partial u'} + \frac{\partial^3 l}{\partial t \partial s \partial \dot{\psi}} \frac{\partial \psi}{\partial u'} + \frac{\partial^2 l}{\partial t \partial \dot{\psi}} \frac{\partial^2 \psi}{\partial s \partial u'} \right] \delta u \right. \\
& + \left[ \frac{\partial^3 l}{\partial s^2 \partial \psi'} \frac{\partial \psi}{\partial u'} + \frac{\partial^2 l}{\partial s \partial \psi'} \frac{\partial^2 \psi}{\partial s \partial u'} - \frac{\partial^2 l}{\partial s \partial \theta} \frac{\partial \theta}{\partial u'} - \frac{\partial l}{\partial \theta} \frac{\partial^2 \theta}{\partial s \partial u'} \right] \delta u \\
& + \left[ \frac{\partial^3 l}{\partial t \partial s \partial \dot{\theta}} \frac{\partial \theta}{\partial u'} + \frac{\partial^2 l}{\partial t \partial \dot{\theta}} \frac{\partial^2 \theta}{\partial s \partial u'} + \frac{\partial^3 l}{\partial s^2 \partial \theta'} \frac{\partial \theta}{\partial u'} + \frac{\partial^2 l}{\partial s \partial \theta'} \frac{\partial^2 \theta}{\partial s \partial u'} \right] \delta u \\
& + \left[ -\frac{\partial^2 l}{\partial s \partial \psi} \frac{\partial \psi}{\partial v'} - \frac{\partial l}{\partial \psi} \frac{\partial^2 \psi}{\partial s \partial v'} + \frac{\partial^3 l}{\partial t \partial s \partial \dot{\psi}} \frac{\partial \psi}{\partial v'} + \frac{\partial^2 l}{\partial t \partial \dot{\psi}} \frac{\partial^2 \psi}{\partial s \partial v'} \right] \delta v \\
& + \left[ \frac{\partial^3 l}{\partial s^2 \partial \psi'} \frac{\partial \psi}{\partial v'} + \frac{\partial^2 l}{\partial s \partial \psi'} \frac{\partial^2 \psi}{\partial s \partial v'} - \frac{\partial^2 l}{\partial s \partial \theta} \frac{\partial \theta}{\partial v'} - \frac{\partial l}{\partial \theta} \frac{\partial^2 \theta}{\partial s \partial v'} \right] \delta v \\
& + \left[ \frac{\partial^3 l}{\partial t \partial s \partial \dot{\theta}} \frac{\partial \theta}{\partial v'} + \frac{\partial^2 l}{\partial t \partial \dot{\theta}} \frac{\partial^2 \theta}{\partial s \partial v'} + \frac{\partial^3 l}{\partial s^2 \partial \theta'} \frac{\partial \theta}{\partial v'} + \frac{\partial^2 l}{\partial s \partial \theta'} \frac{\partial^2 \theta}{\partial s \partial v'} \right] \delta v \\
& + \left[ -\frac{\partial^2 l}{\partial s \partial \theta} \frac{\partial \theta}{\partial w'} - \frac{\partial l}{\partial \theta} \frac{\partial^2 \theta}{\partial s \partial w'} + \frac{\partial^3 l}{\partial t \partial s \partial \dot{\theta}} \frac{\partial \theta}{\partial w'} \right] \delta w \\
& + \left[ \frac{\partial^2 l}{\partial t \partial \dot{\theta}} \frac{\partial^2 \theta}{\partial s \partial w'} + \frac{\partial^3 l}{\partial s^2 \partial \theta'} \frac{\partial \theta}{\partial w'} + \frac{\partial^2 l}{\partial s \partial \theta'} \frac{\partial^2 \theta}{\partial s \partial w'} \right] \delta w \\
& + \left[ \frac{\partial l}{\partial \phi} - \frac{\partial^2 l}{\partial t \partial \dot{\phi}} - \frac{\partial^2 l}{\partial s \partial \phi'} \right] \delta \phi - \frac{\partial^2 l}{\partial t \partial \dot{u}} \delta u - \frac{\partial^2 l}{\partial t \partial \dot{v}} \delta v - \frac{\partial^2 l}{\partial t \partial \dot{w}} \delta w \\
& + [\lambda' (1 + u') + \lambda u''] \delta u + [\lambda' v' + \lambda v''] \delta v + [\lambda' w' + \lambda w''] \delta w \\
& + Q_u \delta u + Q_v \delta v + Q_w \delta w + Q_\phi \delta \phi \Big\} ds + \left[ \frac{\partial l}{\partial \phi'} \delta \phi \right. \\
& - \left( \left[ \frac{\partial^2 l}{\partial t \partial \dot{\psi}} + \frac{\partial^2 l}{\partial s \partial \psi'} - \frac{\partial l}{\partial \psi} \right] \frac{\partial \psi}{\partial u'} + \left[ \frac{\partial^2 l}{\partial t \partial \dot{\theta}} + \frac{\partial^2 l}{\partial s \partial \theta'} - \frac{\partial l}{\partial \theta} \right] \frac{\partial \theta}{\partial u'} + \lambda [1 + u'] \right) \delta u \\
& - \left( \left[ \frac{\partial^2 l}{\partial t \partial \dot{\psi}} + \frac{\partial^2 l}{\partial s \partial \psi'} - \frac{\partial l}{\partial \psi} \right] \frac{\partial \psi}{\partial v'} + \left[ \frac{\partial^2 l}{\partial t \partial \dot{\theta}} + \frac{\partial^2 l}{\partial s \partial \theta'} - \frac{\partial l}{\partial \theta} \right] \frac{\partial \theta}{\partial v'} + \lambda v' \right) \delta v \\
& - \left( \left[ \frac{\partial^2 l}{\partial t \partial \dot{\theta}} + \frac{\partial^2 l}{\partial s \partial \theta'} - \frac{\partial l}{\partial \theta} \right] \frac{\partial \theta}{\partial w'} + \lambda w' \right) \delta w + \delta \mathcal{W}_B \\
& + \left( \frac{\partial l}{\partial \psi'} \frac{\partial \psi}{\partial v'} + \frac{\partial l}{\partial \theta'} \frac{\partial \theta}{\partial v'} - \left[ \frac{\partial l}{\partial \psi'} \frac{\partial \psi}{\partial u'} + \frac{\partial l}{\partial \theta'} \frac{\partial \theta}{\partial u'} \right] \frac{v'}{1 + u'} \right) \delta v' \\
& + \left( \frac{\partial l}{\partial \psi'} \frac{\partial \psi}{\partial w'} + \frac{\partial l}{\partial \theta'} \frac{\partial \theta}{\partial w'} - \left[ \frac{\partial l}{\partial \psi'} \frac{\partial \psi}{\partial u'} + \frac{\partial l}{\partial \theta'} \frac{\partial \theta}{\partial u'} \right] \frac{w'}{1 + u'} \right) \delta w' \Big]_{s=0}^{s=L} dt = 0. \tag{A.13}
\end{aligned}$$

Letting

$$A_\alpha = \frac{\partial^2 l}{\partial t \partial \dot{\alpha}} + \frac{\partial^2 l}{\partial s \partial \alpha'} - \frac{\partial l}{\partial \alpha} \quad (\alpha = \psi, \theta, \phi) \tag{A.14}$$

$$H_\alpha = \frac{\partial l}{\partial \psi'} \frac{\partial \psi}{\partial \alpha'} + \frac{\partial l}{\partial \theta'} \frac{\partial \theta}{\partial \alpha'} \quad (\alpha = u, v, w), \tag{A.15}$$



(A.13) can be written as

$$\begin{aligned}
\delta I = & \int_{t_1}^{t_2} \int_0^L \left\{ \left[ A_\psi \frac{\partial \psi}{\partial u'} + A_\theta \frac{\partial \theta}{\partial u'} + \lambda (1 + u') \right]' \delta u + \left[ A_\psi \frac{\partial \psi}{\partial v'} + A_\theta \frac{\partial \theta}{\partial v'} + \lambda v' \right]' \delta v \right. \\
& + \left[ A_\theta \frac{\partial \theta}{\partial w'} + \lambda w' \right]' \delta w - A_\phi \delta \phi - \frac{\partial^2 l}{\partial t \partial \dot{u}} \delta u - \frac{\partial^2 l}{\partial t \partial \dot{v}} \delta v - \frac{\partial^2 l}{\partial t \partial \dot{w}} \delta w \\
& + Q_u \delta u + Q_v \delta v + Q_w \delta w + Q_\phi \delta \phi \Big\} ds \\
& + \left[ \frac{\partial l}{\partial \phi'} \delta \phi - \left( A_\psi \frac{\partial \psi}{\partial u'} + A_\theta \frac{\partial \theta}{\partial u'} + \lambda [1 + u'] \right) \delta u - \left( A_\psi \frac{\partial \psi}{\partial v'} + A_\theta \frac{\partial \theta}{\partial v'} + \lambda v' \right) \delta v \right. \\
& - \left( A_\theta \frac{\partial \theta}{\partial w'} + \lambda w' \right) \delta w + \delta \mathcal{W}_B + \left( H_v - H_u \frac{v'}{1 + u'} \right) \delta v' \\
& \left. + \left( H_w - H_u \frac{w'}{1 + u'} \right) \delta w' \right]_{s=0}^{s=L} dt = 0,
\end{aligned} \tag{A.16}$$

requiring that

$$\left[ A_\psi \frac{\partial \psi}{\partial u'} + A_\theta \frac{\partial \theta}{\partial u'} + \lambda (1 + u') \right]' = \frac{\partial^2 l}{\partial t \partial \dot{u}} - Q_u \tag{A.17}$$

$$\left[ A_\psi \frac{\partial \psi}{\partial v'} + A_\theta \frac{\partial \theta}{\partial v'} + \lambda v' \right]' = \frac{\partial^2 l}{\partial t \partial \dot{v}} - Q_v \tag{A.18}$$

$$\left[ A_\theta \frac{\partial \theta}{\partial w'} + \lambda w' \right]' = \frac{\partial^2 l}{\partial t \partial \dot{w}} - Q_w \tag{A.19}$$

$$A_\phi = Q_\phi. \tag{A.20}$$

(A.17)-(A.20) are the equations of motion.